Excited states in the highly deformed proton emitter ^{131}Eu

Thesis submitted in accordance with the requirements of the University of Liverpool
for the degree of Doctor in Philosophy by

Holly Louise Tann

November 2022

Let us not take ourselves too seriously.

None of us has a monopoly on wisdom.

QUEEN ELIZABETH II

Acknowledgements

Firstly, I would like to thank my supervisors for their support. Juha, for his unfathomable level of knowledge and expertise, and clear passion for the work he does which is reflected in those who work around him. Dave, for the opportunity to do the PhD in the first place and being the friendly, approachable character that made that happen. Your positive attitude, in that even the tiniest peak could be monumentally important is highly motivating. Also to Robert and Paul for their support as secondary supervisors.

Thank you to the JYU Nuclear Spectroscopy Group and the Liverpool Nuclear Physics Group for some of the most unforgettable experiences of my life. I won't deny that doing this PhD was tough, but I have had the opportunities to experience Finland, the most beautiful country full of the most wonderful people, work on world-leading experiments and present to experts at the top of the field around the world. I have met some life-long friends through this PhD.

I would also like to thank my friends and family for their untiring patience throughout the past few years as I was impossible to make plans with. Also for always listening to me and being so supportive, and having confidence in me even when my ideas appear rather ambitious.

Lastly, and most importantly, I would like to thank Adam for always being my number one fan, making me believe I can do anything and supporting me in everything I do.

Abstract

The newly commissioned JUROGAM 3 γ-ray spectrometer was used in conjunction with the MARA recoil separator to establish excited states in the proton emitting nucleus ^{131}Eu, which is predicted to possess one of the highest quadrupole deformations in the $130 \leq A \leq 140$ region. By identifying the rotational band structures in this nucleus, deformation parameters can be established that provide crucial constraints on theoretical models of deformed proton emitters. Fine structure has previously been observed in the proton emission from ^{131}Eu. The sensitivity of the fine structure to the wavefunctions of states in the parent and daughter nuclides generated significant theoretical interest in this nuclide allowing a $3/2^+$ spin parity assignment to be made for the ground state. The composition of the wavefunctions are highly sensitive to dynamic effects, therefore it would be particularly informative to study the excited states built upon the $3/2^+$ state and other low-lying Nilsson bandheads. Proton radioactivity from ^{131}Eu has been remeasured with a proton energy of 952(5) keV for the ground-state decay to the ground state in the ^{130}Sm daughter and a proton energy of 828(6) keV for the fine structure transition from the ground state in ^{131}Eu to the 2^+ excited state in the ^{130}Sm daughter. The 2^+ to 0^+ transition in ^{130}Sm was also measured directly for the first time with an energy of 125(1) keV. The ^{131}Eu nucleus was produced with a cross section of 140(30) nb with a 23(5) % fine structure branching ratio. The half-life was measured to be 17.6(5) ms. In-beam data from this study was highly fruitful and through gamma-ray correlations it was possible to build rotational band(s). The obtained band(s) in this study cannot firmly be assigned, however comparison to the ^{141}Ho structure suggests that the band is based on 7/2[523] Nilsson state. No clear evidence for existence of any sort of isomeric decay feeding the ground state could be identified.

Preface

The author of this thesis conducted two experiments employing the recently commissioned in-flight recoil separator MARA. In the first experiment, M09, the author acted as Spokesperson. The aim was to search for new beta-delayed proton emitters ^{133}Gd and ^{132}Eu. In this experiment many beta-delayed proton emitters were identified, however the sensitivity to identify new emitters was not reached. Many new isomeric transitions measured at the focal-plane setup were identified. In the second experiment, JM06, the author acted as Liaison. The aim was to study in-beam gamma rays using the recoil-decay tagging method on very neutron-deficient ground-state proton emitter ^{131}Eu. This experiment was the first in-beam study utilizing the recoil separator MARA. The author of this thesis had a notable role in preparing and performing these experiments. In addition, author of this thesis had a major role in analyzing the data. The author spent two years in Jyväskylä JYFL-ACCLAB. During this time, JUROGAM 3 was built and installed at the target position of the MARA recoil separator. The author had a significant role during this process.

Contents

References   **104**

List of Figures

List of Tables

Chapter 1

Introduction

This thesis documents the results of an experiment carried out using MARA [1, 2], the mass analysing recoil apparatus, in combination with JUROGAM 3 [3], the gamma-ray spectrometer array, to study the excited states in the highly deformed proton emitter ^{131}Eu at the University of Jyväskylä Accelerator Laboratory (JYFL-ACCLAB). The best known cases of deformed proton emitters are located in the 130<A<140 mass region. Understanding emission of a proton in such deformed cases requires knowledge of the proton emission data as well as the structure of the excited states. The ^{131}Eu nucleus is expected to have one of the largest quadrupole deformations in this region [4] and is the only highly-deformed proton-emitting nucleus to have had fine structure observed in the proton decay. Experiments studying proton radioactivity can lead to a de-composition of the nuclear wavefunction, give information on nuclear deformation and act as a tool to study the tunnelling process through the Coulomb and centrifugal barrier, as described by Blank [5].

In this chapter the nuclear models used in current research have been highlighted and deformation of the nucleus discussed. The motivations behind experimental nuclear physics are also considered and what we can achieve by studying certain phenomena.

1.1 Nuclear Models

The atomic nucleus is a quantum object that consists of A nucleons: N neutrons and Z protons, which are held together primarily by strong nuclear forces. The nucleus is only stable for certain numbers of protons and neutrons, depending on the ratio between them. Stable nuclei have a lifetime comparable to that of the universe. Those systems which do not form stable configurations are known as unstable nuclei, which will undergo radioactive decays until they reach stability. These nuclei, in their ground-state configuration, are unstable, allowing emission of constituent nucleon(s). Within the nuclear volume, there is competition between attractive nuclear forces, repulsive electromagnetic forces, and proton-neutron asymmetry which determines the binding energy/mass of the nucleus.

Mathematical models are used to understand the structure of the nucleus, providing a framework with which to compare experimental results. The nucleus can be treated as a many-body quantum system. A many-body problem for heavy nuclei does not have an exact solution. Approximations are used in addition to small perturbations to give the most realistic model. If it is assumed that the wavefunction can be written as the product of individual particle wavefunctions and variables may be separated, every particle can then be said to be moving in an average potential generated by the interactions of all other particles. There are several approximations, for which the potential is assumed to take different shapes. When it is assumed that the wavefunction variables cannot be separated, the nucleus can once again be treated as a one-body problem- an individual quantum particle. The wavefunction is then used to describe the shape and potential energy of the particle, which changes with nuclear deformations. Therefore, the nucleus can be viewed by two basic nuclear models: Collectively, where there are no individual particle states, such as in the Liquid Drop Model, or individually where nucleons have discrete energy levels, such as the Shell Model. These models and the perturbations necessary to model the nucleus as accurately as possible are discussed in more detail in the next chapter.

For every nucleus there are maximum and minimum numbers of nucleons that are

able to be supported whilst remaining bound and avoiding nucleon emission. The nucleon limits are known as the proton and neutron drip lines, defined as the boundaries beyond which it becomes energetically favourable to emit a nucleon and the nucleon separation energy becomes negative. When there are too many protons, a proton will be emitted and too many neutrons, a neutron will be emitted. The difference is however, that an unbound proton may be technically unbound but in order for the proton to be emitted, it must tunnel through the potential barrier which holds protons within the nucleus causing half lives of typically milliseconds to seconds. The neutron drip line has no such barrier and therefore nuclei close to this line decay with half lives of the order 10^{-22} seconds and are experimentally very difficult or even impossible to study.

Nucleons can reside in higher energy states. Nuclei in their excited states are unstable and therefore likely to de-excite through various modes in order to reach a stable ground state. By studying excited states, we are able to determine collective features of the nucleus such as vibration or rotation.

1.2 Nuclear Deformation

The equilibrium shape of a nucleus at the magic numbers is a sphere but when the nucleon numbers differ from the number at closed shells, the ground state can be axially deformed, for example prolate (like a rugby ball) or oblate (like a discus), as can be seen in figure 1.1. Nuclear matter is known to be incompressible so when the volume remains constant, excitations are possible when the nuclear shape oscillates. Excitation is also possible when a nucleus rotates.

Nucleon emission will occur when a decrease in binding energy, resulting from the decrease in the energy from the symmetry term, is large enough to overcome the reduced volume binding energy. In the case of proton emission it is primarily determined by the increase in electrostatic potential energy. The proton drip line therefore is located closer to stability than the neutron drip line.

Nucleons experience long range quadrupole-quadrupole interactions meaning that deformed nuclei lying between closed shells possess additional binding energy relative
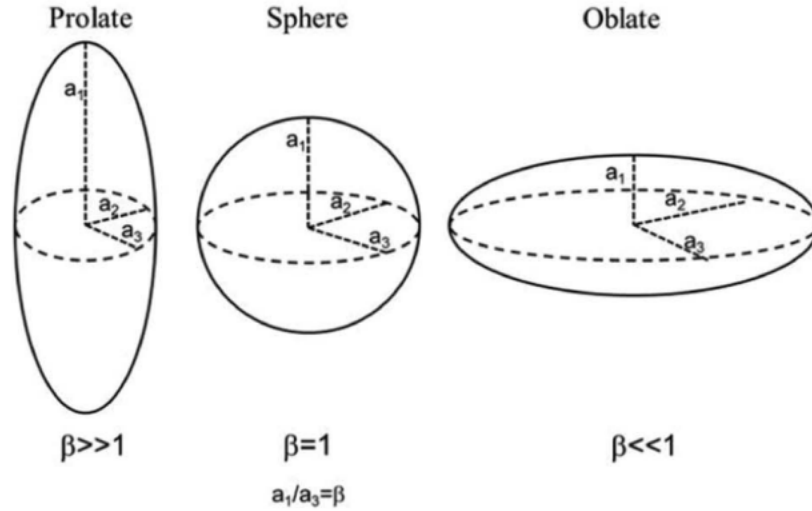
Figure 1.1: Diagram showing three possible nuclear shapes: prolate, sphere and oblate spheroid [6]. The aspect ratio, β, defines the deformity of the nucleus where $\beta = a_1/a_2 = a_1/a_3$.

to those with complete shells. Therefore, low levels of deformation are present in the region of magic numbers, and large deformation around mid-shell points.

Nuclear deformation has been well reproduced by the Nilsson model which is discussed in more detail in the next chapter.

1.3 Experimental Nuclear Physics

A principal goal in nuclear physics is to determine the number of protons and neutrons that can be bound within a nucleus. In light nuclei with fewer than 50 protons, the Coulomb barrier is small, allowing proton emission to occur very quickly. The proton emission process in heavier nuclei is slowed significantly by a larger Coulomb barrier meaning current experimental techniques allow the study of some heavier proton-emitting nuclei.

The study of the structure of the nucleus allows identification of fundamental properties such as decay modes and half lives. As more exotic nuclei are reached, one can study deformations, lifetimes and energies of excited states as well as decay modes including alpha, β^+ or β^- emitters, fission, one-proton or two-proton and exotic-cluster

emitters. By measuring the energy emitted following a transition, information is gained regarding the difference in the two states. Looking at the patterns that emerge in the chart of the nuclides as a result of these measurements allows us to predict the behaviour of groups of nuclei.

At high spin, in order to carry the angular momentum most efficiently, nuclear structure becomes an interaction between the collective and non-collective elements, i.e. the rotational core versus the individual particle alignment.

Chapter 2

Theoretical Concepts

The nucleus incorporates several types of behaviour which interact with one another. Excitations in the nucleus can be considered as single particle or collective modes, the interaction between these modes is what makes nuclear spectroscopy so compelling to researchers. Radioactive nuclei often decay by more than one decay mode, however the primary decay mode is governed by the ratio of protons to neutrons. While a nucleus with a small proton excess may decay via β^+/EC emission, a large excess of protons will lead to the spontaneous emission of a proton [7].

2.1 The Shell Model

As can be seen in the Liquid Drop Model, multiple corrections must be added to the macroscopic picture of the nucleus to be able to make it reasonable in comparison to data so it is important that microscopic single-particle effects are taken into consideration. Experimental evidence confirms that collective models have their limitations and implies that there is a shell structure present. Perhaps most notably, nuclei with certain 'magic' or 'doubly-magic' numbers are spherical and have separation energies for both protons and neutrons much higher than those of their neighbours. There is also a significant peak in the energies of the first excited 2^+ states in nuclei at the proton or neutron 'magic' numbers relative to neighbouring nuclei; this would suggest they possess an increased stability to resist excitations.

As protons and neutrons are fermions, like electrons in the atomic shell model, energy states in the nucleus are filled from the lowest to highest when nucleons are added. There are separate energy levels for both protons and neutrons where the nucleons are arranged in orbitals each with a defined angular momentum.

In the nuclear shell model it is assumed that each nucleon moves within the mean field of N-1 nucleons where there are N nucleons in the nucleus. The intricate two-body interactions are ignored and each particle acts independently of the others so each nucleon only feels a central force. The mean field is an average interaction with all other particles in the nucleus and simplifies the nuclear many-body problem to a solvable two-body problem. If two nucleons i and j experience a short range interaction potential $v(r_{i,j})$, then the average potential acting on each particle can be shown as

$$V_i(r_i) = \langle \Sigma_j v(r_{i,j}) \rangle. \tag{2.1}$$

Essentially there are two methods in determining the potential: the first based upon empirical evidence which includes square well, harmonic oscillator and Woods-Saxon potentials, and the second in which the mean field is self consistent, based upon the nucleon-nucleon interaction.
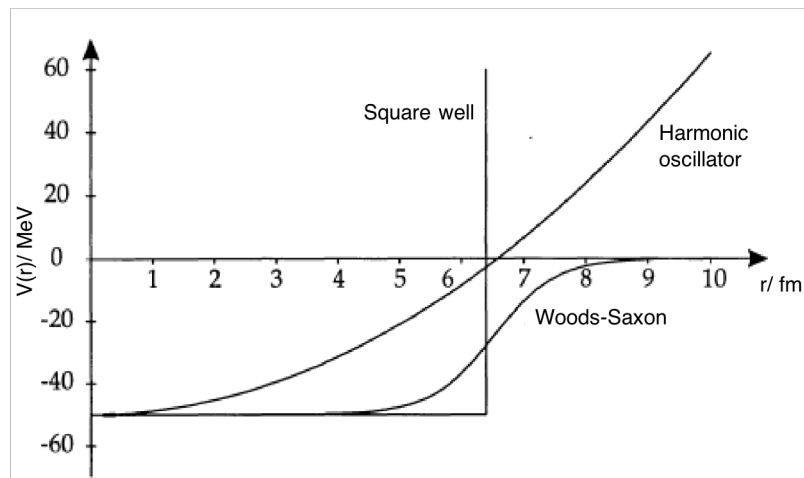
Figure 2.1: Nucleons move in a mean potential which may be determined by assuming an empirical form of potential such as the square well, harmonic oscillator or Woods-Saxon. They are presented here for comparison.

2.1.1 The Harmonic Oscillator Potential

The Harmonic Oscillator Potential benefits from being easily handled analytically. The potential is described in the following form

$$V_{HO} = -V + \frac{1}{2}mw^2r^2, \tag{2.2}$$

where m is the mass of the particle, r is the radius, w is the frequency of the harmonic motion of the particle and V is the depth of the potential. The energy eigenvalues can be found from the solution to the Schrödinger equation, labelled by the oscillator quantum number N

$$E_N = (N + \frac{3}{2})\hbar w. \tag{2.3}$$

The parity of each shell is given by $(-1)^N$. The number of degenerate levels for a given N is $(N+1)(N+2)$.

2.1.2 The Woods-Saxon Potential

The Woods-Saxon nuclear potential is thought to be the most realistic model

$$V(r) = \frac{-V_0}{\{1 + exp[(r - R_0)/a]\}}, \tag{2.4}$$

where a is the surface diffuseness term, also known as skin thickness, R_0 is the radius term and V_0 the depth of the potential. The Woods-Saxon is a finite potential, $V(r) \longrightarrow 0$ as $r > R_0$.

The Woods-Saxon and harmonic oscillator potentials can be seen side by side in figure 2.1. As V(r) $\longrightarrow \infty$ when r is large in the harmonic oscillator potential it is not a realistic potential. The Woods-Saxon potential represents the centre of the nucleus well where nuclear forces are experienced uniformly and therefore there is no overall force. The l^2 term in the Modified Harmonic Oscillator potential adjusts the bottom of the potential to create this flat section.
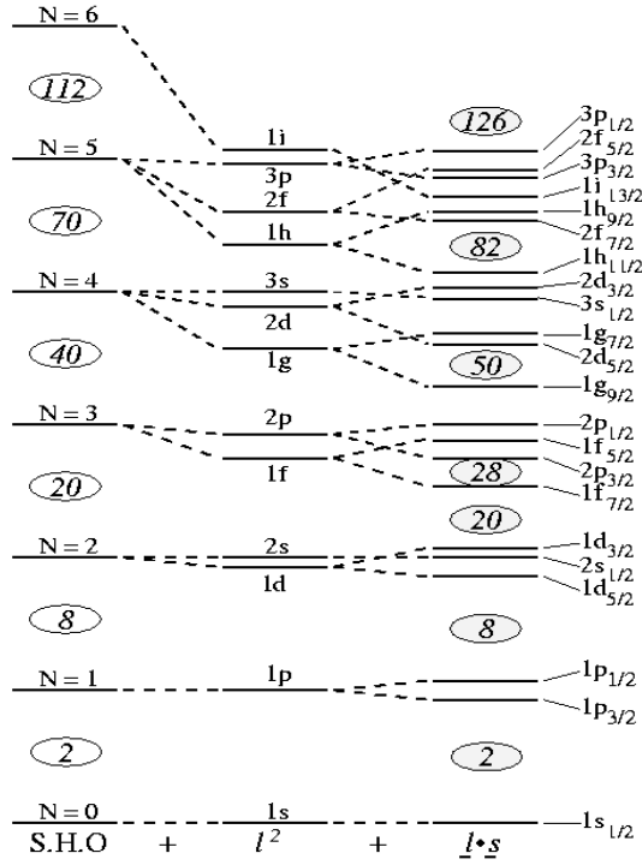
Figure 2.2: Single particle orbitals as seen in the shell model. The left shows the simple harmonic oscillator model, the centre shows the effect of adding the surface correction term. The right hand side shows nl_j where the spin-orbit contribution is included.

2.1.3   Spin-Orbit Coupling

The spin-orbit interaction arises at the atomic level as a result of the magnetic moment of the electron with the magnetic field produced as it moves about the nucleus. In the nucleus a similar adjustment can be included in order to fit the magic numbers that are observed. The extra term describes the force experienced by a nucleon depending on the direction of its spin. The term accounts for the strong spin-orbit coupling where particles with $j = |l| + |s|$ are more bound and therefore reside in lower energy states. j is the total angular momentum, l is the orbital angular momentum and s is the spin angular momentum. The potential becomes

$$V(r) \longrightarrow V(r) + \mu \underline{l}.\underline{s}, \tag{2.5}$$
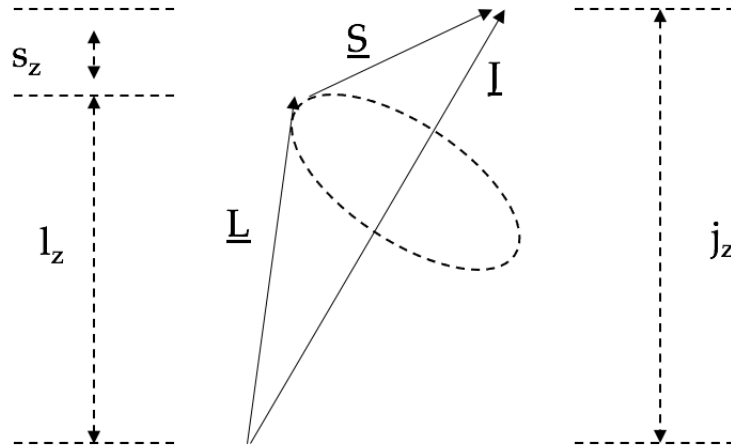
Figure 2.3: Vectors L and S precess about J.

The shell model can be described quite simply by $H = H_0 + H_{res}$, where H_0 typically consists of a kinetic energy term, the Woods-Saxon potential as well as the spin-orbit term. This model correctly recreates the nuclear magic numbers.

2.2 Deformed Nuclei

Nuclei which have an odd mass with either a nucleon added or removed from the closed shell have a single-particle excitation represented by low-lying energy levels. The pairing energy is approximately represented by the energy between the lowest excited state and the ground state. When looking at deformed even-even nuclei it was discovered that those located far from closed shells possess levels with energy differences far smaller than pairing energies would suggest the structure should be. This is due to nuclear rotation.

High-spin states can be generated in a nucleus via collective motions of the nucleons such as vibrations and rotations, and single-particle effects such as pair breaking where the spin of individual nucleons generates the total spin of the nucleus. A non-collective level scheme appears as a complicated, unstructured set of energy levels and has no regular features, unlike a collective level scheme which shows band structures for example.

Deformation in nuclei is evident by large electric quadrupole moments. When the nucleus is deformed the quadrupole-quadrupole interaction increases the binding energy for those nuclei which are located between closed shells. The long-range element of the nucleon-nucleon residual interaction forms the basis for deformation, whereas the component that favours a spherical-shaped nucleus is the short-range pairing.

When nucleons reside in partially filled shells their orbits are anisotropic so the mean field is not spherical. The shape of the nucleus therefore depends on the combination of effects from individual nucleons and the pairing interactions between nucleons.

Deformation of the nucleus can be described in terms of the bulk rotation of nuclei and surface vibrations. The Bohr and Mottelson collective model assumes a well defined surface which can be described in terms of a radius vector defined by an expansion of spherical harmonics

$$R(\theta, \phi, t) = R_0(1 + \Sigma_{\lambda \geq 1}\Sigma_{\mu=-\lambda}^{+\lambda}\alpha_{\lambda\mu}(t)Y_{\lambda\mu}(\theta, \phi)), \tag{2.6}$$

where R_0 describes the radius of a sphere with the same volume as the ellipsoid and the terms $\alpha_{\lambda\mu}$ describe time dependent changes in the nuclear volume where λ is the deformation type. $\lambda = 1$ corresponds to a dipole which is shown by a shift in the centre of mass. $\lambda = 2$ is a quadrupole which corresponds to an ellipsoid shaped deformation.

For quadrupole shapes, two parameters are required to describe the shape: β and γ. The quadrupole deformation parameter, β, measures the degree of deformation of the nucleus where $\beta = 0$ is a sphere and $\beta \neq 0$ is a quadrupole ellipsoid. A prolate shape is defined by $\beta > 0$ and an oblate shape is defined by $\beta < 0$. Parameter γ measures the length along the principal axes. When $\gamma = 0°$ the shape is prolate and the z-axis is the long, symmetry axis as shown in figure 2.4. To define the triaxiality of a deformed quadrupole intrinsic shape, γ is defined in the range $0° \leq \gamma \leq 60°$.
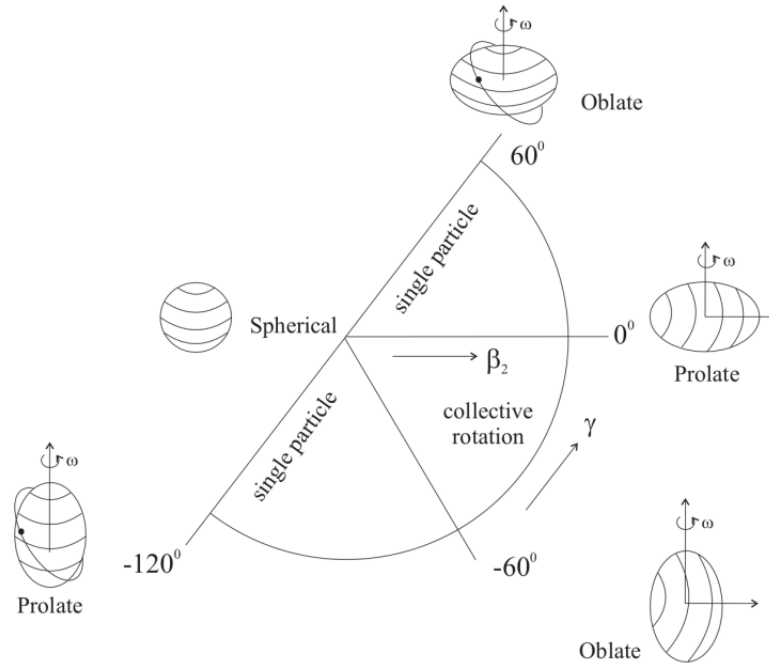
Figure 2.4: The Lund Convention used to specify the triaxiality of a deformed quadrupole intrinsic shape.

2.3   The Deformed Shell Model

When nuclei have partially filled shells they have large quadrupole moments. This leads to the idea that the nucleons move collectively within a deformed potential in the core. Within a spherical nucleus, collective rotation is forbidden as rotation and symmetry axes coincide. Therefore rotational bands are a distinctive feature of deformed nuclei, where the axis of symmetry and rotation are perpendicular. In order to develop the shell model to describe nuclei with deformed shapes the Hamiltonian must include a deformed potential. The deformed potentials that most agree with experimental evidence were evolved from both the harmonic oscillator and the Woods-Saxon potentials.

2.3.1   The Nilsson Model

The Anisotropic Harmonic Oscillator potential describes a spheroidal nucleus which is deformed along the z-axis

$$V(r) = \frac{1}{2}m(\omega_1^2 x^2 + \omega_2^2 y^2 + \omega_3^2 z^2), \tag{2.7}$$

where $\omega_\kappa R_\kappa = \omega_0 R$.

When axial symmetry is assumed and $\gamma=0$, the deformation can be described by ε which as defined as

$$\varepsilon = (\omega_{1,2} - \omega_3)/\omega_0. \tag{2.8}$$

To reproduce nuclear behaviour that is seen experimentally, the potential energy term must include two extra terms to become

$$V(r) = \frac{1}{2}m(\omega_1^2 x^2 + \omega_2^2 y^2 + \omega_3^2 z^2) - C\underline{\ell}\cdot\underline{s} - D\underline{\ell}^2. \tag{2.9}$$

The additional $C\underline{\ell}\cdot\underline{s}$ term originates from the spin-orbit interaction. The $D\underline{\ell}^2$ term flattens the potential well to reproduce the nuclear shape more realistically.

When the additional terms are not considered, the Nilsson energy levels are described by

$$\begin{aligned}
&\hbar\omega_1(n_1 + \frac{1}{2}) + \hbar\omega_2(n_2 + \frac{1}{2}) + \hbar\omega_3(n_3 + \frac{1}{2}) \\
&= \left[(N + \frac{3}{2}) - \varepsilon(n_3 - \frac{N}{3}) + \frac{1}{9}\varepsilon^2(N + \frac{3}{2})\right]\hbar\omega_0.
\end{aligned} \tag{2.10}$$

The energy levels are labelled using asymptotic quantum numbers

$$\Omega^\pi[Nn_3\Lambda]. \tag{2.11}$$

The terms are defined as

Ω : Projection of the total angular momentum j onto the symmetry axis where $\Omega = \Lambda + \Sigma$ and $j = l + s$,

π : Parity of the state where $\pi = (-1)^l$,

N : $Oscillator quantum number where$ N=$n_1 + n_2 + n_3$,

n_3 : The symmetry axis component of oscillator quantum number N,

Λ : Projection of orbital angular momentum l onto the symmetry axis, $\Lambda = l_z$.

In figure 2.5 the spin projections are related to their vector quantities. As long as the nucleus is not rotating and there are no residual interactions, quantum numbers Ω, π, and N are considered 'good' quantum numbers. Numbers n_3 and Λ are not constants of motion due to the additional terms shown in equation 2.9. They are defined as asymptotic quantum numbers because they only become 'good' when $\varepsilon \to \infty$.
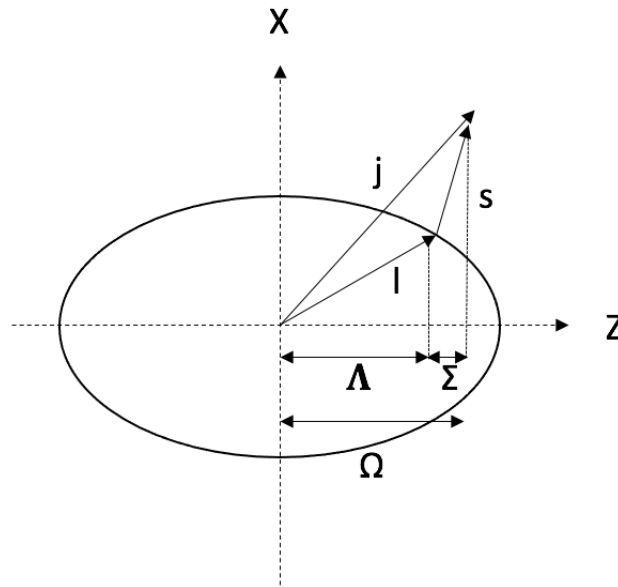
Figure 2.5: The spin projections related to their vector quantities.

As the nucleus becomes deformed some of the degeneracies seen in the spherical harmonic oscillator are lifted. As shown in figure 2.7, the spherical levels, (ℓ), at $\varepsilon = 0$ are each split into $(2j+1)/2$ levels where

$$\Omega = \pm\frac{1}{2}, \pm\frac{3}{2}, ..., \pm j \tag{2.12}$$

The quantum number Ω defines the overlap of an orbital with it's deformed core. In figure 2.6 splitting of the Ω states can be seen where a low-Ω state favours prolate deformation i.e $\varepsilon > 0$. This instance has a large overlap with the core and results in a lower energy. The degeneracy that remains, $\pm\Omega$, determines that each deformed level can accommodate two protons or two neutrons.
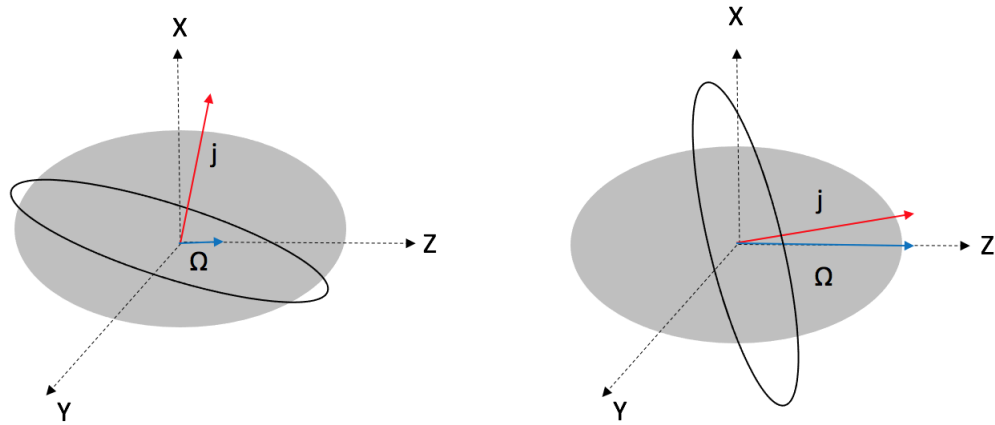
Figure 2.6: The Ω quantum number defines the overlap of the orbital with the deformed core. The potential is attractive so a large overlap leads to a gain in energy (lowering of state energy) and a small overlap results in an increased energy.

The Nilsson diagram, shown in figure 2.7, demonstrates nuclear energy levels as a function of the quadrupole-deformation parameter. When modelling an axially symmetric deformed potential there are certain features that can be noticed in the diagrams. As can be seen around $\beta_2 = 0$ the magic numbers from the spherical shell model are reproduced where there is low level density. As deformation increases, it can be seen that the spherical shell magic numbers are not observed, however new shell closures are apparent relating to deformed shapes.

When an orbital possesses a high-j value it is lowered in energy due to the spin-orbit interaction. This means it is located alongside levels with an opposing parity. These unnatural-parity, low-Ω orbitals, for $\beta_2 > 0$, are said to intrude down into a lower shell at large deformations.

At particular deformation values, due to interactions between states with the same quantum numbers but originating from different j-shells, the slopes of single-particle levels can change. As a result of the Pauli exclusion principle these states cannot cross, instead they meet at crossing points and exchange character.
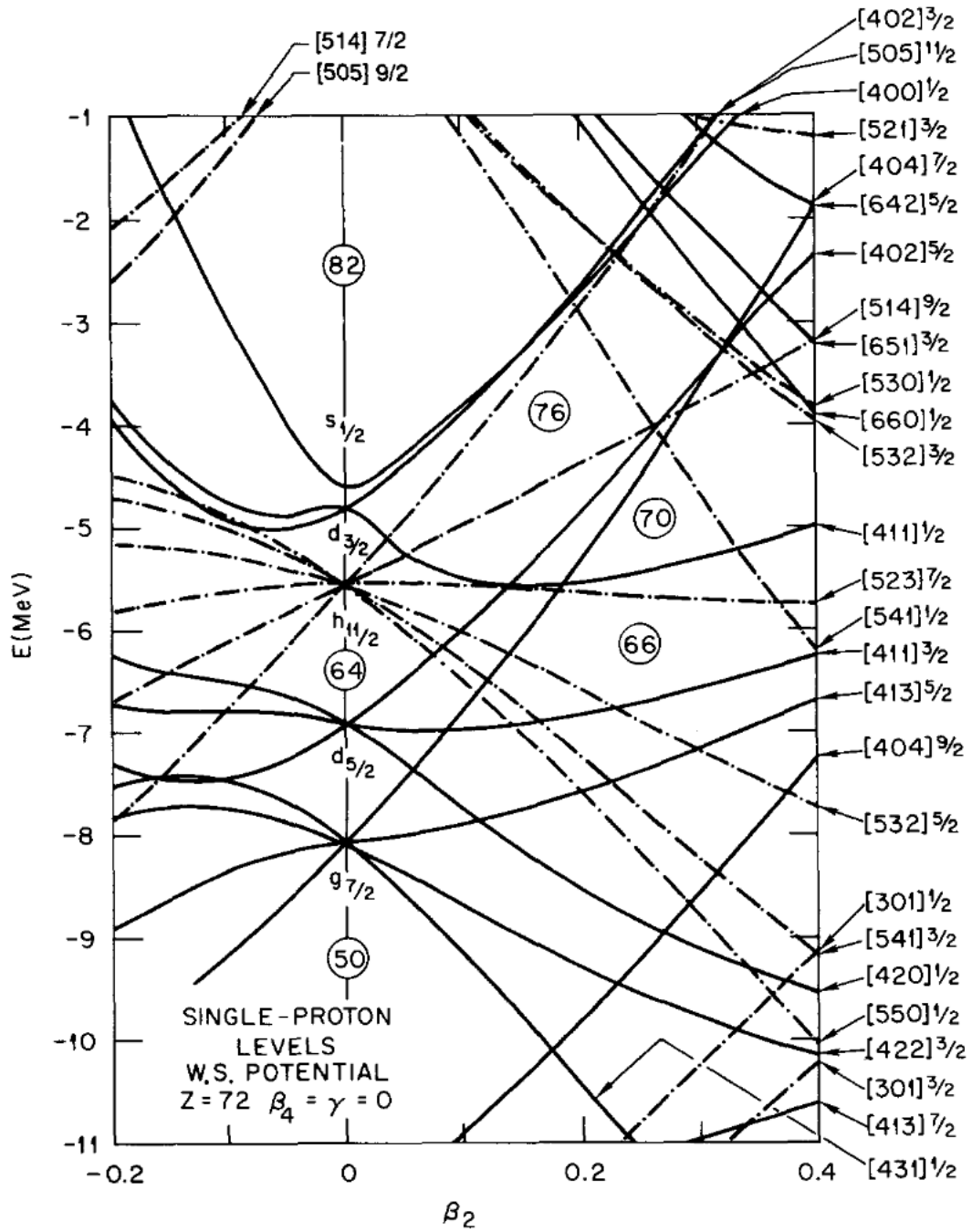
Figure 2.7: Proton single-particle levels versus quadrupole deformation β_2 [8].

2.4   Rotational Model

When a nucleus is deformed, contrary to the case of a spherically symmetric nucleus, the orientation can be defined and therefore also the degrees of freedom of the system. Typically deformed nuclei are found in the 150<A<190 and A>220 regions. In these regions the quadrupole moments of nuclei have been found to be relatively large. In deformed nuclei all nucleons can contribute to a collective rotation around the rotational axis which is perpendicular to the symmetry axis.

The deformation parameter, β, is related to the eccentricity of the nucleus

$$\beta = \frac{4}{3}\sqrt{\frac{\pi}{5}}\frac{\Delta R}{R_{av}}, \tag{2.13}$$

where ΔR is the differences between the axes of the nucleus and R_{av} is the average radius of the nucleus. The nucleus is defined as a prolate ellipsoid when $\beta > 0$ and it has an elongated shape. The nucleus is an oblate ellipsoid when $\beta < 0$ and has a flattened shape.

Classically, energy related to rotation can be given by

$$E_{rot} = \frac{1}{2}\mathcal{J}w^2 = \frac{I^2}{2\mathcal{J}}, \tag{2.14}$$

where $w = I/\mathcal{J}$ is the frequency of rotation, $\mathcal{J}$ is the moment of inertia and I is the total spin.

The excitation energy of the states can then be given by

$$E(I) = \frac{\hbar^2}{2\mathcal{J}}I(I+1) - K^2. \tag{2.15}$$

Using the energy of the collective states obtained experimentally, it is possible to extract the moment of inertia. The projection of the total angular momentum on the rotation axis is

$$I_x = \sqrt{I(I+1) - K^2}. \tag{2.16}$$

The rotational frequency is defined by

$$\hbar\omega = \frac{dE}{dI_x}.$$

<div align="right">(2.17)</div>

Collective rotation stemming from single nucleon state combinations moving in a deformed potential leads to the formation of rotational bands- these are allowed sequences of transitions within an excited nucleus. The allowed sequences can also be described by the selection rules, discussed later in this section. The energy separating each level within a rotational band is ΔE.

2.4.1 Moment of Inertia

The moment of inertia, $\mathcal{J}$, varies with rotational frequency but can be viewed in multiple ways as the nucleus is a complicated system. The nucleus could be considered a rigid body but this provides an estimate much higher than experimental values allude to. Typically the moments of inertia of a nucleus at low spin are less that half of the predicted rigid-body value- this is a consequence of nuclear pairing. Another model would be that of an irrotational fluid, however when this is considered the estimation is much lower than experimental values. The ideal model for a nuclear moment of inertia therefore lies between these two limits. Residual interactions within the nucleus are the explanation for this result and the nuclear moment of inertia is considered a dynamic quantity. In order to explain rotational effects within the nucleus the kinematic and dynamic moments of inertia are defined.

The first derivative of equation 2.15 is known as the kinematic moment of inertia

$$\mathcal{J}^{(1)} = (\hbar^2 I) \left[\frac{dE(I)}{dI} \right]^{-1} = \hbar\frac{I}{w},$$

<div align="right">(2.18)</div>

$$= \frac{\hbar(2I-1)}{E_\gamma},$$

where $\omega(I)/\hbar = E_{\gamma 1}/2$.

The second derivative of equation 2.15, known as the dynamic moment of inertia,

can be described as the response of a system to a torque and is defined as

$$\mathcal{J}^{(2)} = (\hbar^2) \left[\frac{d^2 E(I)}{dI^2} \right]^{-1} = \hbar \frac{dI}{dw},$$

$$(2.19)$$

$$= \frac{4\hbar}{(E_{\gamma 1} - E_{\gamma 2})},$$

where $\omega(I-1)/\hbar = (E_{\gamma 1} - E_{\gamma 2})/4$.

By measuring these quantities it is possible to determine further details about the structure of the nucleus such as the alignment of single particles as well as information about the rotating core. When looking at a plot of ω^2 against $\mathcal{J}$ an effect known as backbending can sometimes be seen as a characteristic 's' shape on the plot. It can be seen when two bands cross: the ground state band and the s-band. The states which have the lowest energy for a given value of I are the yrast states, these are the states which are actually observed. In the rotating core a pair of nucleons break forming the s-band. Their angular momentum can then align with the rotation axis. Band crossings occur when the ground-state energy is approximately equal to the s-band energy.

It is possible to determine how strongly the bands have interacted with each other by how pronounced the backbend is. The more that the wavefunctions of the states in the ground-state band overlap with the wavefunctions in the s-band the smoother the band crossing will be and therefore the weaker the backbend.

The ground-state spin of an odd mass nucleus is determined by the spin of the final nucleon. In even-even nuclei, the ground-state spins are always $0\hbar$.

2.5   The Particle-Rotor Model

The particle-rotor model describes the nucleus as a deformed core coupling to independent valence nucleons. As long as the collective rotation is slow in comparison to the motion of the single particle element, the Hamiltonian may be separated into the intrinsic and rotational components

$$H = H_{int} + H_{rot}. \tag{2.20}$$

The eigenvalues are

$$\Psi = \Psi_{int}\Psi_{rot}. \tag{2.21}$$

The angular momentum consists of the collective component from the rotating core and the single-particle component which is created by the motion of valence nucleons. These combine to give total spin

$$I = R + J. \tag{2.22}$$
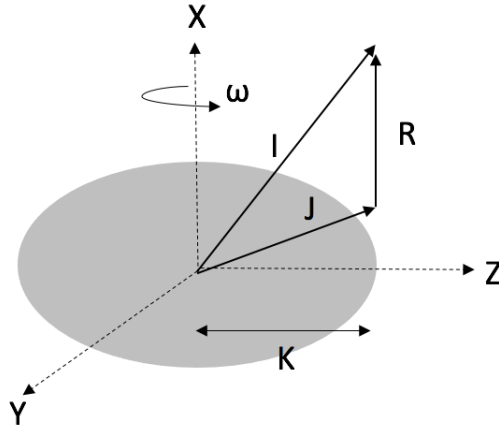
Figure 2.8: Coupling of angular momentum in the particle-rotor model. K shows the projection of total spin I onto the the symmetry axis Z. X shows the rotation axis.

This is shown in figure 2.8 where R describes the collective rotation and J is the sum of the intrinsic angular momenta of the single valence nucleons

$$J = \sum_i j_i. \tag{2.23}$$
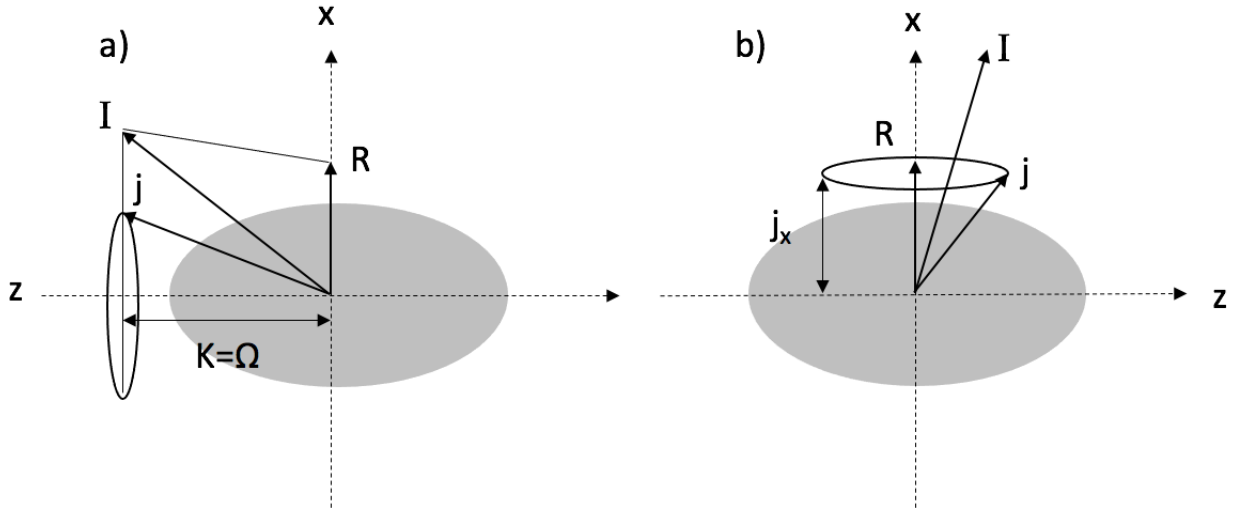
Figure 2.9: a) The Strong-coupling limit or deformation-aligned coupling scheme (DAL). b) The weak-coupling limit or rotation-aligned coupling scheme (RAL)

2.5.1 Strong Coupling (DAL)

The strong coupling limit is achieved when, in the deformed shell model, level splitting of the single particle energies for differing values of Ω is comparatively large with the perturbation due to the Coriolis contribution. The deformation-aligned coupling scheme is recognised when deformation is large or the Coriolis matrix elements are small. j is the angular momentum vector and precesses about the deformation axis. The energy spectrum is therefore given by the levels defined as

$$E_{rot} = \left(\frac{\hbar^2}{2\mathcal{J}_0}\right)[I(I+1) - K^2].\tag{2.24}$$

2.5.2 Decoupling Limit (RAL)

When a nucleus is weakly deformed or the rotation sufficiently fast, the coupling of the valence nucleon to the deformed core may be negligible as the Coriolis force may be too strong. The strong Coriolis force can lead to alignment of j, the nucleonic angular momentum with R, the rotational angular momentum. Also known as the rotation-aligned coupling scheme at this limit the rotational band has allowed spins of $I = j, j+2, j+4, ...$ The level energies in this instance are given by

$$E_{rot} = \left(\frac{\hbar^2}{2\mathcal{J}_0} \right) (I - j_x)(I - j_x + 1). \tag{2.25}$$

Within odd mass nuclei, in a $K = \frac{1}{2}$ band, where a is defined as the decoupling parameter, the rotational energy is given by

$$E(I) = \left(\frac{\hbar^2}{2\mathcal{J}_0} \right) [I(I+1) + a(-1)^{I+\frac{1}{2}}(I + \frac{1}{2})]. \tag{2.26}$$

2.6 Proton emission

Proton emission is a form of nuclear decay in which a proton is emitted from the nucleus. This occurs in so-called proton-rich nuclei where protons are emitted with an experimentally observed Q-value between 0.8-2 MeV. For proton radioactivity to be possible, the proton separation energy must be negative. Proton emission is a rather rare form of decay predicted by Goldansky in 1960 [9] which is fundamental in providing structural information far from stability and is often the only way to access information on the most proton-rich nuclei. It was initially discovered in 1970 where emitted protons were observed from a ^{53}Co isomeric state [10]. Proton radioactivity from the ground state was first observed in 1982 from ^{151}Lu [11] and then ^{147}Tm [12]. Currently over 40 proton emitters have been experimentally established including those which emit from isomeric states as described in the review by Pfützner et al. [13].

The Coulomb barrier is the energy barrier that results from the electrostatic interaction between two nuclei as described by Goldansky in 1960 [9]; this barrier must be overcome so two nuclei can come within a close enough range to take part in a reaction. As protons are charged particles, it is their sensitivity to other charged protons which creates a Coulomb barrier preventing a proton from leaving the nucleus quickly, even when it is unbound. The particle must tunnel through the Coulomb barrier- this process depends on the energy available as well as the height of the barrier, which directly depends on the number of protons in the nucleus. The barrier penetration can lead to measurable half lives that are sensitive to the decay energy available along with the

barrier height. As can be seen in figure 2.10, in most cases, the more energy that is available the shorter the tunnelling time and for nuclei with higher Z, more energy is required for the particle to tunnel in the same amount of time.
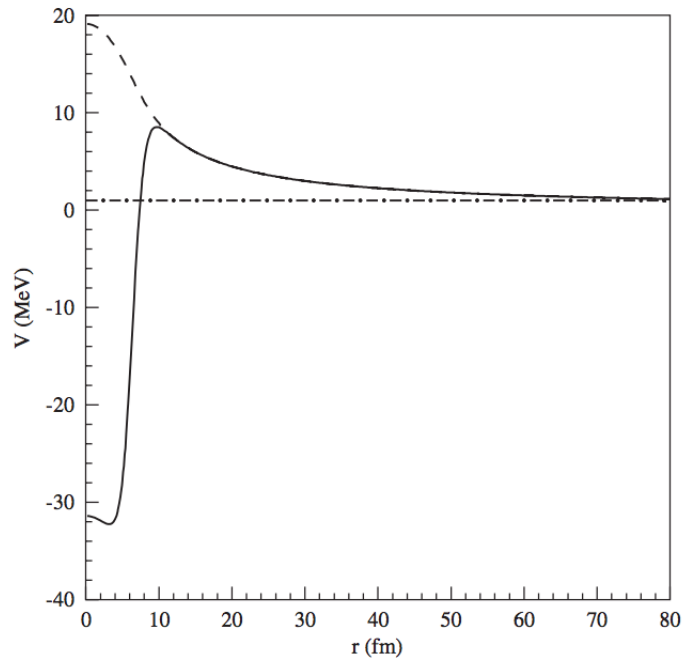
Figure 2.10: The spherical component of the nuclear plus Coulomb interaction is shown by the solid line as a function of the radius in ^{131}Eu. The Coulomb component is shown by the dashed line and the Q-value of the proton shown by the dot–dashed line, as presented in [14].

Half lives of proton radioactivity are also sensitive to orbital angular momentum of specific states meaning a small correction in the form of the centrifugal barrier is also present in the potential, proportional to orbital angular momentum. When a centrifugal potential is added the height of the barrier increases. If two particles have the same amount of energy, one that has a higher orbital angular momentum with respect to the nucleus will have more difficulty leaving the nucleus. A proton and a neutron both experience the same mean potential when they move within the nucleus except for the addition of the Coulomb potential experienced by the protons. After being added to the Coulomb potential, the centrifugal barrier results in a wider, higher barrier which increases the half life [15]. The angular momentum and parity selection rule for proton

emission is given by

$$|J_i - J_f| \pm \frac{1}{2} \leq l \leq (J_i + J_f) \pm \frac{1}{2}, \tag{2.27}$$

where J_i and J_f are the spins of the initial and final states in the transition respectively and l is the angular momentum of the proton. The parity selection rule for proton emission is

$$\pi_f = \pi_i(-1)^l, \tag{2.28}$$

where π is the parity of the state.

When the proton excess increases, nuclear forces are unable to bind all of the protons together and the proton drip line is reached. It is at this point that spontaneous emission of a proton can take place from the ground state of the nucleus. Proton emission occurs in odd-Z nuclei beyond the limit of proton-rich nuclei when the proton decay energy, or the difference in binding energies between the parent and daughter nucleus is positive. The process of direct proton emission is rare due to the large Coulomb barrier which means that other forms of decay, such as α and β^+/EC are often favoured.

Measuring the half life of proton emission is a good indicator of the angular momentum of the initial state due to the sensitivity to the centrifugal barrier. This can be used with the decay energies to map out nuclear behaviour beyond the proton drip line. Emitted protons can also be used in recoil-decay tagging as a tag to study nuclear models.

Nuclear binding energies are used to define the limits of the nuclear system, characterized by drip lines which are used to define the change from a bound system to an unbound one [13]. When at given Z moving along a line of isotopes away from stability, the proton separation energy reduces and eventually becomes negative. The proton drip line provides a limit at which the proton separation energy changes sign and it is beyond that limit that it becomes energetically favourable to emit a proton. The proton separation energy of a nuclide that has N neutrons and Z protons is given by

the following equation [13]

$$S_p(N, Z) = B(N, Z) - B(N, Z - 1). \qquad (2.29)$$

In general it can be said that for isotopes with odd Z, the proton drip line is closer to stability, this is due to the pairing energy of the proton, meaning even Z isotopes are generally more tightly bound. Furthermore, when there are an even number of nucleons, the two nucleon separation energy may be smaller than the energy for just one nucleon which leads to a situation in which a nuclide is two-proton unbound [13].

In the A≈140 region EC/β^+ decay is another competitive decay mode in which a beta particle is emitted from the nucleus producing an isobar of the original nuclide. The EC/β^+ decay typically occurs in proton-rich nuclei such as those studied in this thesis.

Beta-delayed proton emission is a common decay mode in the majority of nuclei located near the proton drip line that have Z<74. Most beta-delayed proton emitters are odd-odd or even-odd nuclei as the systematics of the emission depend on the energy involved in pair breaking, pair formation and the proton binding energies. When beta-delayed proton emission occurs, the levels in the daughter are populated through β-decay with an excitation energy higher than the proton binding energy and the levels can therefore de-excite via proton emission. In the mass region studied in this thesis, the β-decay feeds into a high level density at excitation energies leading to a bell-shaped continuous proton spectrum. The energy must be sufficient to overcome the Coulomb barrier before proton emission can compete against γ-ray emission. Following the decay process the granddaughter nucleus could also be in an excited state and may emit γ rays as well as conversion electrons.

2.6.1   Fine Structure

Proton decay primarily proceeds to the ground state of the daughter nucleus due to a higher decay Q value, however within rotational nuclei the energy of the first excited state can be very low and therefore a significant branching ratio, known as fine structure,

may proceed to the first excited state.

The first observation of proton emission from a deformed nucleus to the first excited state within the daughter nucleus was seen in ^{131}Eu [16]. Two proton lines were observed with similar half-lives with an energy difference of 121(3) keV. The excited state in the ^{130}Sm daughter then emits a γ ray or decays by internal conversion.

2.7   Gamma-Ray Spectroscopy

2.7.1   Gamma-Ray Emission

Gamma rays were initially discovered by Paul Villard [17] in 1900 whilst studying the radiation emitted from radium. The scientific community largely overlooked his discovery at the time as the discovery of a third, unknown, more penetrating type of radiation that did not fit into the working model of atomic radiation. In 1903 Rutherford proposed naming the third type 'gamma rays' leading on from the characteristic penetrating powers Rutherford had already differentiated in alpha and beta decay in 1899 [18].

A gamma ray is a type of electromagnetic radiation emitted by the nucleus following radioactive decay. Gamma rays are emitted from excited states within the nucleus with a negligible recoil momentum. The energy of an emitted gamma ray therefore directly corresponds to the energy difference between the two states involved in the gamma-ray transition.

As the most likely method of de-excitation between excited states is gamma radiation, gamma-ray spectroscopy is a simple and precise way to gather information on nuclear structure. This has led to the development of high-resolution germanium detectors which are used within large arrays of detectors in order to increase sensitivity.

By looking at the measured half lives of levels within a nucleus the absolute transition probabilities and therefore branching ratios can be determined. Relative spins and parities of the initial and final states can be concluded by looking at the internal conversion coefficients. By studying the gamma rays which are coincident with each

other in a defined time window the transitions can be arranged into their band structure
with the help of relative intensities.

2.7.2   Selection Rules

Charged protons moving in the nucleus generate an electric current. Within the nu-
cleus, charge and current distributions are described by electric and magnetic multipole
moments. When the behaviour of multipole moments is considered within an external
field, multipole moments can be related to the transition rates between states.

The emission of a photon is described by Fermi's Golden Rule, an equation that cal-
culates the probability of a gamma-ray transition per unit time between initial nuclear
state ψ_i and final state ψ_f

$$\lambda_{i \to f} = \frac{2\pi}{\hbar} | < \psi_f |\hat{H}_{nr}^i| \psi_i > |^2 \frac{dN_E}{dE}, \qquad (2.30)$$

where $\lambda_{i \to f}$ describes the transition probability, $\hat{H}_{nr}^i$ is the transition matrix element
and $\frac{dN_E}{dE}$ is the density of the final states.

During gamma-ray emission angular momentum is conserved. The initial and final
nuclear states have a particular angular momentum and parity. This conservation al-
ludes to the structure of the nucleus and controls the process by effecting the properties
of the emitted photon, such as the transition rate. When a photon is emitted there
must be a change in intrinsic angular momentum between initial and final states. The
gamma-ray emission angular-momentum selection rule is

$$|I_i - I_f| \leq L \leq (I_i + I_f), \qquad (2.31)$$

where L is not equal to 0. I_i and I_f are the angular momentum of the initial and final
states in the transition respectively. L is defined as the multipolarity of the transition.
The emitted photon has an intrinsic spin of 1. The parity selection rule is given by

$$\pi = \pi_i \pi_f = (-1)^L, \qquad (2.32)$$

L	Electric Transitions	$\Delta\pi$	Magnetic Transitions	$\Delta\pi$
1	$T(E1)_{sp}= 1.0 \times 10^{14} \; A^{2/3} E_\gamma^3$	Yes	$T(M1)_{sp}= 5.6 \times 10^{13} \; E_\gamma^3$	No
2	$T(E2)_{sp}= 7.3 \times 10^{7} \; A^{4/3} E_\gamma^5$	No	$T(M2)_{sp}= 3.5 \times 10^{7} \; A^{2/3} E_\gamma^3$	Yes
3	$T(E3)_{sp}= 3.4 \times 10^{1} \; A^{2} E_\gamma^7$	Yes	$T(M3)_{sp}= 1.6 \times 10^{1} \; A^{4/3} E_\gamma^7$	No
4	$T(E4)_{sp}= 1.1 \times 10^{-5} \; A^{8/3} E_\gamma^9$	No	$T(M4)_{sp}= 4.5 \times 10^{-6} \; A^{2} E_\gamma^9$	Yes

Table 2.1: Weisskopf single particle transition rates. $T(\sigma\lambda)$ values are given in seconds^{-1} and E is given in MeV.

for electric transitions and

$$\pi = \pi_i \pi_f = (-1)^{L+1}, \tag{2.33}$$

for magnetic transitions where π_i and π_f are the parities of the initial and final states respectively. For a given transition, it is possible to identify the most likely type of photon or multipolarity based on the parity change and allowed angular momentum changes.

Weisskopf [19] made some assumptions about the nucleus in order to calculate estimates of the probability of a transition between two nuclear states. The Weisskopf Estimates are simplified, however they are valuable when comparing to measured transition probabilities. Weisskopf assumed a single-nucleon model to calculate the wavefunctions of the initial and final states, based on the single-particle spherical shell model. The gamma-ray transitions are considered to be due to a single nucleon changing orbital without having an effect on the other nucleons in the nucleus. It is assumed that only one nucleon is involved in the transition where the transition goes from initial state $I_i = L + 1/2$ to final state $I_f = 1/2$. It is also assumed that the wavefunction within the nucleus is constant.

Experimentally it is possible to observe the transition rate and compare to the Weisskopf estimates which in general are within a range of up to a factor of ten. It is also possible to determine if more than one particle contributes to the transition by comparing the single particle estimate to the observed transition. It is not easy to measure the probability of decay directly, however the mean lifetime of an excited state

is easier to measure. The mean lifetime, τ, is related to the transition probability, λ, by

$$\lambda = \frac{1}{\tau}. \tag{2.34}$$

2.7.3   Internal Conversion

Another possible form of decay following a nuclear reaction from a nucleus in an excited state is internal conversion, a process which competes with gamma-ray emission. The excited nucleus interacts with the orbital electrons in an atom causing a single electron to be emitted from the atom. The wavefunction of the electron penetrates the nucleus, coupling to an excited state and receiving the energy of the nuclear transition. The majority of electrons in the internal conversion process originate in the K shell or 1s state as the two electrons in this state are most likely to be within the nuclear volume. The L, M and N shells have s states corresponding to 2s, 3s and 4s respectively and are also able to eject electrons during the internal conversion process. The energy threshold for internal conversion is the binding energy of the electron required to eject it. The energy of the transition during internal conversion is the kinetic energy of the electron that has been emitted minus the binding energy required to remove the electron from the atomic shell in which it resides. This results in discrete energy spectra from internal conversion. A hole is created in the electron shell which is then filled by an electron from a higher energy level causing a cascade of X rays or Auger electrons.

Internal conversion is the primary decay mode for E0 transitions due to conservation of angular momentum. It also dominates when the available energy is small for gamma transitions. The ratio between the two processes is given by way of a ratio known as the internal conversion coefficient

$$\alpha = \frac{e}{\gamma}, \tag{2.35}$$

where e is the number of transitions via conversion electrons and γ is the number of transitions via gamma-ray emission.

Where internal conversion competes with gamma decay, the gamma decay counts can be reduced due to the converted electrons. The count rates for gamma detection must therefore be corrected accordingly

$$N_\gamma = N_0 \frac{\epsilon_\gamma}{1 + \alpha},$$
(2.36)

where N_γ is the number of gamma-ray events measured, N_0 is the number of gamma and converted gamma transitions and ϵ_γ is the gamma detection efficiency. When the energy of conversion electrons is relatively high the detection efficiency is close to 100%.

Chapter 3

Experimental Methods

This chapter describes the reactions used to synthesise nuclei such as fusion-evaporation reactions and formation of a compound nucleus. The equipment used during the experiments described in this thesis are presented including the in-beam detection system consisting of gamma-ray detector array JUROGAM 3, the recoil separator MARA and the versatile focal-plane detection system. The techniques used in this work are also described such as recoil-decay tagging and recoil-isomer tagging.

3.1   Fusion-Evaporation Reactions

There are a finite number of nuclei that are stable on Earth. In order to study those that are not stable they must be created, as they do not occur naturally. A fusion-evaporation reaction occurs when a target nucleus is bombarded by a high-energy projectile with sufficient energy to overcome the Coulomb barrier. The projectile and target fuse together and the product nucleus recoils. The compound nucleus has an excess of energy which is lost via evaporation of high-energy particles.

In fusion-evaporation reactions it is possible to produce various nuclei depending on the combination of incident energy, projectile and the target, however the production of nuclei at the proton drip line is often only accessible through fusion-evaporation reactions using particular combinations of beams and targets which are neutron deficient. The resulting compound nucleus may then emit protons, neutrons and alpha particles.

To optimise the fusion-evaporation process and carefully select the best conditions there are various codes available to estimate the cross sections of the process. In the experiments described in this thesis statistical codes PACE [20] and HIVAP [21] can be used to calculate optimal bombarding energies. One obstacle to overcome with this method of production is that there are many open channels so a detection system with high capabilities for selection is needed, especially for weaker evaporation channels. Energies can be selected to optimise for the desired nuclei however when an evaporation channel is very weak, there is a limit to which one can reduce the presence of contaminant nuclei.

Evaporated particles can be detected at the target position by detectors such as JY-Tube (Jyväskylä-York Tube) which can be used to deduce the presence of evaporation residues. The γ-ray background can therefore be significantly reduced by gating on the evaporated particles. As the products are only indirectly identified, it is not possible to select the exact reaction channel that has proceeded but by reducing the background, coincidence relations can be made between recoils at the focal plane and prompt γ rays at the target position from nuclei produced with very low cross sections.

3.1.1   Beam Delivery and Targets

The University of Jyväskylä accelerator laboratory is host to the K130 cyclotron [22, 23] installed in 1990. The K130 is an isochronus cyclotron meaning it possesses a magnetic field that increases with radius. Three external ECR (electron cyclotron resonance) ion sources are available to use as well as a light-ion source, meaning the K130 is able to deliver a large variety of ion beams for various experiments.

The targets are housed within a target chamber typically mounted on a rotating target wheel or a target fan. A carbon 'reset foil' is also located just after the main target position, used to make certain that all recoiling nuclei have the charge state distribution as required. The carbon foil ensures all ions capture or lose electrons repeatedly so that the Gaussian distribution of the charge states restores. This process is necessary as it can happen that when short-lived isomers are produced and then directly decay after

leaving the target, they will change the charge state of the nuclide. A carbon 'degrader foil' may also be positioned at the entrance to the target chamber which slightly reduces the beam energy where necessary, for example when the difference is so small that the cyclotron is not sensitive to the change, or a re-tuning of the beam is not practical.

3.2 Target Detection Systems

3.2.1 JYTube

At the target position surrounding the target, the particle detector array JYTube (Jyväskylä-York Tube) can be used as a charged particle veto. JYTube consists of 96 separate scintillator detectors with silicon photomultiplier readouts. It is a valuable addition to the spectroscopy at the focal plane of MARA as it provides added sensitivity for distinguishing between neutron and proton evaporation channels. The scintillator detectors are arranged within two barrels which are connected to an end-plate array that has a hole in the middle to allow the recoil products and ion beam through. The target is located between the two barrels. JYTube collects evaporated alphas and protons with an efficiency of 65% for one proton channel suppression and 80% for two proton channel suppression [24], aiding the search for weak evaporation channels.

JYTube was used in the data taking for the M09 experiment, however due to outgassing from the detector causing vacuum issues, it was not utilised during the JM06 experiment, discussed in more detail in the next chapter. The additional veto would have been a welcome addition to the setup and vastly aided in analysis, especially when looking at nuclei with the same mass, however this did not affect the final result.

3.2.2 The JUROGAM 3 Spectrometer

Germanium detectors are semiconductor detectors that are sensitive to ionizing radiation such as X rays and gamma rays. Photons such as gamma rays interact with the the germanium crystal, which is the sensitive volume of the detector, and electron-hole pairs are created. The number of electron-hole pairs created is directly proportional

to the energy of the incident radiation. Incidentally the electrons are transferred to the conduction band from the valence band and the same number of holes result in the valence band. High-energy photons up to MeV may be totally absorbed within germanium as it can have a sensitive, depleted area with a thickness of centimeters. When an electric field is applied across the crystal, the electron-hole pairs will travel to the terminals where an electric pulse is created, the size of which is proportional to the incident radiation. Due to the low energy of the band gap in germanium, HPGe (high purity germanium) detectors must be cooled using liquid nitrogen when operating to minimise noise and maintain good resolution. Reverse-bias voltages of approximately 3500 V are applied across the crystals in HPGe detectors to create a large depletion layer. The charge carriers are swept by the increased electric field to the terminals and the flow of current determines the electric signal. The main advantage of HPGe detectors is their resolution which is typically ≈ 2 keV for a γ-ray at 1.33 MeV.

A clover detector consists of four high-purity germanium crystals mounted so that the structure resembles a four leaf clover. Four smaller crystals as opposed to one large-volume crystal can be more cost effective. Clover detectors also have the advantage that the individual detectors have a smaller solid angle so the effects of Doppler broadening are reduced. The Compton scattering process can also be studied between crystals in order to gain information on incident radiation.

JUROGAM 3 [3] is a germanium-detector array which provides in-beam spectroscopic data. 24 composite Clover detectors and 15 tapered single crystal Phase1-type detectors are arranged in a compact geometry around the target position used to measure prompt γ-rays. JUROGAM 3 can be used in combination with both the MARA and RITU (Recoil Ion Transport Unit) separators. Since 2003 JYU has hosted the JUROGAM I and then JUROGAM II arrays. For the majority of the time the detectors were used at RITU in recoil-decay tagging studies [25] with the focal-plane system GREAT [26]. During this time a total of 1391 days of beam time took place across 187 measurements. The first array, JUROGAM I, consisted of 43 Phase1-type detectors and in 2008 was upgraded to JUROGAM II.
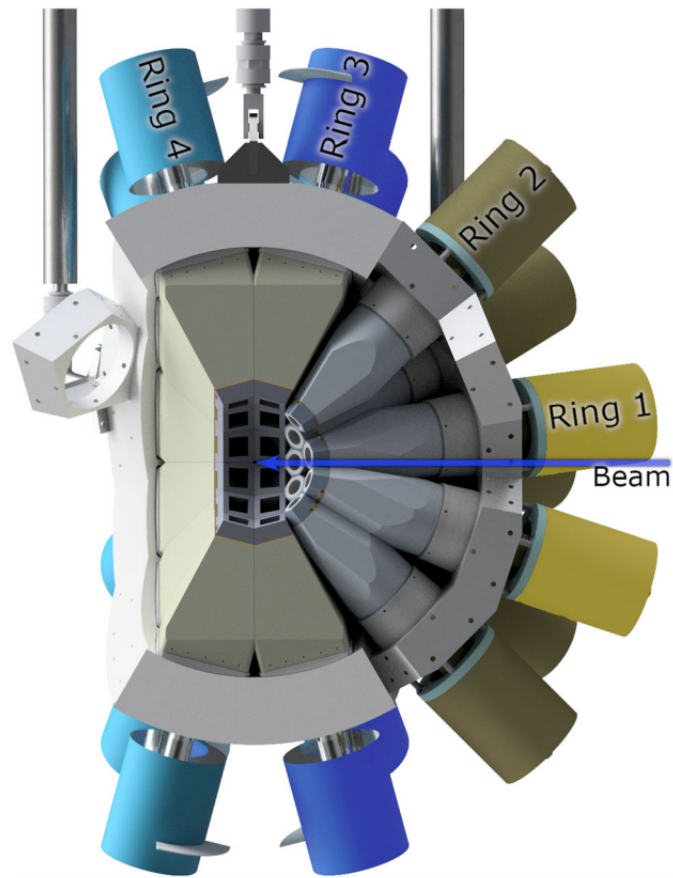
Figure 3.1: A design drawing of the JUROGAM 3 detector array [3]. The beam direction is indicated by an arrow from the right pointing to the target position. One hemisphere in the supporting frame can be seen. Each detector ring has been labelled.

With the addition of MARA this opened up a new and exciting physics program raising sensitivity in probing exotic nuclei around N=Z with in-beam spectroscopy. From the detector configuration point of view, JUROGAM 3 is identical to JUROGAM II. The primary difference between the two incarnations of the spectrometer is that JUROGAM 3 can be moved between RITU and MARA. It enables experiments employing both recoil separators as the two are located in adjacent caves. They can therefore share the majority of the electronics and the data acquisition system. As can be seen in figure 3.1, within the JUROGAM 3 array every germanium detector has a bismuth germanate Compton-suppression shield (BGO) as well as a heavy-metal collimator. Each germanium detector and its associated BGO shield and collimator may be called a detector module. The BGO shields serve as a veto for γ rays that only deposit partial energy within the germanium crystal. The heavy-metal collimators stop γ rays directly hitting the BGO shield when they are emitted from the target. The detector modules are oriented so that the target position sits at the focus of the array. The array is arranged into four detector rings at angles relative to the beam axis: five Phase1 detector modules sit within a ring at $157.6°$, ten Phase1 detectors at $133.6°$, then the Clover detectors are mounted over two rings at angles $104.5°$ and $75.5°$.

3.2.3 Transport Mechanism

To facilitate the movement of JUROGAM 3 between the RITU and MARA caves a transport mechanism was constructed removing the need for unbiasing and warming up the detectors, extending their lifetime by reducing the number of detector anneals. One move of JUROGAM 3 between the caves takes significantly less than the autofill cycle period meaning the detectors can be disconnected from the liquid nitrogen filling system whilst bias is maintained. This is highly beneficial as most experiments at RITU and MARA utilise fusion-evaporation reactions, meaning the germanium detectors are exposed to neutrons which can cause radiation damage by way of dislocation of atoms within the germanium crystal lattice. This negatively affects the performance of the detector by causing incomplete charge collection and a characteristic tail within the

γ-ray spectrum on the low energy side of the photopeak, not always visible until bias is removed. This radiation damage is apparent if the detectors are unbiased and warmed up. Annealing the detectors may diminish the damage however it is important where possible to maintain bias in the detectors throughout an experimental campaign as the process of annealing the full array would be logistically difficult.

The construction of the JUROGAM 3 transport mechanism involved large modifications to the infrastructure. A new support structure was created to house the entire JUROGAM 3 platform. The wall between the two caves had to be rebuilt including a new sliding door mechanism to allow for movement of the array, as well as the ability to work in one cave whilst an experiment is running in the other. All of the auxiliary infrastructure had to be redesigned to move with the entire platform with many of the electronics being moved on top of the support structure. To allow both caves to share the same electronics the existing air-conditioned electronics racks were moved to the roof. The LN_2 lines were extended and the manifolds were mounted onto mobile stands.

The detector modules are mounted within two hemispheres which can be moved independently allowing access to the target position. The whole array is supported by vertical beams which are connected to the movable gantry. The gantry is positioned upon rails and contains the motors necessary to move the array, the high voltage (HV) and preamplifier power supplies, the automatic liquid nitrogen control system, cabling for signal processing, temperature readout and bias shutdown, and electric power distributions. The liquid nitrogen manifolds are contained with the purge containers on mobile trolleys to be moved with the array between the caves.

3.2.4   Calibration

Calibration measurements were taken using ^{133}Ba, ^{152}Eu and ^{60}Co sources by positioning them on the target fan within the target chamber. Each detector may be used in something called direct detection mode in which case each individual crystal is operated as a single detector, or in add-back mode where events are recorded in adjacent or diagonally positioned crystals within a 200 ns coincidence window are identified as

Compton-scattered γ rays. To mitigate this effect, the energies of the coincident γ rays are added together. Using ^{133}Ba and ^{152}Eu sources the photopeak detection efficiency was extracted as a function of the γ-ray energy as can be seen in figure 3.2. Although it wasn't used in the data for this thesis, efficiency curves are shown both with and without JYTube, along with the detection efficiencies for ^{130}Pr and ^{132}Nd which were extracted from $\gamma - \gamma$ coincidences from the JM06 data, explained in detail in reference [3].
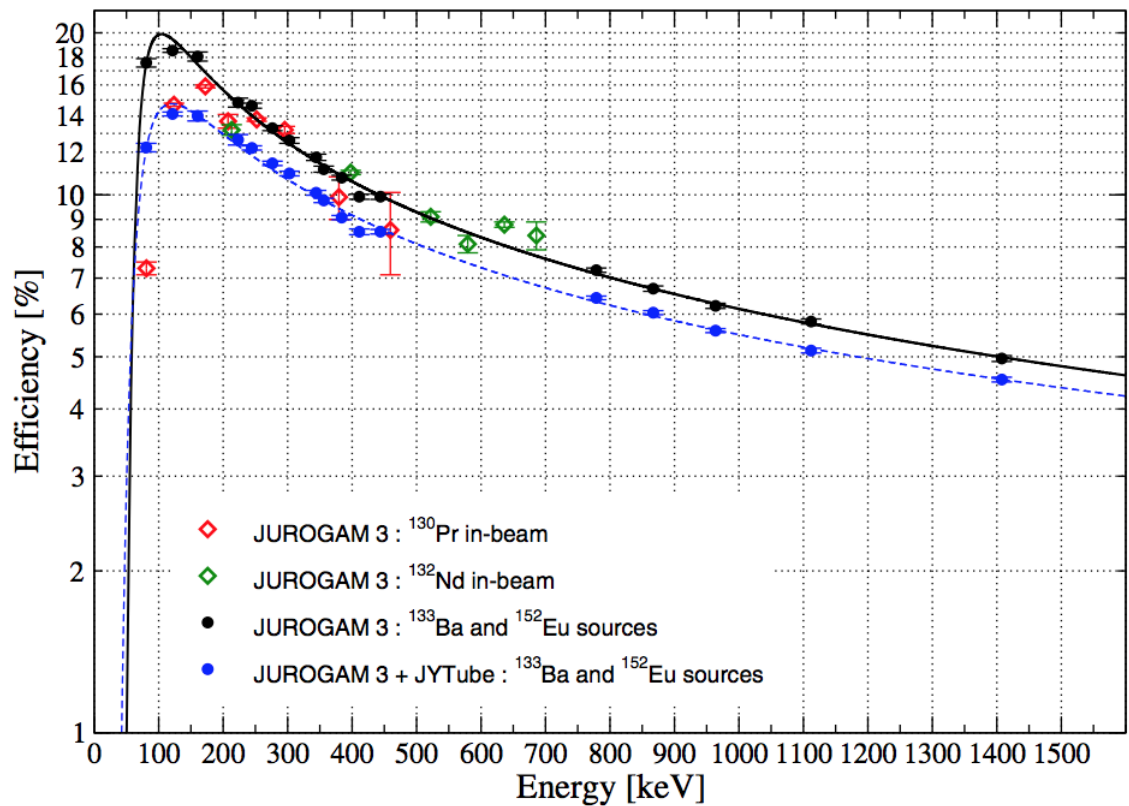
Figure 3.2: The gamma-ray detection efficiency of JUROGAM 3 [3].

3.2.5   Performance

The data taken for this thesis was the first experiment utilising JUROGAM 3, for which the recoil velocity was 5.7% of the speed of light, leading to a recoil transmission time through MARA of approximately 400 ns. Typically in an experiment involving JUROGAM 3 nuclei are moving at 1-8% of the speed of light and in flight γ rays are

Property	JUROGAM 3	GAMMASPHERE
Detector configuration	15 tapered	110 HpGe
	24 clover	
Solid angle acceptance of separator	10 msr	2 msr
Efficiency at 1360 keV	5 %	10 %

Table 3.1: A comparison of the properties of the JUROGAM 3 [3] and GAMMAS-PHERE [27] gamma-ray detector arrays.

emitted leading to the broadening of the γ-ray peaks, known as Doppler broadening, shown as

$$\Delta E = \frac{\nu}{c} sin\theta \Delta \theta E, \tag{3.1}$$

where ν is the velocity of the recoil, c is the speed of light, θ is the angle of the detector relative to the beam axis and $\Delta \theta$ is the opening angle of the detector. Doppler broadening has an effect on the FWHM, this is clearly seen when comparing the resolution values obtained using calibration sources and nuclei produced in-beam.

Absorbers are positioned in front of the detector modules, 0.50-0.64 mm of Cu and 0.23-0.26 mm of Sn, installed to prevent a high flux of X rays when the beam impinges on the target.

The operation of JUROGAM 3 with MARA does not alter the solid angle acceptance. When looking at similar combinations of devices, for example the operation of GAMMASPHERE [27], the gamma-ray detector array, with the FMA (Fragment Mass Analyser) [28], requires the target position to be moved from its nominal position, so the acceptance is reduced. GAMMASPHERE has a higher number of detectors and better efficiency therefore it has superior capabilities when it comes to γ-γ correlations. Looking at recoil-gated and recoil-decay tagged γ-ray spectra, JUROGAM 3 would have the advantage as it would produce a better total efficiency.

3.3   MARA separator

MARA (Mass Analysing Recoil Apparatus) [1, 2, 29] is an in-flight, vacuum-mode mass separator that was constructed for nuclear structure studies around the N≈Z line and

for studies beyond the proton dripline at JYU.

MARA was built with the motivation to compliment RITU (Recoil Ion Transfer Unit) [25] the gas-filled separator which has been used by the Nuclear Spectroscopy Group at JYU for nearly three decades to study the products of fusion-evaporation reactions in the region of the proton drip line. RITU was originally designed for experiments involving heavy nuclei with Z≥82 produced with asymmetric kinematics during fusion-evaporation reactions. Eventually RITU came to be used for experiments producing nuclei at the proton drip line lower in mass than originally intended, however a gas-filled separator is not optimal in the lighter mass region where separation of the beam is challenging during symmetric reactions, and not possible at all in inverse kinematics. As the mass-resolving power is very modest, a tag is required such as alpha particles or protons, however these tags are not possible in the lighter mass region. As research interests developed towards lighter nuclei, where the primary decay mode is beta decay, the need for a vacuum-mode separator became apparent. In order to achieve the necessary selectivity MARA, the in-flight mass separator, was designed.
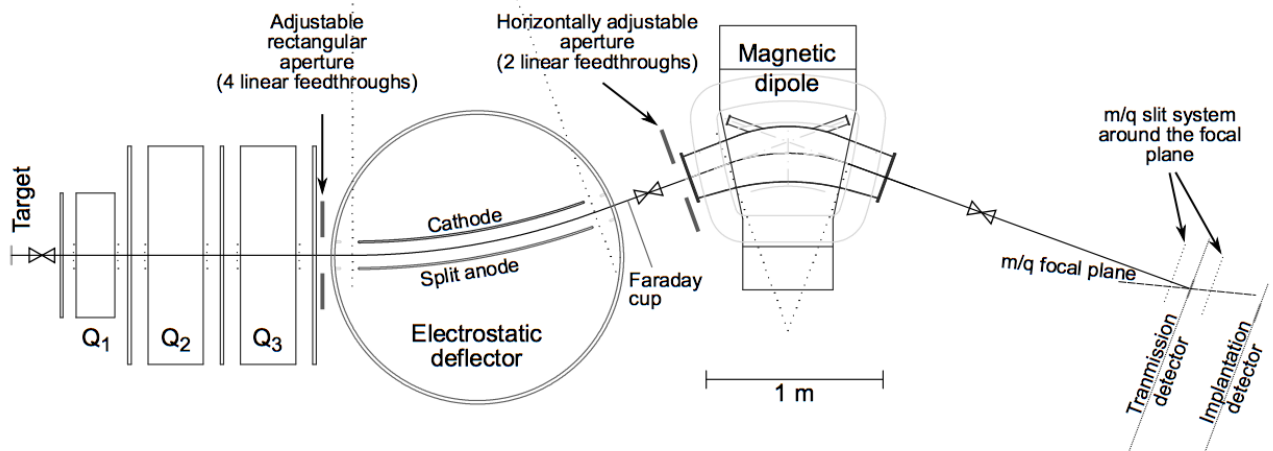
Figure 3.3: Layout of the MARA separator [29]

The MARA separator has a configuration of QQQEM (Figure 3.3): a quadrupole triplet followed by an electrostatic deflector and a magnetic dipole. The ion optics are described in detail by Jan Sarén [29]. MARA is not a symmetric device, contrary

to the majority of vacuum-mode in-flight separators. The quadrupole triplet spatially focuses products from the target position to as small an area as possible. It also creates a point-to-parallel focus between the target and the deflector and point-to-point focus from the target position to the focal plane as seen in figure 3.4. The electric deflector in combination with the magnetic dipole provides the energy focus at a fixed point at the focal plane. The magnetic dipole creates a mass dispersion and refocuses particles that were defocused by the electrostatic deflector. What remains is that the ions with varying m/q ratios are separated physically. By adding a small quadrupole component into the magnetic dipole using correction coils, the focal plane is variable along the optical axis by ± 30 cm. Energy slits are located between the dipoles, they are movable to allow the event rate at the focal plane to be limited. The focal plane is tilted so a double mass slit system is in place before and after the MWPC (Multi-Wire Proportional Counter). There are also movable aperture slits located at the entrance to the electric dipole. Sometimes the mass slits are positioned to allow just two charge states for a particular mass to be transported to the DSSD (Double-sided Silicon Strip Detector). The resulting mass-resolving power can be improved using both the energy and aperture slits but at the cost of acceptance. The quadrupole triplet allows for an infinite number of setting values of MARA, for example the angular acceptance can be increased at the cost of the mass-resolving power. The ion-optical properties of MARA can be seen in table 3.2.

MARA is a notable competitor amongst vacuum-mode recoil separators. As a comparison, in table 3.2 some ion optical properties of both MARA and the FMA [28] at Argonne national laboratory have been presented. The FMA (Fragment Mass Analyser) is a symmetric device running experiments in the same mass region as MARA. Both separators have their advantages and together advance fundamental nuclear research.

Several mass spectrometers exist around the world but most are longer than MARA due to employing two electrostatic deflectors located symmetrically either side of the magnetic dipole. In this type of layout the energy dispersion disappears after the second deflector so the focal-plane position can be moved in order to change the mass
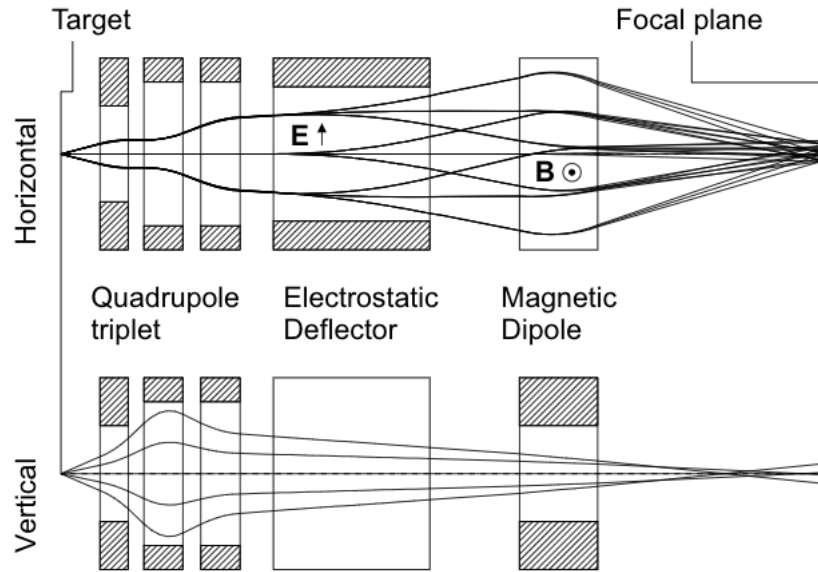
Figure 3.4: MARA optics shown in horizontal and vertical orientations. Trajectories are shown with different starting angles, masses and energies. [1].

Ion Optical Property	MARA	FMA
Overall length (m)	6.90	8.20
Configuration	QQQEM	QQEMEQQ
m/q dispersion	8.0 mm/%	10.0 mm/%
m/q acceptance	±7%	±7%
Energy acceptance (central m/q and angle)	-15% to +20%	±20%
Solid angle acceptance (central m/q and energy, msr)	10	8

Table 3.2: A comparison of the ion optical properties of MARA [2] and the FMA [28]

dispersion. MARA has a fixed point for the mass dispersion (the quadrupole component allows some flexibility to the focal plane) as the energy dispersion disappears at a fixed point after the magnetic dipole. MARA is therefore easier to construct, cheaper and the distance from the target to the focal plane is 6.9 m, shorter than majority of the vacuum-mode separators. The first order mass-resolving power is calculated to be 259.

3.3.1 Mass Separation

MARA uses the combination of the electrostatic deflector and magnetic dipole to separate the nuclei at the focal plane into different masses as described in detail by Sarén [29]. A charged particle moving in the presence of magnetic and electric fields is subject

to the Lorentz force

$$\vec{F} = q\vec{E} + q\vec{\nu} \times \vec{B}, \tag{3.2}$$

where E is the electric field, B the magnetic field, q the charge of the particle, and ν the velocity. The principle behind mass separation in MARA is rigidity which defines the ease with which a particles trajectory can be bent. By using the combination of field strength and bending radius, the field can be varied to bend charged particles by varying radii of curvature according to their masses.

When the velocity of a particle is perpendicular to a homogenous magnetic field, the particle is subject to a circular motion due to the Lorentz force which is perpendicular to the velocity and acts as the centripetal force, where the radius is given by ρ. The magnetic field component of the Lorentz force is given by the second term in equation 3.2. The rotation has an angular velocity of $\omega = d\theta/dt = \nu/\rho$, where the centripetal acceleration is given by $a = \omega^2\rho = \nu^2/\rho$ and $q\nu B = m\nu^2/\rho$. The magnetic rigidity can then be defined as

$$\chi_B = B\rho = \frac{m\nu}{q} = \frac{p}{q} = \frac{\sqrt{2E_k m_0}}{q} \tag{3.3}$$

where an ion has mass m and kinetic energy E_k.

When the velocity of a particle is perpendicular to an electric field, the particle moves in a circular motion as the force is perpendicular to the velocity, and the first part of the Lorentz equation describing the electric field component acts as the centripetal force, where $F = m\nu^2/\rho = qE$. The trajectory of an ion can therefore be described by the electric rigidity

$$\chi_E = E\rho = \frac{p\nu}{q} = \frac{2E_k}{q}. \tag{3.4}$$

The electric and magnetic fields are formed in such a way as to cancel the energy dispersion leaving purely a mass dispersion.

3.3.2 Important Quantities

The required excitation energy of a compound nucleus following a fusion reaction is given by

$$E^* = E_{CoM} + Q, \tag{3.5}$$

where E_{CoM} is the centre of mass bombarding energy and Q is the reaction Q-value, the amount of energy absorbed or released in the reaction. Q is defined as

$$Q = (m_t + m_b - m_c)c^2. \tag{3.6}$$

In a collision between a projectile or beam and target, the centre of mass energy can be calculated as

$$E_{CoM} = \frac{m_t}{m_b + m_t} E_{lab}, \tag{3.7}$$

where m_t is the mass of the target, m_b the mass of the beam and E_{lab} is the laboratory energy of the beam. E_{CoM} must be larger than the Coulomb barrier between two nuclei in order for them to form a compound nucleus. When the required excitation energy and reaction Q value are known, E_{CoM} can be taken from equation 3.5. Using equation 3.7, E_{lab} can be calculated, which is the energy at the middle of the target.

The Coulomb barrier for heavy ions can be approximated as

$$V_c = \frac{Z_A Z_B}{A_A^{1/3} + A_B^{1/3}} MeV. \tag{3.8}$$

The energy of the fusion recoil can be estimated as follows

$$E_{fr} \approx E_b \times \frac{m_b}{m_c} \times \frac{m_r}{m_c}, \tag{3.9}$$

where m_b is the mass of the beam, m_c the mass of the compound nucleus and m_r is the mass of the recoil.

The equations presented above are calculated at the middle of target (MoT), there-

fore in the next step the energy of the fusion recoil entering the separator has to be calculated. The energy required to leave the target is calculated by considering stopping energy in the target material which can be obtained from SRIM [30]. The energy lost within the carbon foils is also considered at this point. The resulting energy is used then to calculate the setting values of the MARA separator.

The cross section of a reaction is calculated using

$$\sigma = \frac{R}{I},\tag{3.10}$$

where R is the number of reactions per unit time per nucleus and I is the number of incident particles per unit time per unit area. This can be translated to

$$\sigma_R[\mu b] = \frac{A[\frac{g}{mol}]N_R[\frac{1}{sec}]}{I_{beam}[pnA]t[\frac{mg}{cm^2}](3.882)},\tag{3.11}$$

where N is the yield calculated at the target, A is the mass number of the target, t is the target thickness and I is the beam intensity in units pnA. 3.882 is a conversion factor between units.

3.4   Focal-Plane Detection System

MARA alone cannot achieve the desired selectivity so must be used alongside an efficient detector system. As a mass separator, MARA cannot separate isobars or fusion-evaporation channels that overlap causing m/q ambiguity. It is therefore necessary to have a highly selective detector setup at the focal plane as well as in-beam detector systems where possible.

The focal-plane detection system provides essential instrumentation to the MARA separator. The focal plane allows measurement of the position of a recoil, the time-of-flight and therefore the velocity, the energy as well as the energy loss. It is also possible to identify the mass of the recoil. The decay following the recoil can be detected and then correlated with the recoil. The versatile focal plane which is located at the end of MARA typically consists of a position sensitive MWPC, then 40 cm after the MWPC,

a DSSD is located where recoils are implanted. A second layer of silicon sits behind the DSSD for punch-through events, and in front of the DSSD an escape-particle silicon box detector. The punch-through detector and the escape particle silicon box detector are used to veto background events. By using a combination of two position-sensitive detectors it is possible to measure the velocity and incoming angle of ions.
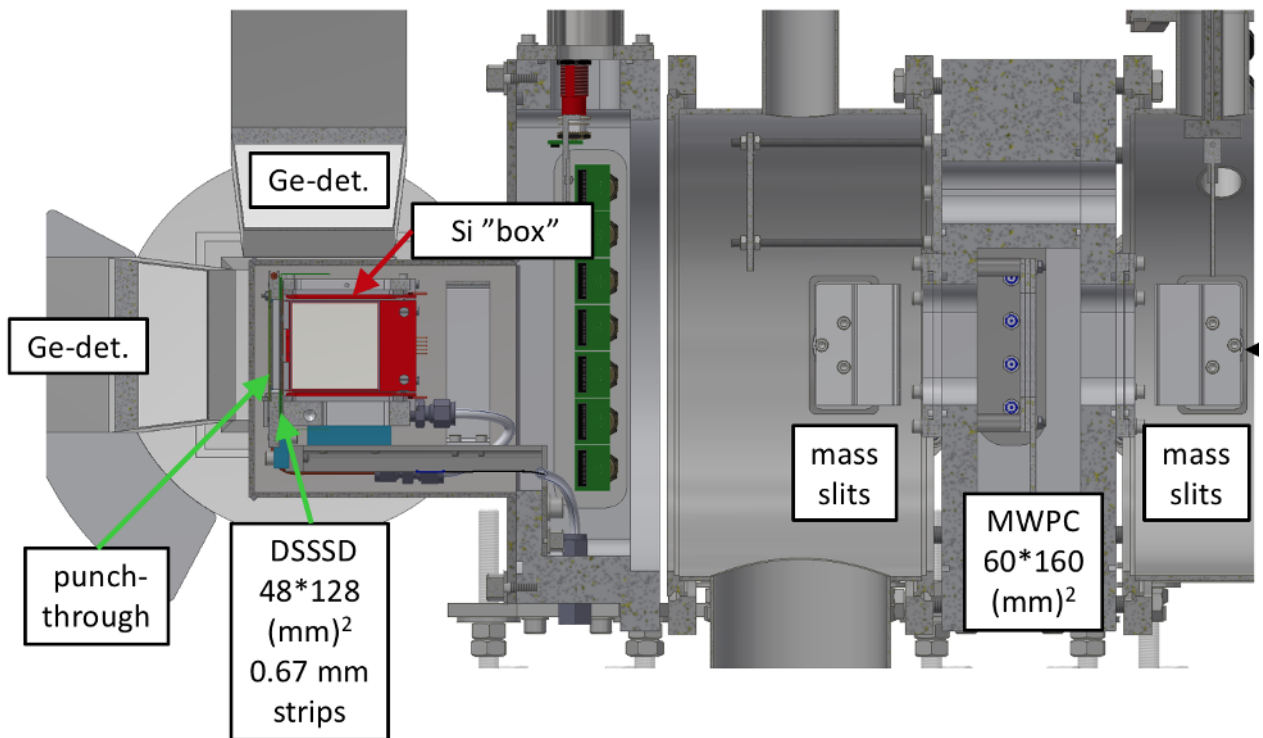
Figure 3.5: Diagram showing the MARA focal plane.

The silicon detectors are usually surrounded with an array of up to five germanium clover detectors and/or Broad Energy germanium detectors.

3.4.1 MWPC (Multi-Wire Proportional Counter)

The position sensitive MWPC is 160 mm wide and 60 mm high. It consists of three wire planes: x-plane, y-plane and the cathode which are made up of 20 μm thick gold plated tungsten wires with a separation of 1 mm. 2 ns delay lines are used between the wires (x and y planes) to provide position-sensitive information by recording the delay

between signals at both ends of the wire planes. The wire planes are separated by 3 mm from each other. Thin mylar foils of 240 μg/cm^2 thickness are used to separate the gas counter volume from the rest of the vacuum. Typically iso-butane gas is used in the detector at a pressure of 2 - 3 mbar and a voltage of -470 V is applied at the cathode plane. The MWPC provides an additional veto in identifying decay events by recognising those also seen in the implantation detector.

3.4.2   DSSD (Double-sided Silicon Strip Detector)

The primary detector associated with the MARA setup is the DSSD BB20 silicon strip detector which is highly pixelated with a pixel area of 0.45 mm^2 and a total of 13824 pixels allowing precise correlations between events. The total number of strips in the BB20 detector is 192 in the x-direction and 72 in the y-direction. The detector size is 128 mm in the x-direction and 48 mm in the y-direction with a strip width of 0.67 mm. Three different thicknesses are available, 700 μm, 300 μm, and 150 μm. The 300 μm detector was used in the M09 experiment and the 150 μm detector was used in the JM06 experiment. A three line alpha source consisting of ^{239}Pu, ^{241}Am and ^{244}Cm was used to gain match the DSSD strips for both experiments.

Time of Flight (ToF) is measured between the MWPC and BB20. The ToF vs. Energy plot provides the information between fusion recoils and scattered beam components.

The punch-through detector is used to measure those recoils and particles which travel through the DSSD with sufficient energy to not implant and therefore only deposit a partial energy in the DSSD. Those events which are measured in the punch-through detector are then vetoed. The escape-particle silicon box detector may similarly measure light particles like electrons, protons, alphas which only partially deposit energy in the DSSD and still have sufficient energy to escape the thickness of the detector.

3.5   Data Acquisition

In order to read and interpret physical events measured by the various detectors, a reliable data acquisition (DAQ) system is fundamental. Coincidences between the detectors are almost always necessary to be able to observe the desired nuclei so to increase the sensitivity and optimise collection the data should be collected and stored from each detector channel independently wherever possible and a common trigger signal should not be used.

The signals from detectors used in conjunction with MARA and JUROGAM 3 are processed by a digital DAQ. A total data readout (TDR) [26] method is used where channels are all triggered and run independently of each other and then associated within the software to reconstruct the events. Each detector signal is time stamped so that time and position correlations can be made between recoils and subsequent decays. All channels are connected to Nutaq (Lyrtech) digitizers.

Grain [31] is a data analysis system that was developed to be used in conjunction with the Total Data Readout DAQ. The event-building process and analysis are carried out completely in the software after the processing of the data stream. Grain provides an efficient event parser and software system written in Java, which has been used to process the data taken in this thesis work.

3.6   Recoil-Decay Tagging

When proton-rich nuclei below lead are produced during fusion-evaporation reactions the compound nucleus emits primarily protons. As described previously, many reaction channels are open and a system that is highly selective is required. Especially so when looking at in-beam data where multiple γ-ray transitions are emitted for every reaction channel. The strong channels dominate the number of events due to Compton scattering so the weaker transitions become hidden.

In the recoil-decay tagging method, the decay following the implantation of a recoil into the DSSD is observed in the same position as the recoil within a certain time

window. The implanted recoil can therefore be tagged with the unique signature from
the subsequent decay. As the recoils are identified using their decay properties the
prompt γ rays can be correlated with the recoils. In the experiments described in this
thesis, the recoils which are implanted at the MARA focal plane emit protons and these
were used to tag prompt γ-ray transitions detected using JUROGAM 3. An example
of the recoil-decay tagging technique in use at JUROGAM 3 is shown in figure 3.6.

The recoil-decay tagging technique was initially implemented at GSI [32]. The
SHIP separator was used in combination with NaI detectors to detect prompt γ rays.
At Daresbury the method was carried out for the first time using a recoil mass separator
combined with an array of germanium detectors [33] based upon studies by Sellin *et al.*
[34] in which the technique was developed utilising a DSSD. The background events
were significantly suppressed allowing very clean, time-correlated decay energy spectra
to be produced.

3.7   Recoil-Isomer Tagging

The recoil-isomer tagging technique [35, 36] is a selective method used to characterise
structures which are weakly populated above isomeric states. As previously discussed,
many nuclear states are produced during fusion-evaporation reactions. Correlations are
made between prompt and delayed events across long-lived isomeric states by utilising
devices, such as MARA in this case, that are able to separate beam particles away from
the recoil products reducing the background rates sufficiently to allow measurements
of isomeric decays. Similar techniques are commonly used in which the delayed events
are seen during a period of no beam allowing for the low background component,
however this technique allows far more structural data to be observed. So called 'recoil-
shadow' experiments allow observation of delayed events that follow the isomer, giving
no structural information on the states above. Prompt, in-beam data such as that
obtained from JUROGAM 3 is sensitive to states built above the isomeric state, but
not those below. The recoil-isomer tagging technique allows study of the feeding and
decay of an isomeric state.
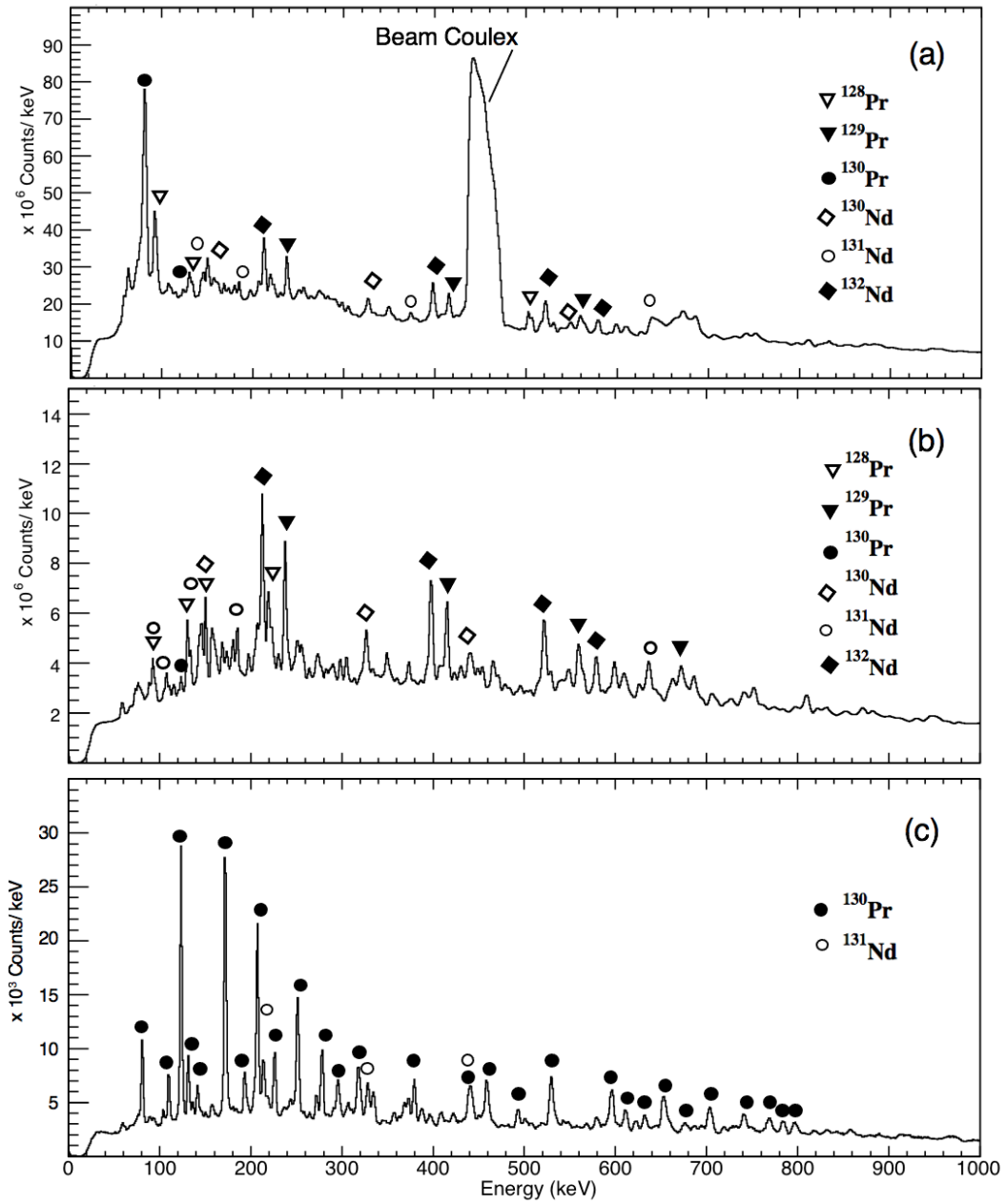
Figure 3.6: Gamma-ray energy spectra obtained with JUROGAM 3. Panel (a) shows gamma rays with just an addback condition applied. Panel (b) shows the gamma rays in coincidence with recoils seen at the MARA focal plane. Panel (c) shows gamma rays gated on the recoils and gated on an isomer observed at the focal plane.

Chapter 4

Proton Emission from Rare-Earth Nuclei in the A≈130 Region

This chapter surveys the rare-earth region where the best-known cases of deformed proton emitters lie, with a particular focus on the highly deformed nucleus ^{131}Eu which is predicted to have a quadrupole deformation amongst the largest in this mass region. The previous studies investigating ^{131}Eu including their successes and limitations are highlighted. The structure of nuclei within the vicinity of ^{131}Eu are considered in order to draw some conclusions on what might be expected from the structure and properties of ^{131}Eu. The experimental details of the two experiments, M09 and JM06, carried out as part of this thesis work are discussed.

Beyond the proton drip line, the nucleus is unstable and will not bind additional protons. The Coulomb repulsion does not allow nuclei with a large proton excess to be bound so the proton drip line lies relatively close to the β-stability line. The observation of ground-state proton emission, a relatively rare process, is an indication that the proton drip line has been crossed. During the 1990s there were great efforts to study proton radioactivity between the Z=50 and Z=82 closed shells as described by Blank and Borge [38]. There is great research interest in this area and as technology
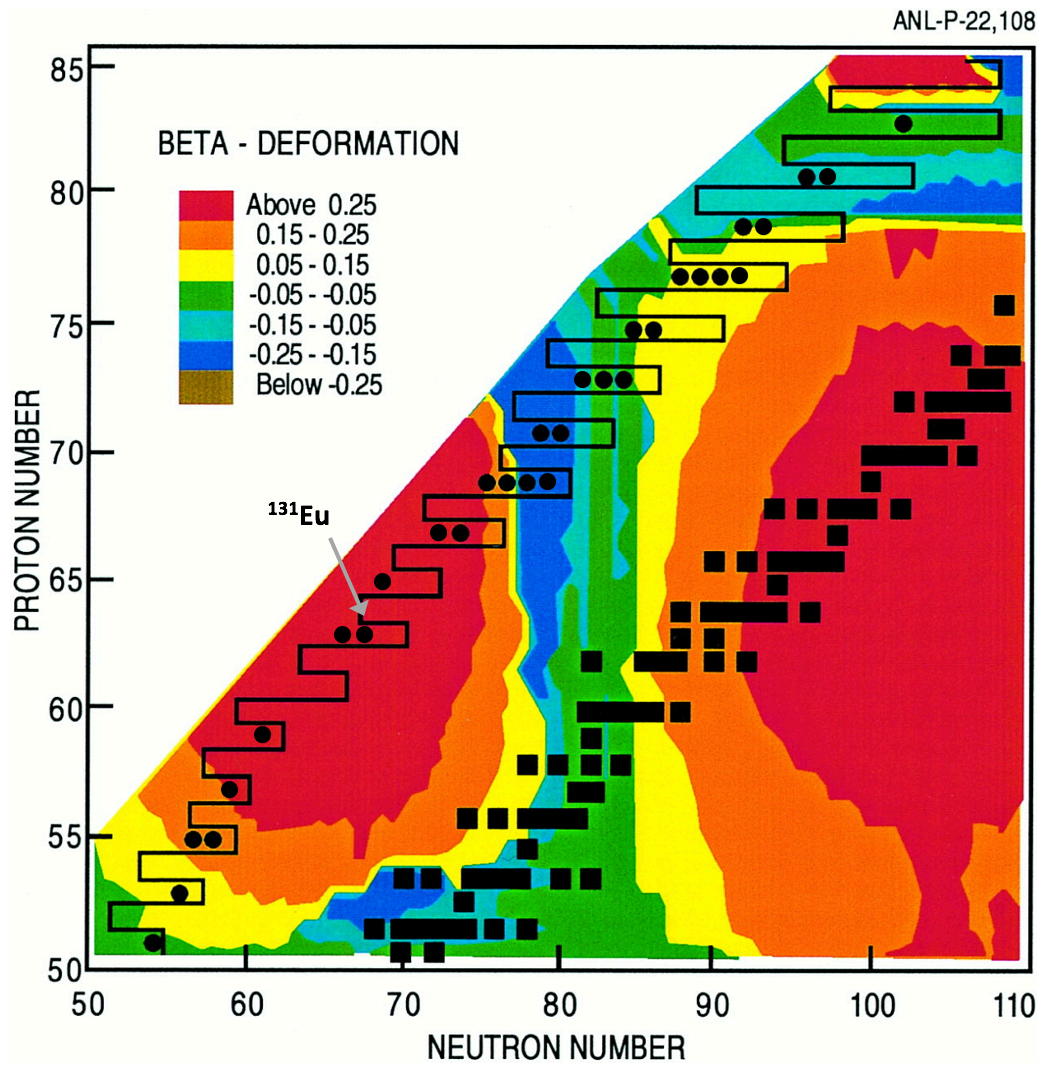
Figure 4.1: Region of the chart of nuclides around the proton drip line, displayed as a black line, showing deformation as a contour plot. Originally presented in ref. [37], the proton emitters are shown as black circles and have been updated to include those which have been discovered since original publication.

develops in the forms of mass separation and radiation detection, it is possible to explore more exotic, less stable nuclei which live for extremely short lifetimes.

For ^{131}Eu there are no data available on the excited states of the daughter nucleus following proton emission, the neighbouring isotones or the neighbouring isotopes. Data on excited states in this region is very limited, primarily to some transitions in the ground-state rotational bands in even-even nuclei. There are some nuclei with established bands based upon the $h_{11/2}$ orbital within odd mass nuclei. In nuclei with enough valence nucleons to make deformation possible, where Z > 50 and N < 82, it is common to observe bands based upon the $h_{11/2}$ orbital.

4.1   Z = 59

Wilson *et al.* [39] observed high-spin states in ^{125}Pr and identified excited states which were identified as five rotational structures. The ^{125}Pr nucleus is the most neutron-deficient Pr isotope with established excited states. The strongest band was identified as originating from the $h_{11/2}$ proton configuration up to a spin of $67/2^-$. Another structure was concluded to be based on the $g_{9/2}$ proton state, seen in many nuclei in this region and associated with those bands with enhanced deformation. A negative-parity yrast band in ^{127}Pr was identified by Parry *et al.* [40]. The nucleus was found to have a structure that differs from heavier odd-mass isotopes. The band was observed from the $11/2^-$ band head to spin $47/2^-$, interpreted as being based on the $h_{11/2}$ [541]3/2$^-$ proton configuration. Smith *et al.* [41] reported on observation of rotational bands of enhanced deformation in ^{127}Pr and ^{128}Pr. It was concluded that the band in ^{127}Pr was based upon the $g_{9/2}$ [404]9/2 proton configuration. When studying the dynamic moments of inertia versus N at low frequencies, the $\pi h_{11/2}$ or 'normal-deformed' bands show a differing trend to the $\pi g_{9/2}$ bands in $^{127-131}$Pr both experimentally and in theoretical models. Smith *et al.* did not observe links from the $\pi g_{9/2}$ band to the normal-deformed band in ^{127}Pr, however this could be because the bandhead state is isomeric. James *et al.* [42] reported the $9/2^-$ state in ^{129}Pr to be isomeric with a 60 ns lifetime. Weng *et al.* [43] reported on a delayed yrast band crossing in ^{129}Pr

at a frequency of 0.37 MeV which was interpreted as a result of the alignment of two $h_{11/2}$ protons. The enhanced-deformation rotational band in ^{131}Pr was discovered by Galindo-Uribarri *et al.* [44].

4.2 Z = 61

A negative-parity yrast band was identified in ^{131}Pm by Parry *et al.* [40] in the same study as described above. Differing in structure from heavier odd-mass isotopes, the yrast band of ^{131}Pm was observed from the $11/2^-$ band head to spin $47/2^-$, also interpreted as being based on the $h_{11/2}$ [541]$3/2^-$ proton configuration. Regan *et al.* [45] presented evidence for both signature partners in the $\pi h_{11/2}$ band in ^{133}Pm. Also established was a strongly coupled band built upon the $\pi g_{7/2}$ [413]$5/2^+$ configuration. Galindo-Uribarri *et al.* [46] measured the lifetimes of rotational bands in ^{133}Pm and deduced deformation parameters using the Doppler-shift attenuation method. A strongly coupled band based on the $g_{9/2}$ proton configuration was observed to the bandhead at spin $9/2^-$. This band has a deformation parameter of $\beta_2 = 0.40$ (5), which is similar to or even larger than the typical superdeformed bands in the mass $\sim$130 region [47].

4.3 Z = 62

Samarium can be considered as an even-even core to which a single proton couples to become Eu. By looking at the energy-level systematics in Sm with increasing neutron number, this could help to develop knowledge of the structure of excited states in Eu, however as already established, the information in this region is limited.

β-delayed proton emitter ^{129}Sm was produced and identified for the first time by Xu *et al.* [48] using proton-gamma-ray coincidences. The half life was determined to be 0.55(10) s. The spin and parity were assigned as $1/2^+$ (or $3/2^+$) which agrees with predictions made by Nilsson diagrams and suggests that the ground state is highly deformed with $\beta_2 \sim 0.3$. Until now ^{130}Sm has only been observed indirectly when the fine structure line was identified in reference [16]. Beta-delayed proton emission

in ^{131}Sm was identified with a 1.2(2) s half life by measurement of Pm X rays in coincidence with the delayed protons by Nitschke *et al.* [49], however no structural information has been found on the excited states. The states in the yrast band of ^{132}Sm were identified by Wadsworth *et al.* [50] up to $J^\pi = 16^+$. This is the closest even-even structure to ^{130}Sm so can be used to predict the structure above the 2^+ to 0^+ transition identified so far. The ^{133}Sm nucleus has far more structural information available. Regan *et al.* [45] observed two strongly coupled bands in ^{133}Sm thought to be built upon the $\nu h_{11/2}$ [523]7/2$^-$ and $\nu d_{5/2}$ [402]5/2$^+$ Nilsson configurations . A $\nu i_{13/2}$ intruder band was previously reported [51] and evidence was found for a second decoupled, negative-parity structure based on the $\nu h_{9/2}$ [541]1/2$^-$ orbital.

4.4   Z = 63

The ^{130}Eu nucleus was observed [52] and found to decay via emission of a proton with energy E_p=1020(15) keV and half-life $t_{1/2}$=0.90$^{+0.49}_{-0.29}$ ms to ^{129}Sm. The transition was assigned to a ground-state configuration of $J^\pi = 1^+$. Similar to ^{131}Eu, due to the characteristics found in the proton decay, ^{130}Eu is found to also be highly deformed with $\beta_2 \approx 0.3$ with the same $3/2^+$ ground-state proton configuration as ^{131}Eu. ^{132}Eu currently has no structural information available, however an attempt was made to study the nucleus within the work carried out in this thesis as described later in this chapter. To date, decay of ^{133}Eu has not been observed experimentally. The β-delayed proton decays of isotopes ^{134,135,136}Eu were studied in reference [53] where the first observation of β-delayed proton emission was made in europium isotopes. The ^{135}Eu nucleus was identified via Sm K$_\alpha$ X-rays after its electron-capture decay. Beta-delayed proton emission was assigned to both ^{134}Eu and ^{136}Eu based upon mass separation and following the observation of proton K X-ray coincidences.

The nearest europium isotope to ^{131}Eu with established excited states is ^{137}Eu [54, 55]. With sufficient data on the excited states in europium isotopes it would be possible to compare the energy level systematics of each nucleus between the closed shells with increasing neutron number. Deformation changes rapidly with increasing

numbers of valence nucleons in this region.

4.5   Z = 64

Eu can be considered as a proton hole in Gd, an even-even core, however very little is known about the Gd isotopes in this region. The nearest Gd isotope with known in-beam data is ^{138}Gd where the level scheme was developed over several studies [56–60], prompt-delayed gamma-ray coincidences were made across an isomeric state and allowed identification of low-intensity rotational bands. A $K^{\pi} = 8^-$ collective rotational band was established upon the 6 μs isomeric state [35, 61].

4.6   Z = 65

The ^{135}Tb nucleus was produced via the p6n fusion-evaporation channel [62] at the FMA where the emission of a proton was observed. The transition was assigned a configuration of $J^{\pi} = 7/2^-$. Both ^{135}Tb and its daughter ^{134}Gd are expected to have highly deformed, prolate shapes with $\beta_2 \sim 0.33$ [4]. It was concluded by Woods *et al.* [62] that the existence of a lower lying, ground-state $3/2^+[411]$ configuration could not be ruled out. The $3/2^+[411]$ Nilsson configuration was also predicted [**?**] to be the ground-state configuration for ^{131}Eu- this was ultimately confirmed when the fine structure was observed from that orbital [16]. In the ^{134}Gd daughter, based on a deformation of $\beta_2 \sim 0.33$, an excitation energy of $\sim$120 keV would be expected in the 2^+ excited state. An 8% fine structure branching ratio is predicted [62] for which there were corresponding events seen in the data. No firm conclusions were possible in this study regarding the proton decay fine structure for ^{135}Tb, however the results provide further data to constrain theoretical models of proton decay from deformed nuclei. Unfortunately the production cross section at $\sim$3 nb was too low for in-beam studies.

4.7 Z = 67

In 1998 [63] proton emission from ^{141}Ho and ^{131}Eu was successfully discovered. A proton-emitting state was discovered in ^{141m}Ho [64] which was interpreted to be the $1/2^+[411]$ state observed with $t_{1/2} = 8 \pm 3$ μs. The ground-state proton radioactivity was interpreted to be from the $7/2^-[523]$ state. In the same experiment proton emission from ^{140}Ho was observed with an energy lower than the emission from ^{141}Ho. For $Z \geq$ 69 nuclei that are spherical proton emitters the reverse energy dependence holds where Q_p increases with distance from the line of stability.

The Recoil-Decay Tagging method was utilised at the Fragment Mass Analyser at Argonne where the ground state was populated with a cross section of 250 nb and the isomeric state with a cross section of 50 nb [65] and evidence of the rotational bands in ^{141}Ho was found. Seweryniak *et al.* plotted the dynamic moment of inertia $\mathcal{J}^{(2)}$ as a function of rotational frequency for the rotational bands in both ^{131}Eu and ^{141}Ho as shown in figure 4.2. The $\mathcal{J}^{(2)}$ gradually increases until $\omega \approx 0.4$ MeV in the ^{141}Ho ground state band. The alignment of $h_{11/2}$ protons was expected to cause the first crossing at ≈ 0.25 MeV, however the dynamic moment of inertia of the ground-state band does not appear to display the crossing at that point. Seweryniak *et al.* suggested that this would suggest the band is built upon the $h_{11/2}$ orbital, as the crossing appears to be blocked.

The ground state of ^{141}Ho was calculated to have a deformation of $\beta = 0.29$, leading to the prediction that the ground state orbital is the $7/2^-[523]$ Nilsson orbital which originates from the $h_{11/2}$ spherical state. The rotational bands in ^{141}Ho were studied again by Seweryniak *et al.* [66] in 2001, where bands feeding both the ground state and the isomeric state were observed and the quadrupole deformation of the ground state was found to be $\beta_2 = 0.25(4)$ deduced from the extracted dynamic moment of inertia. The band crossings that were observed and the signature splittings agreed with the configuration assignments previously proposed. The ground state of ^{140}Dy is populated in the decay of ^{141}Ho from the ground and isomeric states so the spectroscopic information on ^{140}Dy was studied in [67] to draw conclusions on the proton emitting
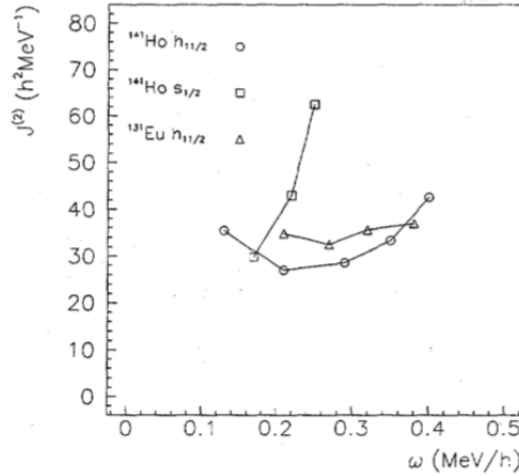
Figure 4.2: The dynamic moments of inertia for rotational bands in ^{131}Eu and ^{141}Ho as a function of the rotational frequency as observed in [65].

states in ^{141}Ho and determine the likelihood of observing a fine structure decay. The fine structure decay was first observed [68] to the 202 keV 2^+ excited state in ^{140}Dy with a 0.7(2)% branching ratio and $\beta = 0.23$-0.24 for the daughter nucleus. The decay properties of the $7/2^-$ and $1/2^+$ states in ^{141}Ho were investigated again [69] and for the first time fine structure was observed in the proton emission from different levels in the parent which is an odd-Z and even-N nucleus.

4.8   Previous Studies of ^{131}Eu

Davids *et al.* [63] first identified proton radioactivity from ^{131}Eu in 1998. The proton energy was measured to be 950(8) keV with an associated half-life of 26(6) ms. The Argonne ATLAS accelerator was used to produce a beam of ^{40}Ca ions at 222 MeV and an intensity of 4.5 pnA (particle nano amps). The target used was ^{96}Ru backed by a foil of 700 μgcm^{-2} Al resulting in a compound nucleus of ^{136}Gd. The target was bombarded for 36 hours. Using the FMA, 2 charge states were collected. Davids *et al.* used a predicted β^+ decay half-life of 147 ms, based on the values given in [70], to calculate the partial proton half-life to be 32(9) ms. In this experiment, the cross section of the proton decay of ^{131}Eu was estimated to be ∼90 nb from the yields of the

950(8) keV proton line. Davids *et al.* concluded in 1998 that the measured decay rates were indicative of large deformations below Z=69 and that further research including gamma-ray studies of proton decay from these highly deformed nuclei would be hugely advantageous in constraining theoretical models.
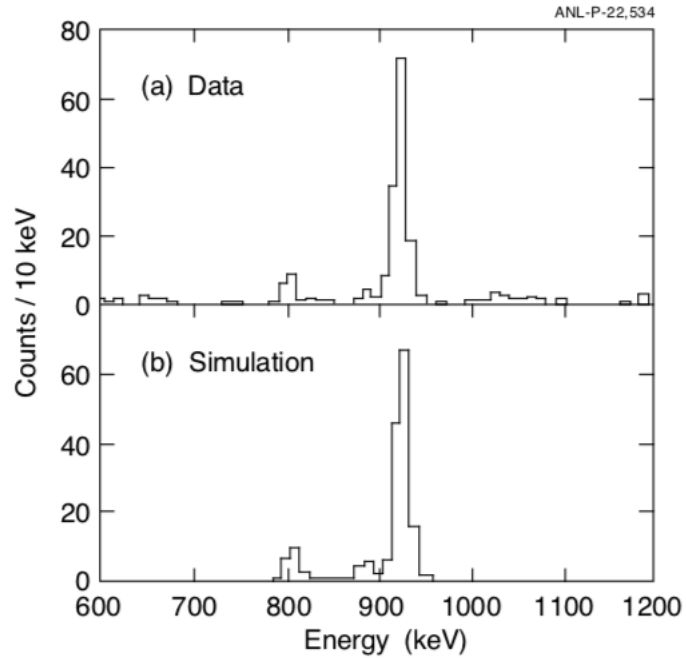
Figure 4.3: Fine Structure in the proton decay of highly deformed ^{131}Eu observed by Sonzogni et al [16] in 1999.

Identification of fine structure within the ground-state proton decay of highly deformed ^{131}Eu was first made in 1999 by Sonzogni *et al.* [16] using the FMA. In this paper they discussed the motivation behind looking for proton decay fine structure within highly deformed nuclei and explain that within the daughter nuclei the low-lying first excited 2^+ state is likely to receive significant decay strength compared to the ground state where the 2^+ state is sensitive to different elements in the parent wavefunction. The experiment was conducted at Argonne National Laboratory using the ATLAS accelerator system. A beam of ^{78}Kr ions at 402 MeV and 2 pnA intensity was incident upon a ^{58}Ni target of 0.77 mg/cm^2 thickness. Using the FMA, two charge states were selected and slits used to select the transmission of these particular ions into a 60um thick DSSD. A silicon strip box detector and an additional silicon detector

behind the DSSD were used to reject background events. Sonzogni *et al.* reported an estimated combined production cross section for the two proton peaks of ∼70 nb. The ^{131}Eu ground state proton transition was measured to be 932(7) keV with a half life of 17.8(19) ms. The fine structure proton transition was measured to have an energy of 811(7) keV and a half life of 23^{+10}_{-6}ms. Sonzogni *et al.* suggested that both proton groups originate from the ^{131}Eu ground state decay due to the fact that the two proton peaks have half-lives in agreement with each other and are separated by 121(3) keV. Sonzogni *et al.* concluded that the ground-state configuration of ^{131}Eu to be $3/2^+[411]$. In 1999, the small peak between the two proton peaks was also identified as the sum of 811 keV protons and K electrons. Based on the excited 2^+ energy Sonzogni *et al.* found that ^{130}Sm had a quadrupole deformation of $\beta_2= 0.34$ confirming the high pro-late deformation in the region on the proton drip-line below Z = 69 in agreement with Davids *et al.* [63].
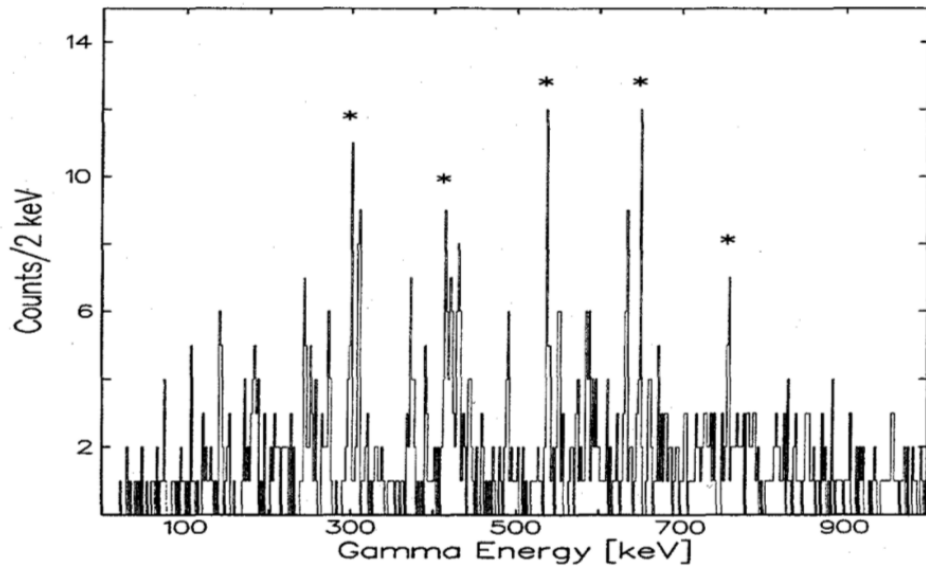
Figure 4.4: Singles spectrum of γ rays tagged with protons emitted from the ground state of ^{131}Eu, established in an experiment at ATLAS using FMA and GAMMAS-PHERE [65]. It was suggested that the peaks identified could be ideal candidates for an $h_{11/2}$ band.

In 2000, Seweryniak *et al.* [65] published the results of further study into ^{131}Eu, once again at ATLAS utilising GAMMASPHERE [27] in conjunction with the FMA [28]. A beam of ^{78}Kr beam at 402 MeV was used to bombard a 0.75 mg/cm^2 ^{58}Ni target. The proton tagged γ-ray spectrum obtained for the decay to the excited 2^+ state resembled the same tagged spectrum to the ground state decay confirming the idea that both proton decays within ^{131}Eu are in fact from the same state. Seweryniak *et al.* found the ground state proton decay rate to be consistent with theory for $3/2^+[411]$ as well as $5/2^+[413]$ as concluded by Davids *et al.* [63] yet the proton decay to the 2^+ excited state in ^{130}Sm was found to clearly favour a $3/2^+[411]$ assignment, similarly found by Sonzogni *et al.* [16]. Seweryniak *et al.* were unable to make any band assignments due to the complexity of the γ-ray spectrum and the low number of statistics. They did conclude that the transitions marked as shown in figure 4.4 could be ideal candidates for an $h_{11/2}$ band where the regular spacing of the transitions indicates that the first crossing is blocked. A deformation of $\beta = 0.34 \pm 0.05$ was obtained. The transitions remaining were concluded most likely to produce a strongly coupled band. As in previous studies in order to draw solid conclusions they suggested further research including γ-γ coincidence studies.

Systematic comparison was found to be difficult due to the lack of data in the region on excited states of proton-decay daughter nuclei. The sparsity of data is still problematic today.

4.8.1 Theoretical Models

The decay process in proton radioactivity from a theoretical viewpoint can be considered as a simple quantum tunnelling process through the Coulomb barrier in the daughter nucleus. The probability of barrier penetration and therefore the half-life of the decay is dependent on the reaction Q value and the orbital angular momentum of the emitting state. For nuclei that are considered to be spherically symmetric, a simple WKB tunnelling description is most appropriate [72]. In reality this is not the optimal solution as the nuclear many-body wavefunction cannot be completely separated into the parent
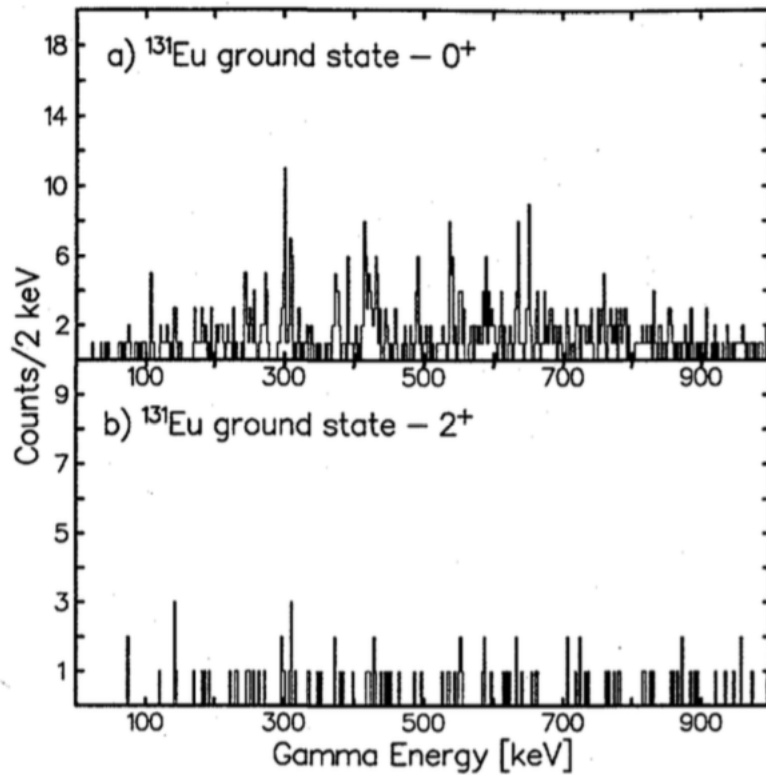
Figure 4.5: Spectrum of correlated γ rays with ground-state proton decay in ^{131}Eu to a) the ground state in the ^{130}Sm daughter, and b) the 2^+ state in the ^{130}Sm daughter [71].

and daughter. The decay is heavily influenced by factors relating to nuclear structure such as residual interactions and configuration mixing [73]. Within highly deformed nuclei such as ^{131}Eu, rotational effects change the orbital admixtures contributing to the nuclear wavefunction [74].

Proton radioactivity can be considered as a three-dimensional quantum mechanical tunneling problem. In its simplest form it involves just one proton tunnelling through the Coloumb barrier of the daughter nucleus however as the process cannot be completely separated into the proton and daughter elements of the nuclear many-body wavefunction, the process is far more complicated. Using the single-proton picture, a considerable amount of information can be determined: the angular momentum and spectroscopic factor in the majority of cases. In order to consider nuclear-structure

effects such as coupling between bound states and configuration mixing, further theoretical investigation is required.

There have been multiple efforts to model the behaviour of deformed proton emitters. In these attempts, the daughter nucleus was always assumed to have an infinitely large moment of inertia as a perfect rotor. Under these circumstances, all states in the ground-state rotational band can be considered as degenerate and therefore Coriolis coupling ignored. Kruppa *et al.* [73] made the first attempt to develop and move beyond simplified models previously encountered by using a technique based upon Gamow states. By modelling the daughter nucleus as a core the proton can be seen as moving in its average potential and the coupled-channel Schrödinger equation can be solved.

In 2000 Maglione and Ferreira [75] analysed the decay from ^{131}Eu to the first excited 2^+ state in the ^{130}Sm daughter nucleus. By reproducing the experimental half lives the deformation of the parent nucleus and the angular momentum of the decaying state were able to be determined. It is vital to have information other than the experimental ground-state decay energy to confine theoretical models as there are instances where more than one decaying state or value could reproduce the same data. When considering energy of proton decay, in theory, it should proceed primarily to the ground state in the daughter nucleus but as has been seen in the previous studies into the structure of ^{131}Eu when the first excited state is low in energy in rotational nuclei a significant branching ratio can be expected. Fine structure decay from a theoretical standpoint should be reproduced with the same angular momentum and deformation as the decay to the ground state. Maglione and Ferreira considered the emitted proton to be moving in a deformed single-particle Nilsson level, where the Schrödinger equation is solved using a deformed Woods-Saxon potential including a deformed spin-orbit term. By varying the depth of the nuclear potential, the real part of the resonance can be at the measured energy. The fine structure decay can be dealt with similarly. Maglione and Ferreira [75] determined the angular momentum of the ground state and deformation of ^{131}Eu in agreement with Sonzogni et al [16]. A further confirmation of their calculations and modelling was shown regarding ^{130}Sm. In all even-even nuclei,

the relation between the energy of the excited 2^+ state and the deformation can be given by: $E_{2^+} \approx 1225/A^{7/3}\beta^2$ MeV. Given that the 2^+ state was at 121(3) keV in the data set discussed the relation gives $\beta \approx 0.34$ which is in agreement with what would be expected proving the consistency of their calculations.

Further theoretical models describing proton radioactivity from deformed drip-line nuclei are documented in references [76–79], the content of which is beyond the scope of this thesis.

4.9 Experimental Details

4.9.1 M09

M09 was the experiment code for the first experiment carried out in this thesis work, referring to the use of the MARA separator. The primary aims of the M09 experiment were to search for beta-delayed proton emitters ^{133}Gd and ^{132}Eu using MARA in combination with the focal-plane detection system and JYTube charged-particle detector. In theory, studies into beta-delayed proton emission can offer significant structural information. If the β-decay component of the process occurs via electron capture, an X ray will follow in prompt coincidence with the proton allowing identification of the parent nucleus. When γ rays or X rays are emitted from the excited granddaughter nucleus in coincidence with the protons these may be used to identify the nucleus in question.

The experiment was performed at the University of Jyväskylä accelerator laboratory utilising the K130 cyclotron [22, 23]. A ^{58}Ni target was bombarded for approximately four days with a 3 pnA 373 MeV ^{78}Kr beam forming a compound nucleus of ^{136}Gd. The ^{132}Eu nucleus was produced via the p3n channel as can be seen in equation 4.1. The same target was also bombarded for approximately four days with a 3 pnA 340 MeV beam to produce ^{133}Gd via the 3n channel as can be seen in equation 4.2.

$$^{78}\text{Kr} +^{58} \text{Ni} \rightarrow^{132} \text{Eu} + \text{p3n}, \tag{4.1}$$
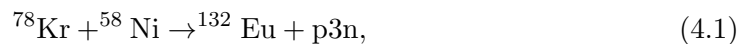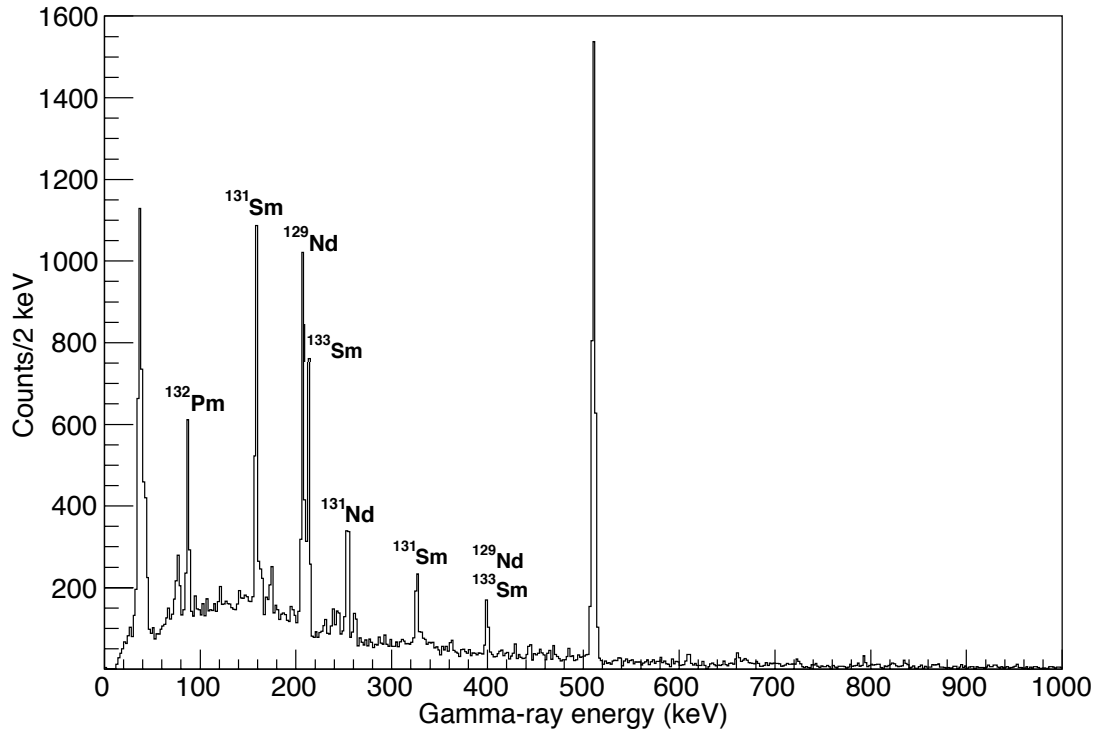
Figure 4.6: Gamma-rays associated with beta-delayed proton emitters produced during the reaction ^{78}Kr + ^{58}Ni →^{136}Gd* at an energy of 373 MeV in the M09 experiment.
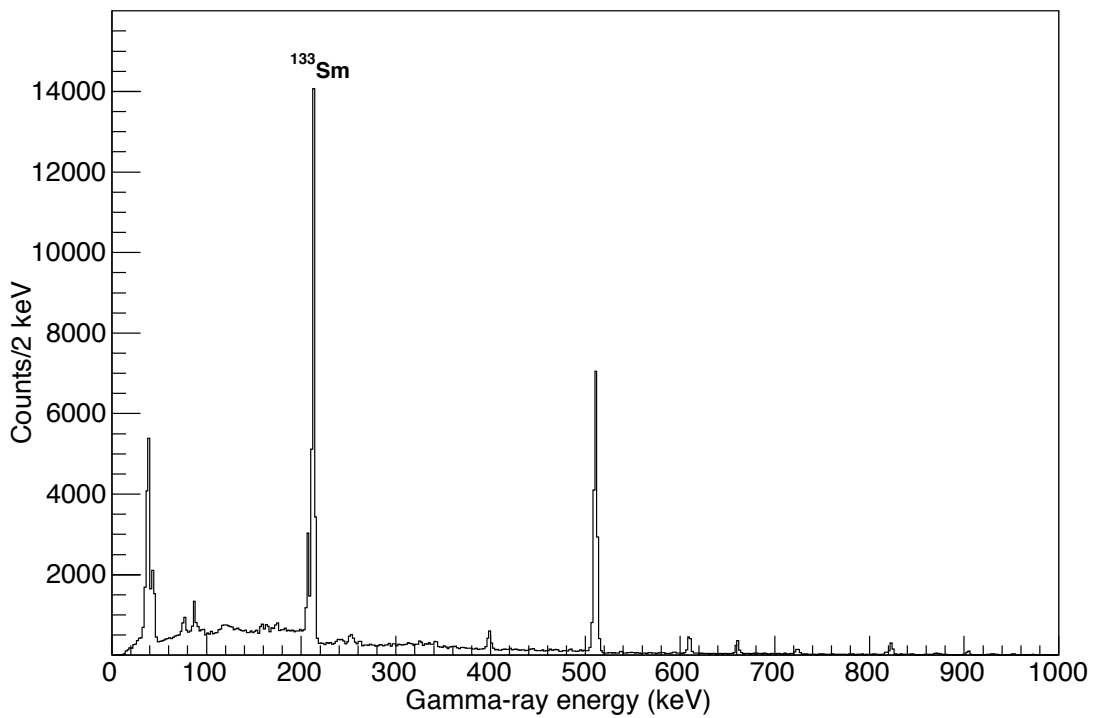
Figure 4.7: Gamma-rays associated with beta-delayed proton emitters produced during the reaction ^{78}Kr + ^{58}Ni →^{136}Gd* at an energy of 340 MeV in the M09 experiment.

$$^{78}\text{Kr} + {}^{58}\text{Ni} \rightarrow {}^{133}\text{Gd} + 3\text{n}. \tag{4.2}$$
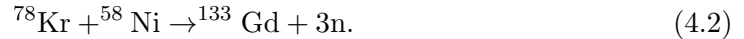
Unfortunately this experiment was not successful in the original aims and these nuclei were not identified. The production cross sections of some beta-delayed proton emitters in this region are very small compared to the yields of their isobars so it is very difficult to obtain structural information on these nuclei through conventional methods. The expected production cross sections for ^{133}Gd and ^{132}Eu are 100 nb and 1 μb respectively and the beta-delayed proton branches are expected to be small. Many other known beta-delayed proton emitters were identified and it was concluded that in order to carry out recoil-decay tagging with these cases we must run with much lower rates to minimise random correlations. BEGe (Broad energy Germanium) detectors that are now available at the focal plane have excellent energy resolution and efficiency at lower energies, such as when detecting X rays.

Although the search for beta-delayed protons ^{133}Gd and ^{132}Eu in experiment M09 was unsuccessful, the data still proved to be very useful. The data obtained allowed us to identify and confirm isomers observed again in JM06 as the experimental setup in M09 had the benefit of JYtube. Figure 4.6 shows the gamma rays associated with beta-delayed proton emitters produced at an energy of 373 MeV in the M09 experiment. Figure 4.7 shows the gamma rays associated with beta-delayed proton emitters produced at the lower energy of 340 MeV. Figure 4.8 shows the energy of the beta-delayed protons in coincidence with the associated gamma rays at the focal plane as produced in the JM06 experiment at an energy of 364 MeV. The energy is cut off at 1000 keV to reduce the beta background.

4.9.2   JM06

JM06 was the experiment code for the second experiment carried out in this thesis work, referring to the use of JUROGAM 3 in conjunction with the MARA separator. Lots of research and new data on proton emitting nuclei in recent years has prompted further interest in the area [80]. There are many hanging bands in this region, so using in-beam studies and isomer-decay tagging, it is possible to link them to the ground
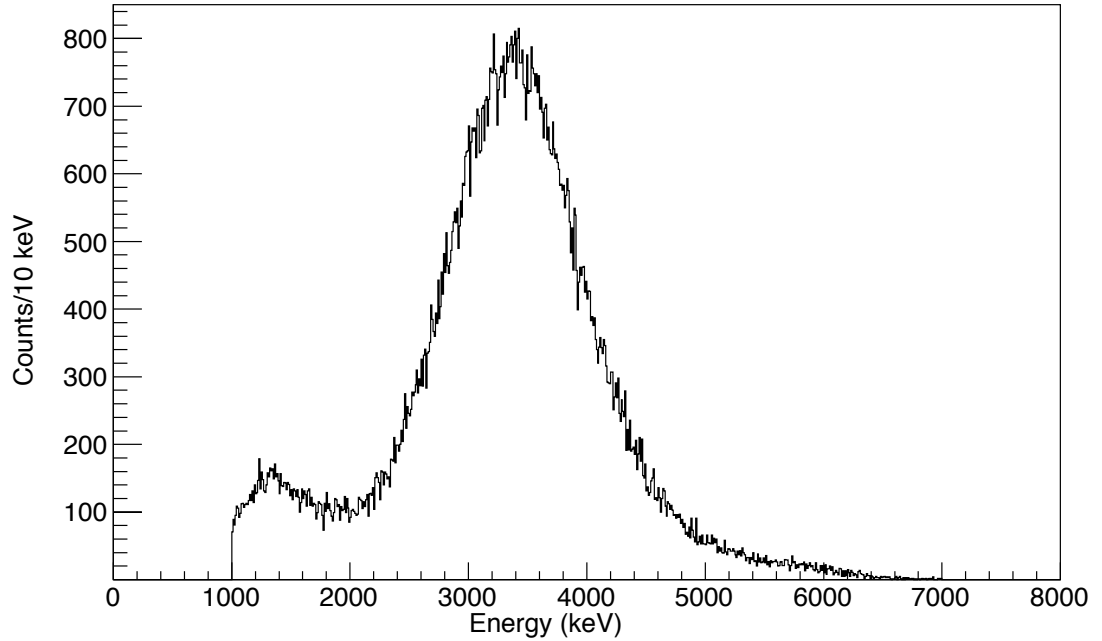
Figure 4.8: Beta-delayed protons in coincidence with the associated gamma rays at the focal plane as produced in the JM06 experiment at an energy of 364 MeV.

states. Developments in mass separation and gamma-detecting capabilities have led to the possibility of accessing areas of the chart that were not previously accessible.

As proton emission is sensitive to the potential in which the proton has to tunnel through, which is dependent upon the nuclear shape, it is expected that the emission of a proton will prove to be informative as to the nuclear shape. The most well known examples of deformed proton emitters are located in the 130≤A≤140 mass region. In order to understand these nuclei better, information is needed on the proton decay as well as data from the excited states. Predictions have been made as to the structure of low-lying excited states using non-adiabatic approaches but in order to constrain the models the quadrupole deformation must be obtained experimentally. By measuring the collective band structure, assuming the rotational model is valid, the moments of inertia can be deduced.

[131]Eu has been predicted to have one of the largest quadrupole deformations in this region with $\beta_2 \approx 0.3$. As the only highly deformed proton emitter in which fine structure has been observed in the proton decay, [131]Eu was identified as an ideal case

study. The fine structure is sensitive to the wavefunctions of the states in both the parent and daughter nuclides meaning there has been significant interest to theorists in this nucleus. The experiment was performed at the University of Jyväskylä accelerator laboratory utilising the K130 cyclotron [22, 23]. A 3 pnA beam of 390 MeV ^{78}Kr ions was used to bombard a 0.75 mg/cm^2 thick ^{58}Ni target over a period of 5 days, which resulted in a compound nucleus with an excitation energy of 76 MeV at the centre of the target. MARA was set to analyse ions with mass 131 and five charge states. Recoils were implanted into a 150μm thick DSSD. The experiment was run under these conditions for a total of approximately 9 days. In the latter part of the experimental run, the beam was re-tuned to 364 MeV, optimised to search for isomers. In addition to the MWPC and DSSD, the focal-plane detection system consisted of 5 germanium clover detectors and a punch-through silicon detector.

4.9.3   Expectations

The reaction of ^{78}Kr + ^{58}Ni was proven to be feasible during the MARA commissioning experiments detailed in [2]. With a cross section as low as 70 nb it was vital that the beam energy was optimised specifically to produce ^{131}Eu. Based on fusion-evaporation reaction calculations and the performance of the equipment, certain predictions were made as to what would be seen:

- MARA was expected to achieve a factor of two increase in transmission efficiency relative to FMA

- The initial aim of twelve days of irradiation was four times the amount of beam time in the experiment at FMA

- The aim was to increase the beam current by a factor of two from 3 pnA to 6 pnA

- JUROGAM 3 has a lower gamma-ray detection efficiency than GAMMASPHERE- a factor of 0.5

After taking into account these factors a yield of emitted protons of ≈ 2000 was estimated for the proposal which is roughly a magnitude larger than achieved with the FMA. Assuming this number was attainable, the gamma-ray singles spectrum would show a vast improvement over the previous experiment [65]. This would allow tagged coincidence analysis to be carried out.

In the proposal it was also expected that the ^{131}Sm nucleus would be observed.

4.9.4   Optimal Beam Energy Consideration

The initial reaction used by Davids *et al.* [63] in 1998 in the search for proton radioactivity from ^{131}Eu was

$$^{40}\text{Ca} + ^{96}\text{Ru} \rightarrow ^{131}\text{Eu} + \text{p4n}, \qquad (4.3)$$
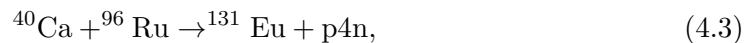
with a 222 MeV beam at an intensity of 4.5 pnA over a period of $\sim$36 hours corresponding to an excitation energy, E*, of approximately 77 MeV in the compound nucleus ^{136}Gd. The FMA [28] was set to collect A=131 recoils at the DSSD and charge states q= 22 and 23. ^{131}Eu was produced with a cross section $\sigma \sim$90 nb.

The study of ^{131}Eu by Sonzogni *et al.* [16] involved the following reaction with a 2 pnA beam at 402 MeV run for approximately 2 days

$$^{78}\text{Kr} + ^{58}\text{Ni} \rightarrow ^{131}\text{Eu} + \text{p4n}. \qquad (4.4)$$
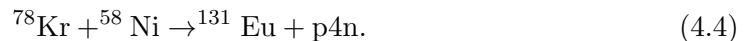
The resulting compound nucleus had an excitation energy, E*, of approximately 82 MeV at the center of the target. The combined production cross section of both protons emitted from ^{131}Eu was found to be 70 nb. The FMA was optimised to collect ions of A = 131 using mass slits to only allow transmission of charge states q= 32 and 33 into the DSSD. Fewer than 200 counts were recorded, with a transmission efficiency of 15%.

The reaction Q value in reaction 4.1 is calculated according to equation 3.6 to be 85.3 MeV using values obtained in reference [81]. The reaction used in the search

Isotope	Binding Energy (keV)
^{136}Gd	S(n)=12770
^{135}Gd	S(n)=11160
^{134}Gd	S(p)=1360
^{133}Eu	S(n)=13110
^{132}Eu	S(n)=11000
Total	49400 ≈ 50MeV

Table 4.1: Binding energies as estimated in [81] used to estimate the required excitation energy to evaporate 1 proton and 4 neutrons from the ^{136}Gd compound nucleus.

for ^{131}Eu in the present data taken produces the same compound nucleus of ^{136}Gd but is optimised for a p4n fusion evaporation channel. In a p4n reaction there are 1 proton and 4 neutrons to be evaporated. As it is not known in which order these evaporations will occur, it is reasonable to estimate. For example it could be assumed that initially 2 neutrons are evaporated, followed by 1 proton, then 2 neutrons. The masses and therefore the binding energies are not known, therefore estimates from mass evaluations [81] must be used as shown in table 4.1.

Additionally there is 3-4 MeV of kinetic energy per neutron and ∼12 MeV per proton required to allow them to escape the target, giving a total energy of approximately 26 MeV. The required excitation energy to evaporate the particles from the ^{136}Gd compound nucleus is therefore 76 MeV. The centre of mass bombarding energy can be calculated from equation 3.5 giving an energy of 162 MeV as the middle of target energy, E_{Lab} is calculated to be 380 MeV from equation 3.7.

The stopping power of the ^{78}Kr beam in ^{58}Ni is ∼30 MeV/mg/cm^2. The target thickness is ∼0.8 mg/cm^2 therefore the energy loss in the middle of target is 12 MeV and E_{lab} is equal to 392 MeV. From equation 4.1, V_c = 125 MeV and $V_c(E_{Lab})$ = 293 MeV. This is the minimum energy required for the nuclear reactions to occur.

The Coulomb barrier between a single proton and ^{130}Sm is ∼12 MeV. This is a good approximation to calculate the kinetic energy of a proton when evaporated. Using equation 3.9, ^{131}Eu has E_{fr} = 210 MeV. The stopping power on Ni = 53 MeV/mg/cm^2 leading to an energy loss of 21 MeV as the fusion recoil leaves the target. The stopping

power on the carbon foil (reset C-foil, thickness of 20 μg/cm^2) is 90 MeV/mg/cm^2 which leads to an energy loss of 2 MeV. This leaves a remaining energy of E_{lab}= 187 MeV which is used to calculate the MARA settings.

Chapter 5

Excited States in ^{131}Eu

This chapter presents the results of the data obtained at the focal plane detection system of MARA and the in-beam detection system at JUROGAM 3 during the JM06 experiment. The energy of the main proton emitted from the ground state of ^{131}Eu to the ground state in the ^{130}Sm daughter has been remeasured, as has the energy of the fine structure proton and the branching ratio. The gamma ray emitted in the 2^+ to 0^+ transition in ^{130}Sm has been directly observed for the first time. Using the recoil-decay tagging method the optimum conditions have been established to identify correlations between gamma-ray events. The in-beam data for ^{131}Eu has been improved upon and excited states have been identified. The previously unknown rotational band(s) have been constructed by observing gamma-gamma coincidences. The relative intensities of the gamma rays have been established. The results are discussed relative to what was expected and how the data correlates with nuclei in the region.

The typical rates measured at each detector during the search for excited states in ^{131}Eu in the JM06 experiment are shown in table 5.1.

Beam intensity	3.0 pnA
Tapered detector count rate	7.5 kHz
Clover detector count rate (one crystal)	5.0 kHz
Focal plane MWPC detector count rate	8.5 kHz
Focal plane implantation detector rate	5.9 kHz
Data transfer to storage	2400 kB/s

Table 5.1: Typical rates recorded during ^{131}Eu experiment as seen in [3]

5.1   Proton-Emission Spectroscopy

Previously no transitions in ^{130}Sm had been directly observed. As described in the previous chapter, Sonzogni *et al.* [16] observed fine structure in the ground-state proton radioactive decay of ^{131}Eu in 1999. The ground-state to ground-state transition was measured to have a proton energy of 932(7) keV and a second proton peak was observed with an energy of 811(7) keV. It was concluded that this was representative of the proton decay from the ground state of ^{131}Eu to the first excited 2^+ state in ^{130}Sm the daughter nucleus. The 2^+ excitation energy in the ^{130}Sm daughter was assumed to be 122(3) keV.
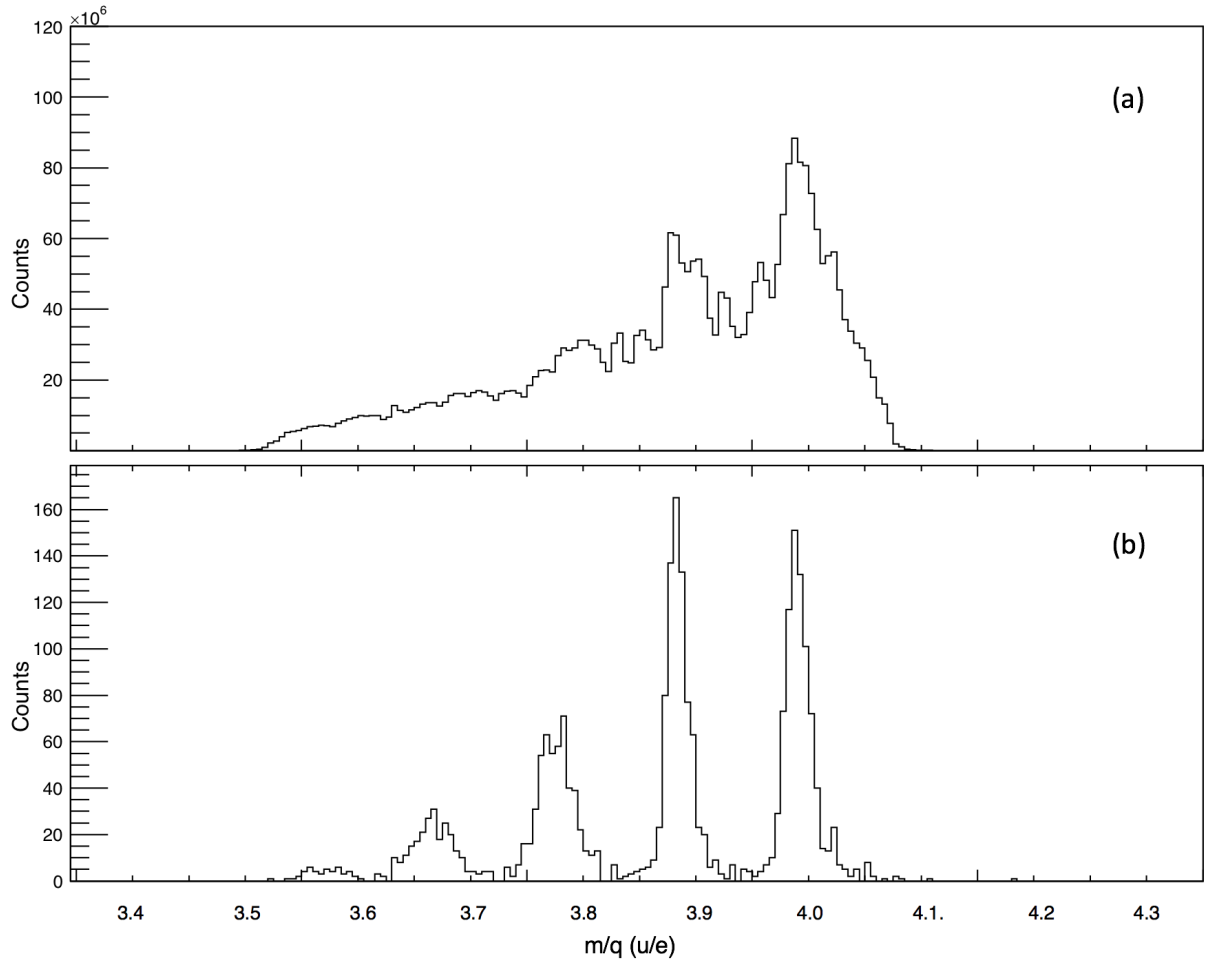
Figure 5.1: Mass to charge ratio spectrum collected in the MWPC at the focal plane of MARA including events that are (a) defined as recoils (b) in coincidence with the ^{131}Eu protons.

In the data taken for this thesis, five charge states (33, 34, 35, 36, 37) were collected in the MWPC as can be seen in figure 5.1. Panel (a) shows the spectrum produced in the gas counter including only those events defined as recoils. At this high excitation energy a lot of evaporation channels are open 'smearing' the recoil-gated mass spectrum. Panel (b) was created by gating on the protons emitted from ^{131}Eu produced at a beam energy of 390 MeV. As can be seen, the mass separating capabilities of MARA negate the need for mass gating as the spectrum is remarkably clean after tagging on the ^{131}Eu protons and the masses and charge states of mass 131 are clearly separated.

Figure 5.2 shows the decay-energy spectrum in the DSSD from the entire experimental run under various conditions. There is a large beta background created in this reaction, therefore the primary focus of sorting the data is to differentiate between proton events and beta events. This is a difficult task as the proton peaks being searched for are obscured by the beta background. The aim is to minimise the beta background by adding various selection conditions to the events.

The events shown in figure 5.2 must be 'decay' events, i.e. the decay products of recoils implanted in the DSSD. Decay events therefore originate in the DSSD and must also occur in the same pixel as a recoil, which is an event that triggers both the MWPC and the DSSD. A time gate of 320 ns is defined between the MWPC and DSSD as the lowest value for the time of flight of a product that can be considered from something that is flying, i.e. it has travelled through MARA. Below this value the event may be a decay.

The next condition added is a veto for events that are also recorded in the punch-through silicon detector as described in Chapter 3. These are events which are too high in energy to be stopped by the DSSD and therefore travel through into the silicon behind.

A 'one-pixel' condition was added in which there is a requirement for events in the DSSD to occur only within one pixel. This helps to distinguish between proton events and beta events. Beta particles have a longer range and can escape one pixel whereas the protons are implanted in the detector and deposit all of their energy, such that they

Figure 5.2: Proton-decay spectrum under various selection conditions: (a) 50 ms search time (b) 50 ms, punch-through vetoed (c) 50 ms, punch-through vetoed, one pixel (d) 50 ms, punch-through vetoed, maximum x-y energy difference 60 keV (e) 50 ms, punch-through vetoed, one pixel, maximum x-y energy difference 30 keV
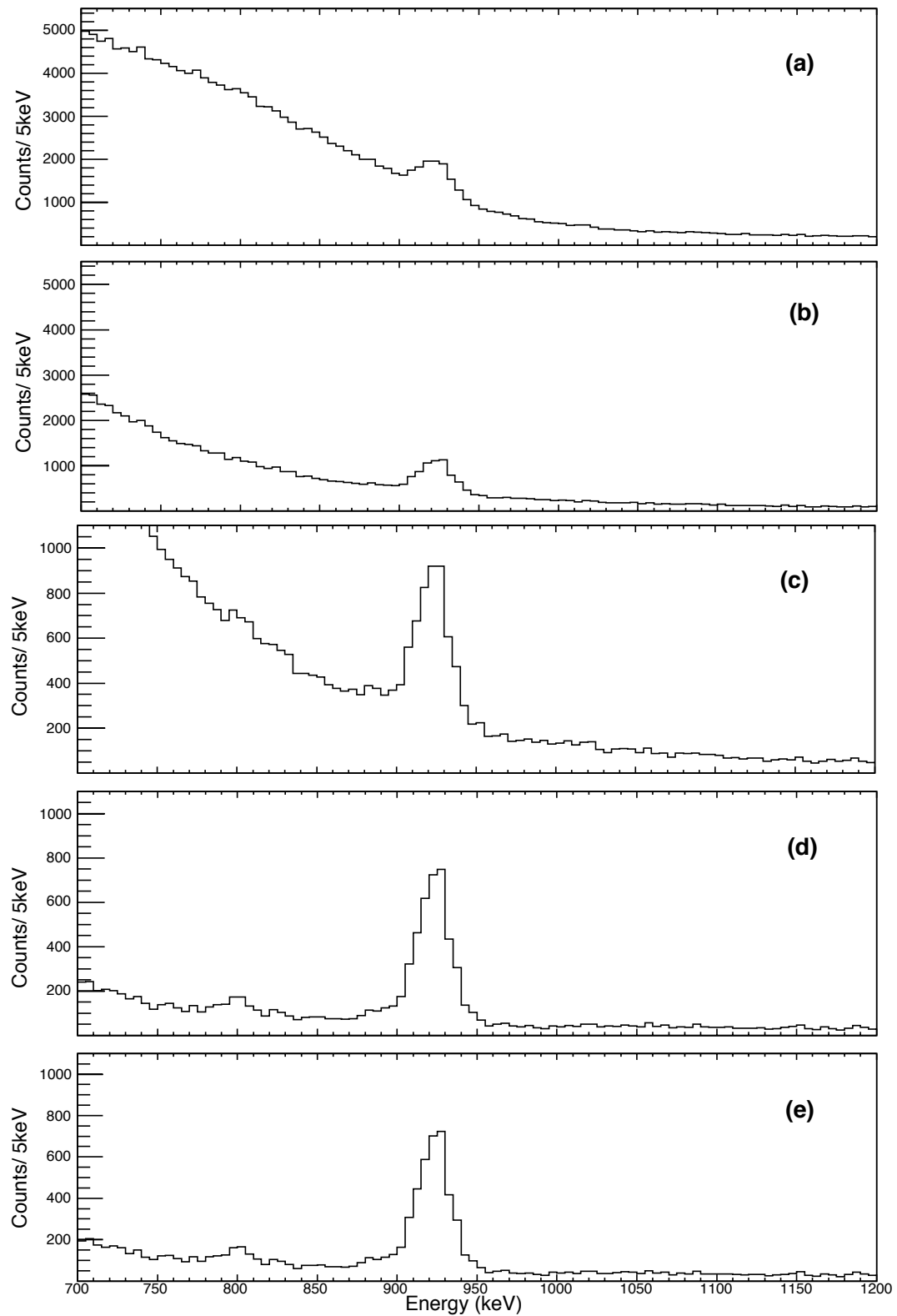
should not travel out of the pixel.

A maximum energy difference between the x strips and y strips in the DSSD was introduced to once again try to minimise the beta background. Beta particles may lose energy in the first pixel then travel into a second pixel however not meet the threshold energy to register in the second pixel. Therefore the beta particle would fulfill the one pixel condition but could deposit energy in a strip after travelling. A maximum energy difference of both 30 keV and 60 keV was tested between x and y strips as the proton events should fulfill these conditions, whereas the beta events are less likely to. The difference in the spectra with 30 keV and 60 keV maximum energy differences are not significant so it was decided to use the 60 keV energy difference.

From figure 5.2, it was concluded that the optimum conditions to reduce the beta background while ensuring valuable proton events were not lost were punch through detector vetoed, one-pixel, maximum x-y energy difference of 60 keV. As described at the beginning of this chapter, the mass selection resulting from MARA is very clean. When adding a mass selection criteria to the search via mass gating, the background is significantly reduced however the impact on the proton counts is large and many events are lost due to the strong 'tails' in the mass spectra. It is therefore not necessary to add mass selection when applying recoil-decay tagging.

A consideration when searching for the proton events within a large background is the search time. In figure 5.3, various search times were tested to see in which both the fine structure and main proton lines were most clearly visible, while also making sure proton events were not lost. The half life published by Sonzogni *et al.* [16] for the main proton line was 17.8(19) ms and 23^{+10}_{-6} ms for the fine structure so an estimation for the search time was based on number of half lives. Starting with 25 ms, approximately one half life, both proton lines are visible. Panel (b) at a search time of 50 ms appears to show both lines quite clearly but with more events. Panel (c) at a search time of 100 ms shows the two proton lines with a similar number of statistics but a much larger background. From 150 ms and above, it is clear that the background increases substantially whereas the number of proton events remains almost the same. Therefore

50 ms was chosen as the optimum search time when looking for the proton-tagged events.

The final spectrum used to define the proton energy, as shown in 5.4, is recoil-gated with punch-through events vetoed, under a one-pixel condition with a maximum energy difference between x and y of 60 keV and a search time of 50 ms. The main proton was measured to have an energy of 923(5) keV with 3365 counts in the peak.

When tagging on the fine structure proton, in a coincidence spectrum of proton events in the DSSD against events in focal plane germanium detectors, a gamma transition can be observed with an energy of 125(1) keV as seen in figure 5.5. This is consistent with the proton decay Q value differences measured by Sonzogni *et al* [16]. The bottom panel in figure 5.5 shows the energy spectrum in the DSSD gated on the 125(1) keV transition seen in the focal plane germanium detectors. The fine structure proton line in ^{131}Eu is clearly visible showing that the 125(1) keV gamma is in coincidence, proving that the transition belongs to the ^{130}Sm daughter. The small peak to the left of the fine structure peak is simply beta background. This was confirmed by increasing the width of the energy gate.

When tagging on the main proton line, the 125(1) keV peak is not visible in the focal plane germanium spectrum confirming that 125(1) keV is the transition from the 2^+ to the 0^+. No other peaks can be observed when gated on the main proton line.

As can be seen in figure 5.4 the fine structure proton line is difficult to fit accurately. Looking at the coincident spectra between events in the focal-plane germanium detectors and those events in the DSSD, a gate was added on the 125(1) keV transition to fit the fine structure proton more precisely. The energy of the fine structure peak was measured to be 799(6) keV.

5.1.1 Calibration

Davids *et al.* [63] measured the energy of the main proton emitted from ^{131}Eu to be 950(8) keV and used the 1051(4) keV peak in ^{147}Tm for calibration and gain matched using an external triple alpha source. Sonzogni *et al.* [16] measured a main proton
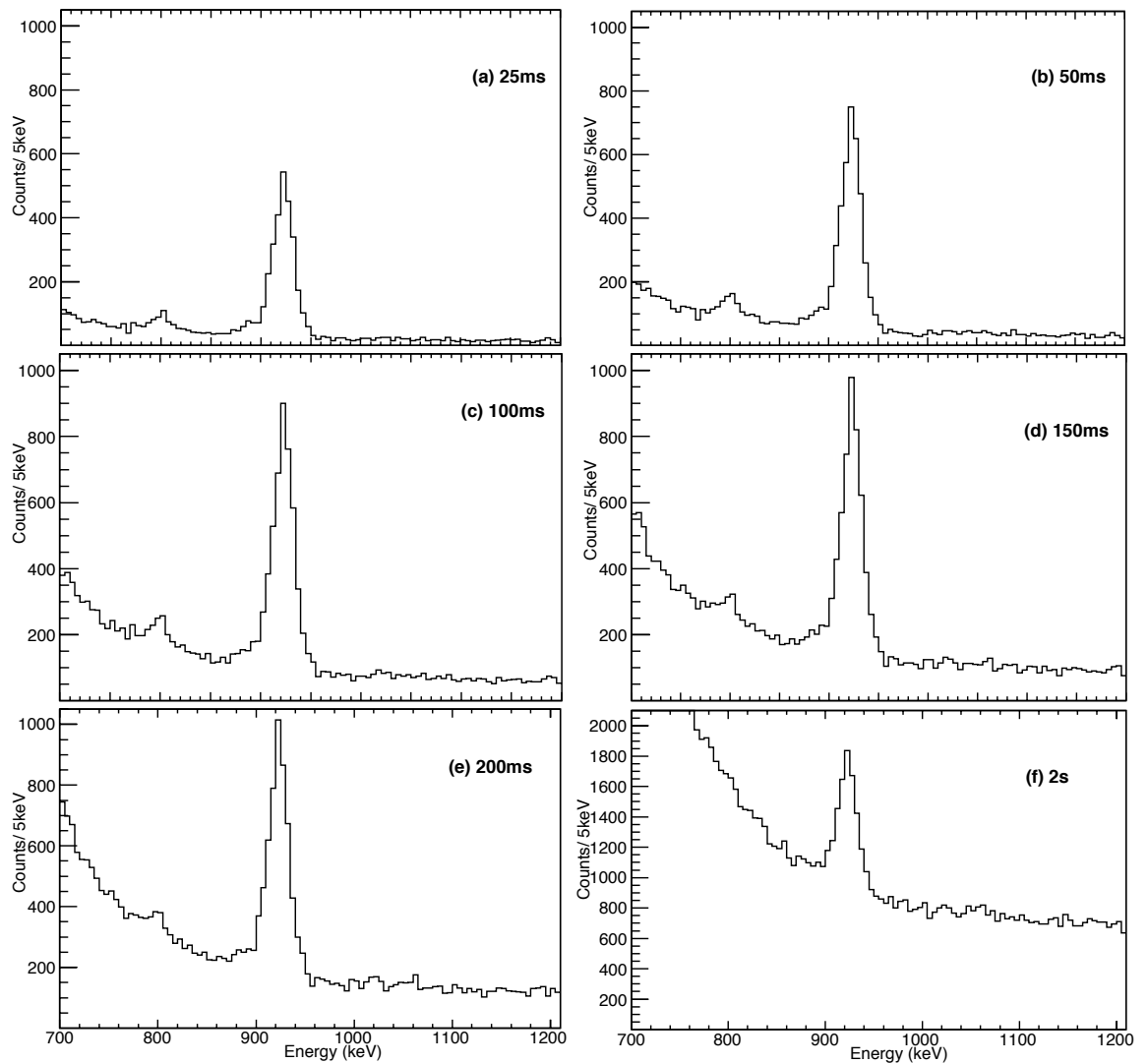
Figure 5.3: Decay energy spectra in the DSSD shown with varying search times. The two proton lines in ^{131}Eu are visible. The 50 ms search time was chosen to be optimal as the background is reduced sufficiently without compromising the number of proton events.
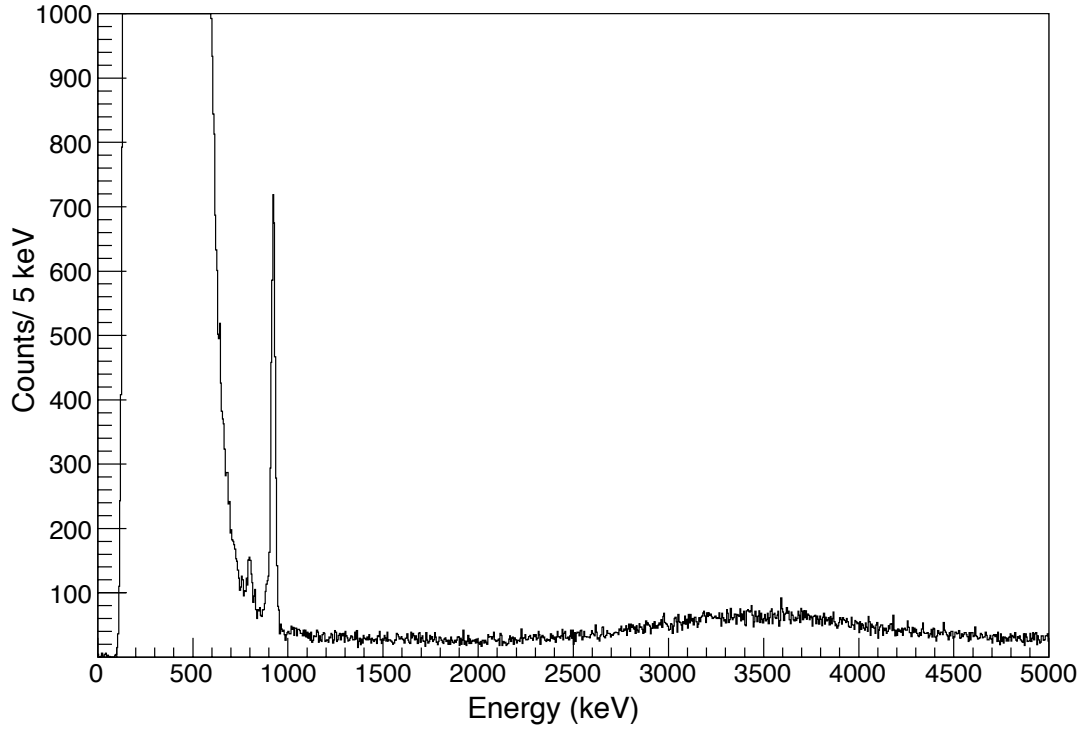
Figure 5.4: Decay energy as seen in the DSSD showing the two proton lines in ^{131}Eu, applying a 50 ms search time, vetoing punch-through events, with a one-pixel condition and a maximum x-y energy difference of 60 keV. The large beta background can be seen below ~1000 keV and the beta-delayed protons in the 2500-4000 keV energy range.

energy of 932(7) keV and 811(7) keV for the fine structure proton using the 1064(6) keV peak in ^{167m}Ir for calibration and gain matched using an external triple alpha source. It is surprising to see an 18 keV difference in the energy values reported in these two studies because the proton energy in ^{167m}Ir was originally measured to be 1064(6) keV by Davids *et al.* [82] using the 1051(4) keV line in ^{147}Tm for calibration. In this study the implanted alpha activities were used for gain matching and the proton line was used for offset. In an experiment utilising the SHIP Penning trap mass spectrometer, Rauth *et al.* measured the mass excess in ^{147}Tm to be -35969.8(10) keV [83] giving a proton separation energy of -1066(13) keV. Using mass tables [81] the mass excess in ^{146}Er is -44322(7) keV with S_p= -1059(3) keV. This raises the question as to why the ^{147}Tm mass excess is given as -35974(7) keV. Using the more accurate value for ^{147}Tm in combination with the AME values [81] for the mass of ^{146}Er, S_p= -1063.9 keV gives the proton energy as E_p= 1056.7 keV, which is ~6 keV higher than the original energy
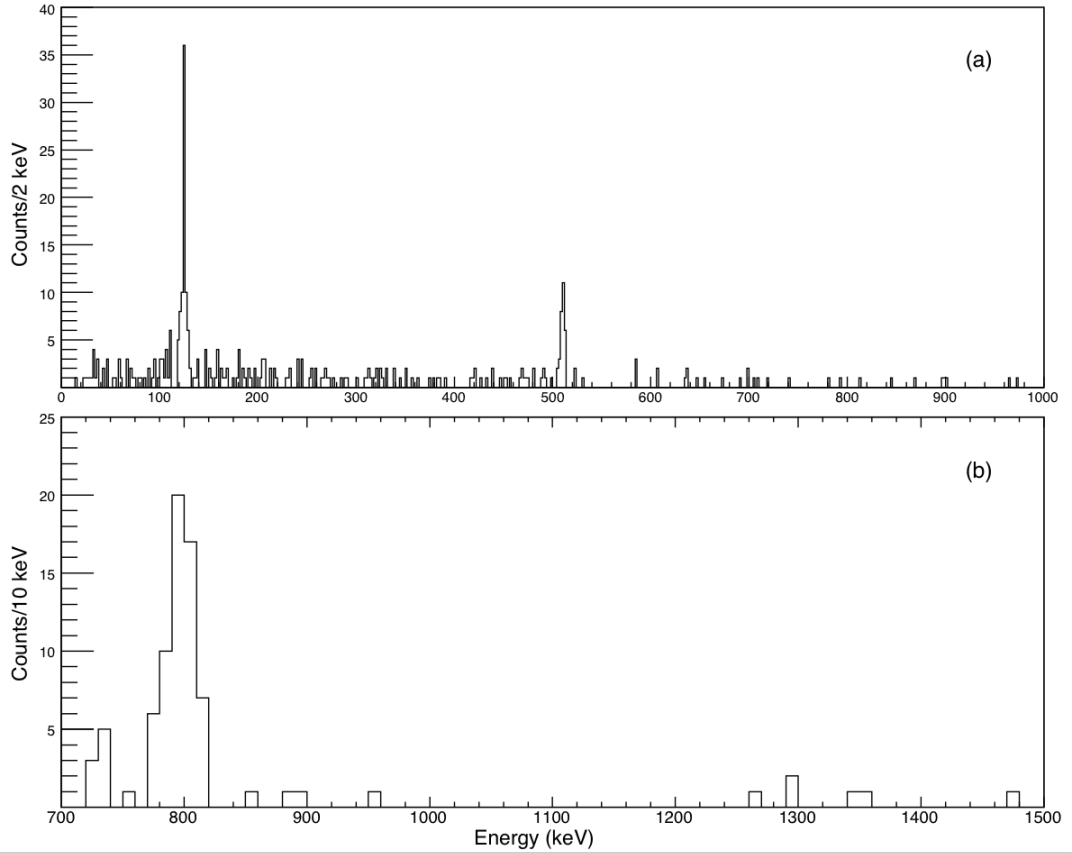
Figure 5.5: (a) The focal plane spectrum gated on the fine structure proton in ^{131}Eu showing the transition from 2^+ to 0^+ in the ^{130}Sm daughter. (b) The decay energy spectrum in the DSSD gated on the 125(1) keV gamma from the 2^+ to 0^+ transition in the ^{130}Sm daughter.

of 1051 keV.

In the data taken for this thesis, no separate proton calibration data was collected, instead the proton energies were measured using three line alpha calibration, ^{239}Pu, ^{241}Am, ^{244}Cm. The main proton line from ^{131}Eu was measured to be E_{p1}: 923.1 keV, and the fine structure proton line, E_{p2}: 798.5 keV (shown to this accuracy for purposes of the following calculation).

Hofmann *et al.* [84, 85] and Lennard *et al.* [86, 87] studied the pulse-height response of silicon semiconductor detectors. It was concluded from these studies that for a given ion the pulse height is not a linear function of the energy deposited. Since an external source was used for calibration and the proton activity was implanted into the silicon detector, some corrections to the obtained energies could be carried out in this data
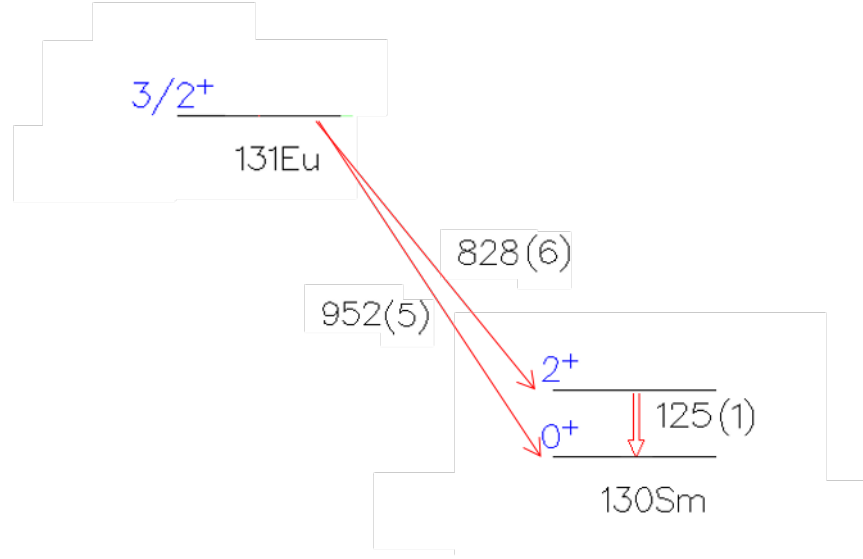
Figure 5.6: Level scheme showing the proton emission energies for the transitions from the ground state in ^{131}Eu to the ground state in ^{130}Sm and the first excited 2^+ in ^{130}Sm. The identified transition from 2^+ to 0^+ in ^{130}Sm is also shown.

$$E_d = E_o - \Delta E_s - \Delta E_W - \Delta E_n, \tag{5.1}$$

where E_d is the energy deposited, E_o is the actual energy, ΔE_s is the source thickness, ΔE_w is the energy loss in the window and ΔE_n is the energy difference from the non-linear response. The actual energy in this case was from ^{241}Am: 5485.56(12) keV. The effective thickness of the source was approximated to be ~1 keV. The DSSD used was a 150 μm BB20 with a 0.1 μm window. The stopping power of alphas given by SRIM [30] is approximately 1.34×10^2 keV/μm therefore the energy deposited on the window was ~13.4 keV. The energy from the non-linear response was ~13.8 keV as described by Lennard [87]. Inserting these values into equation 5.1 gives $E_o - E_d = 28.2$ keV.

In the case of protons, the activity is instead implanted so there is a contribution from the recoil and a small contribution from the non-linearity of 2.6 keV. A factor of 0.28 is also accounted for in the recoil pulse height defect which is under study by Page *et al.* [88]. After considering these factors, the corrected, 'real' proton energies become $E_{p1*} = 923.7$ keV and $E_{p2*} = 799.3$ keV.

The difference in the energy values is relatively small showing that the non-linearity effect and the contribution from the recoil added to the 28% pulse height defect cancels each other out. After accounting for the energy difference between the actual energy and the energy deposited, the final values become $E_{p1Final}$= 951.9 keV and $E_{p2Final}$= 827.5 keV, as presented in figure 5.6.

The difference between the final proton Q values is shown by ΔQ_p=(951.9-827.5)(1+1/130) keV = 125.4 keV. The gamma-ray energy was measured to be 125.4 keV. The γ energy and ΔQ_p are therefore in perfect agreement.

It is interesting to note that the difference in proton Q values based on the original uncorrected peak energies is very similar ΔQ_p=(923.1-798.5)(1+1/130) keV = 125.6 keV.

In the current work, no such calibration source was used as the aims of the experiment did not require such a detailed measurement. The main focus was the prompt in-beam measurement. The data obtained in JM06 does however allow an observation of the silicon response in the DSSD. The fine structure has been previously observed, but as the first measurement of the 2^+ to 0^+ transition in the ^{130}Sm daughter, it is possible to compare the direct measurement with the difference in the proton energies.

5.1.2 Proton Efficiency

To calculate the final production cross section it is important to know the proton collection efficiency. Implementing SRIM [30], the collection of software packages used to calculate multiple features of the interaction of ions in matter, it is possible to establish the range and stopping power of ions within a detector. To calculate the efficiency of protons in our experiment, H can be used to represent an individual proton, and a silicon target used to simulate the DSSD at the focal plane.

The range of a 950 keV proton in silicon is 17 μm. The DSSD used was 150 μm thick. Selecting Eu as the ion, initially looking at a range of 100 MeV-200 MeV (estimated from previous calculation) incident upon the silicon target, SRIM is able to calculate the implantation depth of the ion within the silicon. In order to collect 100% of the

protons, the energy is selected at which point the implantation depth exceeds $\sim 20~\mu$m. At the ^{131}Eu recoil energy of 150 MeV the range in silicon is $\sim 18~\mu$m. The reference particle entering the MARA separator was calculated to have an energy of 186 MeV.

The MWPC is represented within SRIM as a mylar target. In reality this consists of two mylar windows which will alter energy of the reference particle as it interacts. The ^{131}Eu recoils enter MARA with E_{lab}=186 MeV where the stopping power in MYLAR is ~ 94 MeV/mg/cm^2. The total energy loss in the gas counter was calculated to be ~ 24 MeV. Therefore, even once this is accounted for, the protons are still unable to escape the silicon and 100% collection efficiency can be assumed.

5.1.3   Cross Section Estimates

In the JM06 experiment the same reaction was used as by Sonzogni *et al.* [16]. Beginning with a lab energy of 390 MeV and excitation energy of 79 MeV. Under these conditions 3350 protons were measured to have been emitted from ^{131}Eu to the ground state in ^{130}Sm over a period of 5 days with an average beam current of 3 pnA. This averages to 9 protons per hour per pnA.

The proton branching ratio for ^{131}Eu is 89% [70] and 20% of protons emitted from ^{131}Eu form the fine structure transition. The MARA transmission is 50(10) % as quoted in [29]. The proton collection efficiency is assumed to be 100%. Using equation 3.11, the cross section, σ, is estimated to be 140(30) nb.

At the second beam energy of 364 MeV, the yield was calculated to be approximately 2 protons/h/pnA which gives an estimated yield

$$\frac{2}{9} \times 140nb \approx 30(10)nb. \tag{5.2}$$

The cross section in this data is much larger than the values seen in previous studies. There is a slight difference in bombarding energies between this and previous experiments which is likely to have improved the production, but it is unlikely to have accounted for the entire difference. It is possible that the value used for transmission at the FMA was overestimated as the MARA transmission value quoted here was a

conservative estimate.

5.1.4   Branching Ratio

Another important consideration is the behaviour of the conversion electrons. The gamma transition has an energy of 125(1) keV in ^{130}Sm. Assuming this is in fact an E2 transition, the total conversion is 1.083 (0.643 K- conversion) [89]. The K-electron energy is ∼77 keV and the L-electron energy is ∼117 keV. Based on the calculations carried out by Kantele [90] an electron with energy 77 keV has an extrapolated range in silicon of 35 μm which correlates to a stopping power of 3.8 keV/(mg/cm^2). An electron with energy 117 keV has an extrapolated range in silicon of 71 μm which correlates to a stopping power of 2.9 keV/(mg/cm^2). Therefore in 20 μm, energy losses of 17.6 keV and 13.6 keV for the K electrons and for the rest, respectively, can be estimated. If the energy loss from the escaping conversion electrons (and Augers, X rays) sum up with the fine structure proton line at 799 keV the sum peak would be visible at 825-830 keV. This is visible in figure 5.7. By taking the number of counts in this peak we can see how many have been removed from the 799(6) keV proton peak and adjust accordingly.

The main proton line from ^{131}Eu was measured to contain 3365 proton events. The 125(1) keV peak was measured to contain 55 γ rays. The γ-ray efficiency is 12(2) %, obtained from gamma-gamma coincidences in the isomers from the same data set. The L, M, N electrons will sum up with the main proton peak; roughly half of the electrons will escape, therefore using equations 2.35 and 2.36, the number of counts is estimated to be 108. Subtracting this value from the main peak gives 3257 protons. The fine structure proton branch becomes

$$\frac{953}{953 + 3257} = 23(5)\% \tag{5.3}$$

This value is in good agreement with the value of 24(5)% given by Sonzogni *et al.* [16].
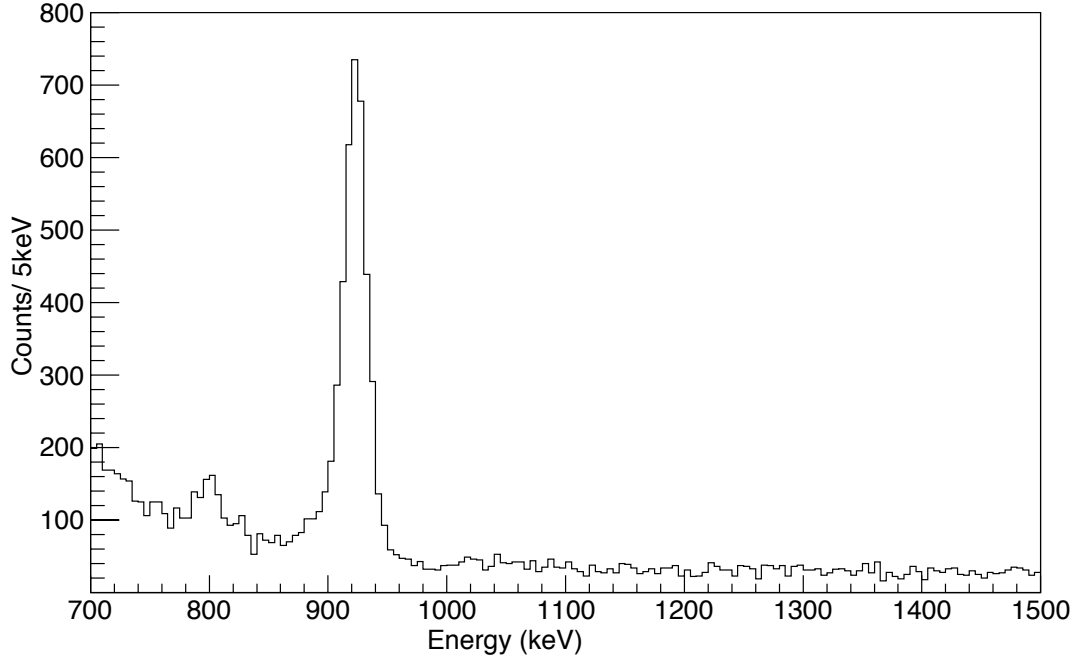
Figure 5.7: Decay energy as seen in fig. 5.4 shown with a smaller energy range to display electron summing from 825-830 keV.

5.1.5   Half Life

The half-life spectrum can be seen in figure 5.8. Schmidt *et al.* [91] described a method of fitting exponential distributions with at least two components. In this data there are two components which can be fitted separately, the background lifetime and the proton component. Using a two-second search time the separate components are clear to see. If the background was not fitted it would lead to an underestimation of the half life. The density distribution to be fitted is described by Schmidt *et al.* [91]

$$\left| \frac{dn}{d\Theta} \right| = n_0 exp(\Theta + ln\lambda)exp(-exp(\Theta + ln\lambda)). \tag{5.4}$$

The individual decay times are arranged within a spectrum using time intervals Δt. The data is presented in logarithmic time bins in order to allow decay time information over a large time scale and a reasonable number of channels. This function is an asymmetric, bell shaped curve shifted by $ln\lambda$ where the height is dependent on the number of counts. By representing the data as two asymmetric curves and removing

N1 = 331.58 +/- 18.0

$t_{1/2}$ 1 = 17.64 ms
$t_{1/2}$ 2 = 949.52 ms
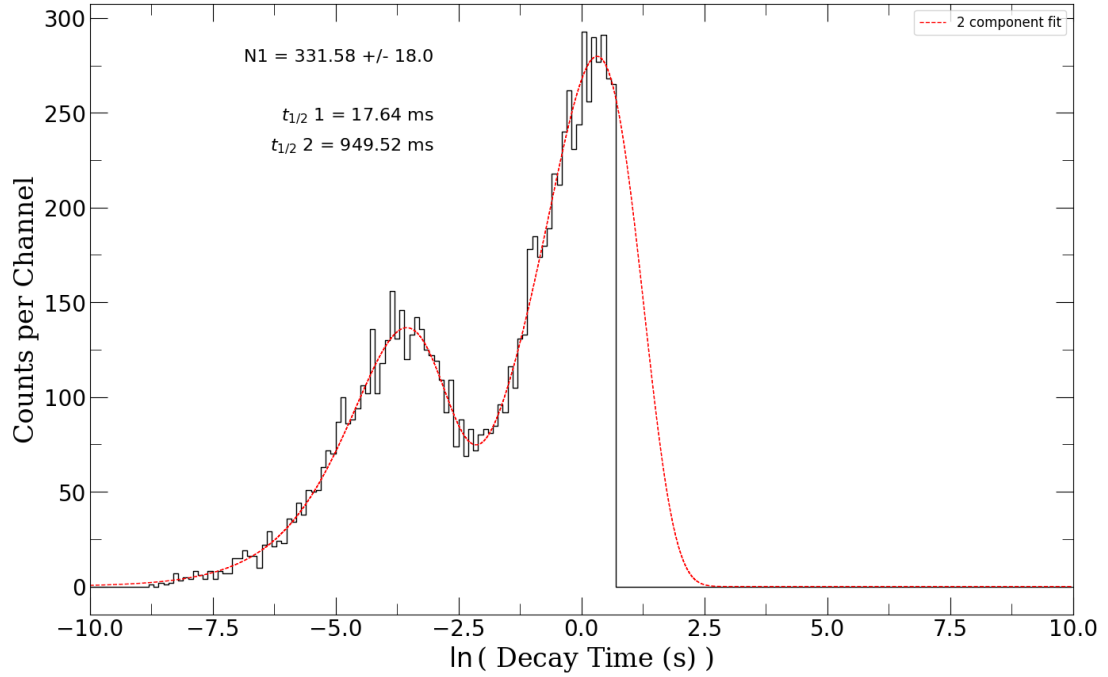
Figure 5.8: Two component half-life fitting of the main proton emission from ^{131}Eu. A two second searching time was used.

the background component, it is ensured that both λ and n_0 are correct for the desired decay and the half life can be extracted accurately. When adding a second component to the density function, it becomes

$$|\frac{dn}{d\Theta}| = (n_1\lambda_1 e^{-\lambda_1 e^\theta} + n_2\lambda_2 e^{-\lambda_2 e^\theta})e^\Theta, \tag{5.5}$$

where n_1 and n_2 are the number of counts in the two different components and λ_1 and λ_2 are the decay constants of each activity. A substitution of $\Theta=\ln t$ is used.

The function fitted in figure 5.8 gives a half-life of 17.6(5) ms for the main proton emitted from ^{131}Eu and 949.5 ms as the half-life of the background component. In reality there are multiple components to the background due to various decays however a two-component fit is sufficient in this case. This is in good agreement with the previously measured value for the half-life and the statistics in this case are greatly improved.

5.2   In-Beam Gamma-ray Spectroscopy

As described in chapter 4, previously no band assignments have been made for the excited states in ^{131}Eu as the statistics were too low when investigated by Seweryniak *et al.* [65]. The spectrum produced had no definite structure, it was too complicated to confidently identify any transitions although there were indications that rotational bands were present. In chapter 4 it was also discussed what we expected to see in terms of the band assignments. In the data taken for this thesis, the spectra of gamma rays in coincidence with the main proton and the fine structure proton had improved statistics compared to previous measurements. Although identification of rotational bands was still challenging, it was possible to identify gamma-gamma coincidences for the first time in ^{131}Eu.

During a p4n fusion evaporation reaction there is a source of background introduced from the evaporated neutrons. The (n,n$'\gamma$) reactions create bumps in the spectra from ^{72,74}Ge approximately at energies of 600 keV and 830 keV. When the neutrons scatter they can excite the Ge or be absorbed, producing a characteristic gamma ray. These gammas are not in the moving frame but have been Doppler corrected with the other gamma rays, therefore they are shown at an energy different to their real energy. This background has to be considered since the ^{131}Eu produced comes in the p4n evaporation channel.

The gamma-ray singles spectra obtained with JUROGAM 3 can be seen in figure 5.9. Panel (a) shows the gamma rays coincident with the main proton emission in ^{131}Eu seen at the focal plane that have been identified as rotational band(s). Panel (b) shows the prompt gamma rays coincident with the fine structure proton line at the focal plane. These coincidences were made using a 50 ms search time with any events detected in the punch-through detector vetoed, including a condition that the proton event must only occur within one pixel at the DSSD and the maximum difference in energy between the x and y strips must not exceed 60 keV. The gamma rays can be seen far more clearly in coincidence with the main proton which is to be expected as there are more events in the main line than the fine structure. As indicated by the arrows on panel

(b) there are still signs of the peaks which confirms the previous conclusions that the protons are emitted from the same state in ^{131}Eu. These spectra are both shown with the background subtracted however the subtraction when gating on the fine structure proton is not a full representation of the background that is present. This is due to the presence of electron summing, as explained when discussing the branching ratio, so the background component can only be subtracted to the right hand side of the main proton peak where the beta background is significantly less. It looks as if there is evidence of another band in figure 5.9, however we were unable to identify any further coincidences due to the limited number of statistics, so these peaks are listed in table 5.2.

5.2.1   Gamma-ray Coincidences

Figure 5.10 shows prompt gamma-gamma coincidences gated on the main proton emitted from ^{131}Eu as seen in JUROGAM 3. In panel (a) a gate was created on the 177 keV peak, the resulting coincidences can be seen. Note that there is an indication of a peak at 179 keV. As the peak at 177 keV cannot be coincident with itself, it is likely that this is a doublet. Panel (b) shows the coincident gamma rays when gated on 177 keV or 414 keV. This is an 'or' condition so the gamma rays may be coincident with either of the peaks. The 268 keV peak emerges when the 414 keV gate is added suggesting that it is not coincident with 177 keV but is 'seen' by the 414 keV peak. The other identified peaks visibly grow above the background with the additional gate other than 414 keV telling us that they are coincident. In panel (c) 535 keV is added to the gating conditions and the only additional peak that becomes visible is at 86 keV. The arrows displayed in panels (b) and (c) indicate the peaks identified in the panel(s) above, used to clearly demonstrate the coincidences with additional gating conditions. These spectra obviously have very low statistics however the coincidences are suggested by the various gate combinations tested. The 628 keV gamma ray can be seen in figure 5.9 when gating on the main proton and the fine structure proton. Due to the low statistics in the gamma-gamma coincidences the 628 keV gamma ray is not clearly visible but its
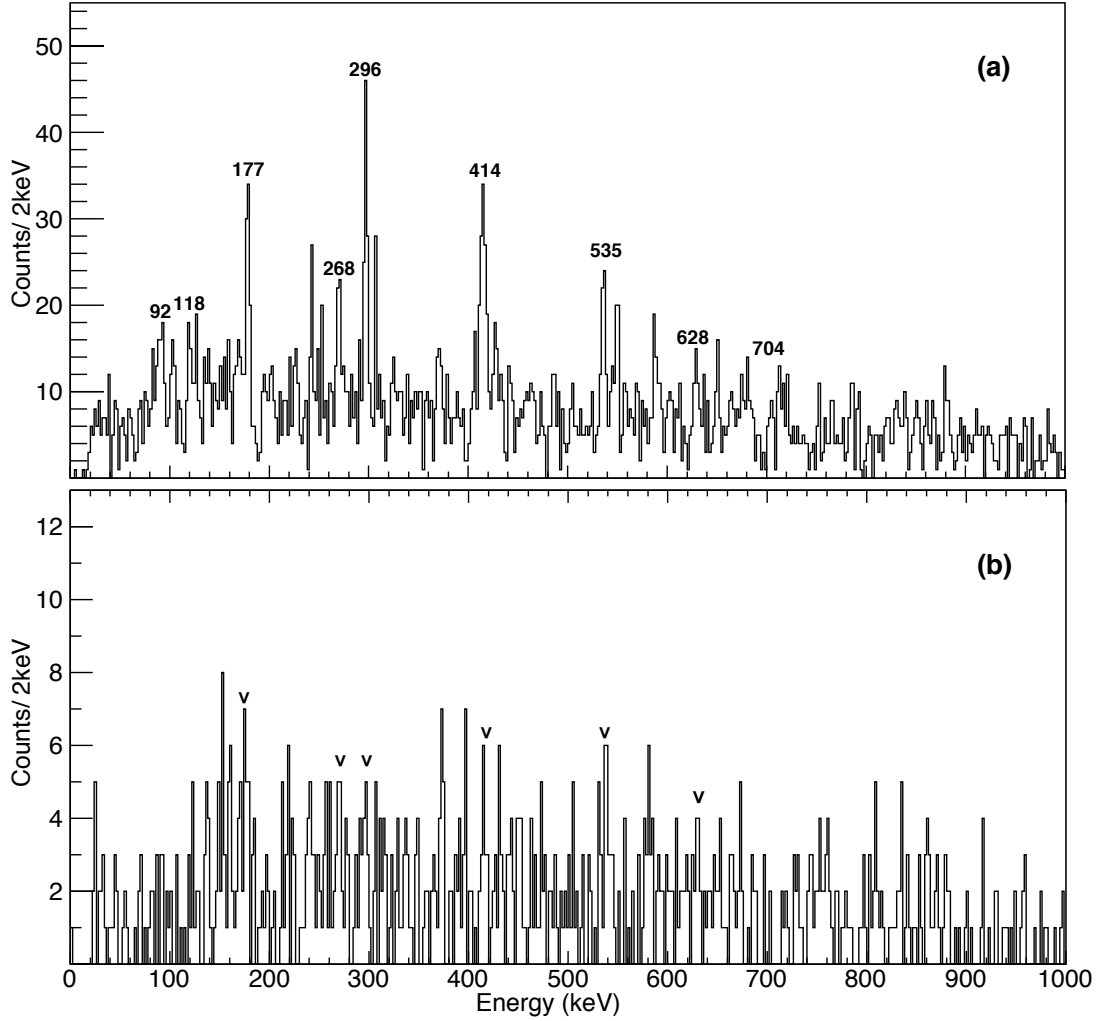
Figure 5.9: Prompt gamma-ray energy spectra obtained with the JUROGAM 3 spectrometer gated on (a) The main proton in ^{131}Eu and (b) The fine structure proton in ^{131}Eu.

existence cannot be ruled out. Based on these gamma-gamma coincidences two partial rotational bands were constructed as seen in figure 5.11. The intensities of the in-beam gamma rays can be calculated by assuming the 414 keV peak has an intensity of 100% as shown in table 5.2.

Using Grodzin's formula as can be seen in equation 5.6 and the transition in ^{130}Sm at 125(1) keV, the beta value is calculated to be 0.34(1).

$$E(2^+)[MeV] = \frac{1225}{A^{\frac{7}{3}}\beta_2^2} \tag{5.6}$$
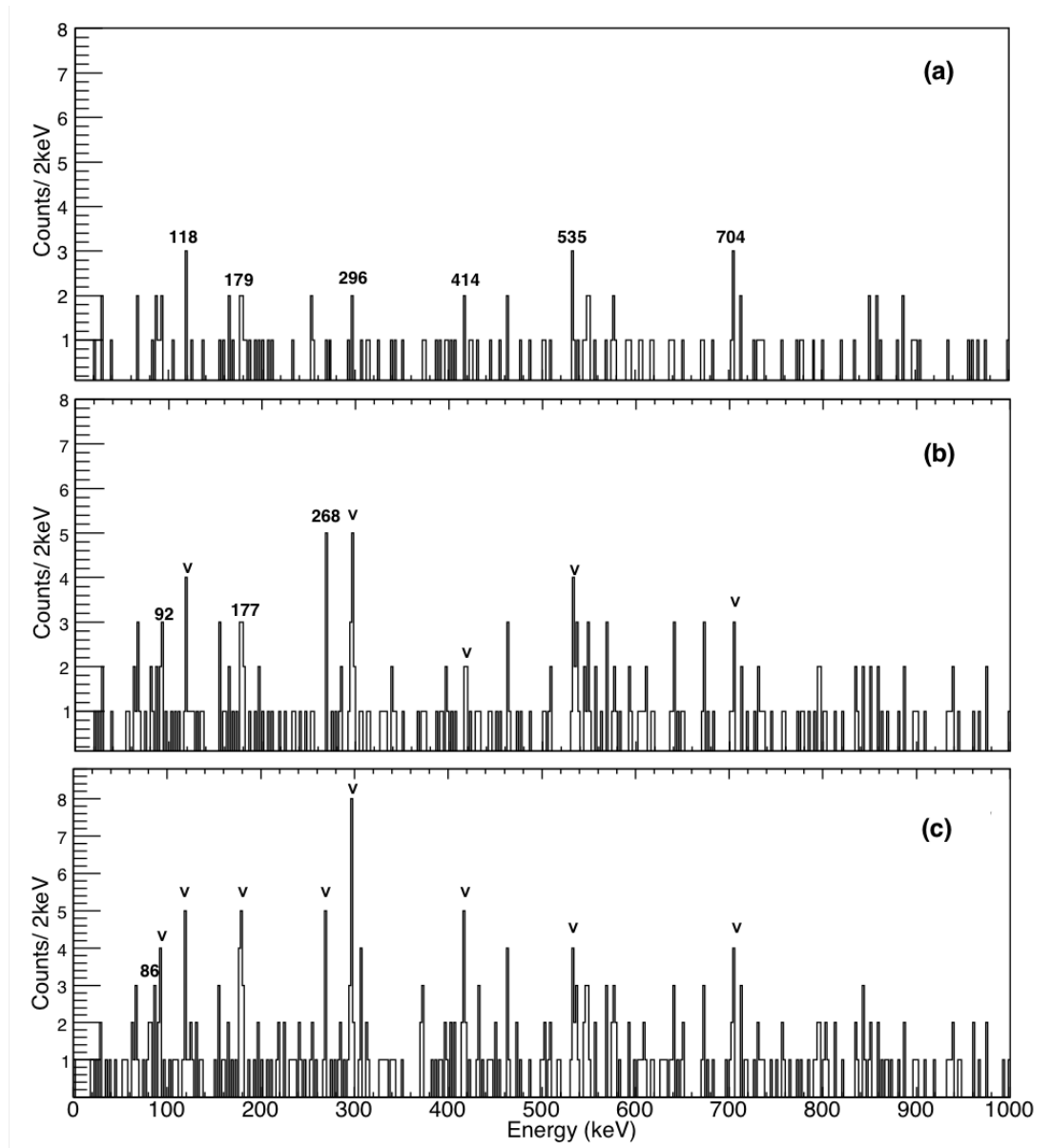
Figure 5.10: Prompt gamma rays in coincidence with (a) the 177 keV gamma ray (b) the 177 keV or 414 keV gamma rays (c) the 177 keV, 414 keV or 535 keV gamma rays.
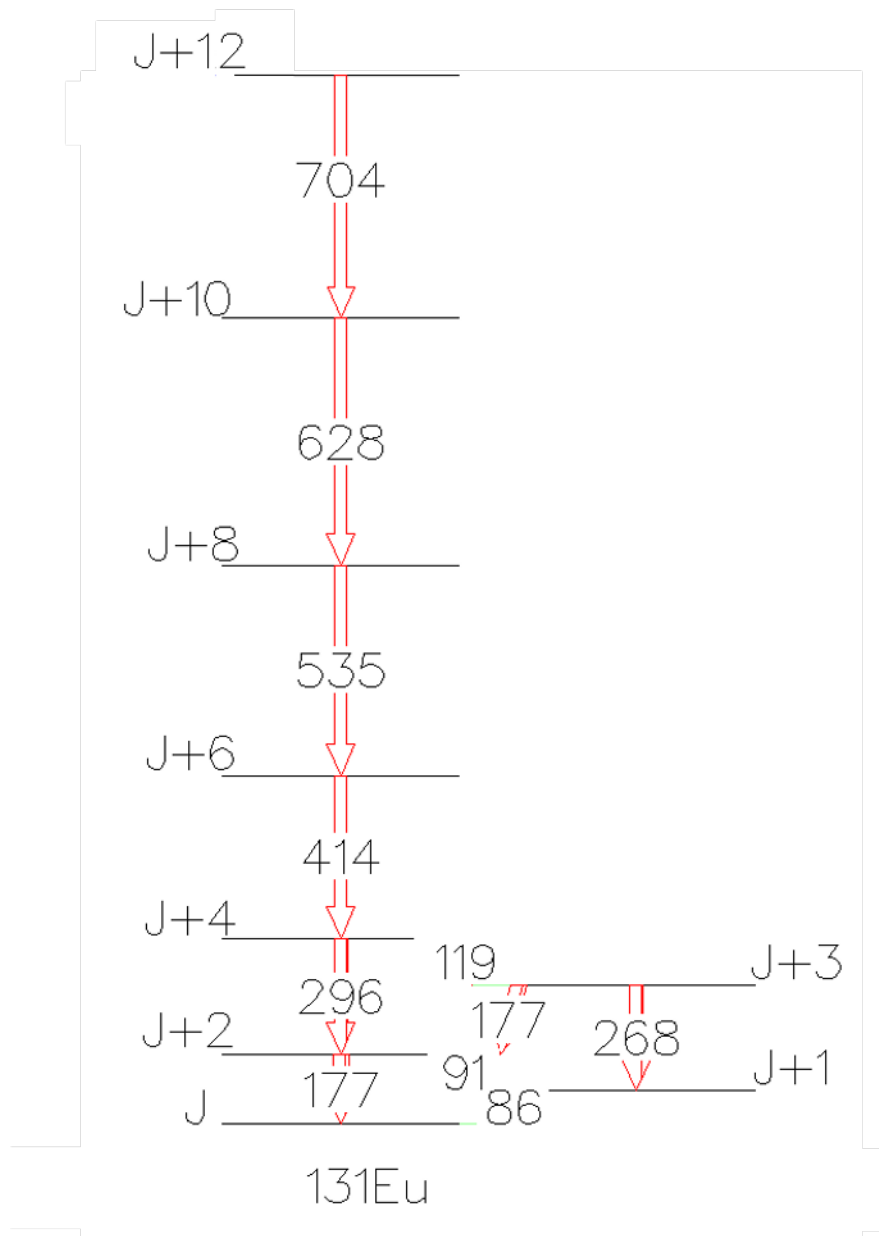
Figure 5.11: Excited states in ^{131}Eu identified through gamma-gamma coincidence measurements using JUROGAM 3.

E(level) (keV)	E(γ) (keV)	I(γ)
0		
177(1)	177(1)	63(7)
473(1)	296(1)	84(9)
887(2)	414(1)	100(10)
1421(2)	535(2)	54(6)
2049(2)	628(2)	30(6)
2753(2)	704(2)	
86(1)	86(1)	
354(1)	268(1)	39(4)
177(1)	91(1)	25(3)
354(1)	177(1)	
473(1)	118(1)	27(3)
	306(1)	
	372(1)	
	426(1)	
	550(2)	
	585(2)	
	647(2)	

Table 5.2: Intensities of the gamma-ray transitions relative to the 414(1) keV peak as seen in figure 5.11. It appears as if the peak at 177(1) keV is a doublet. Peaks are also listed that were present but due to the limited number of statistics, coincidence measurements could not be made to place them in the band structure.

Previous studies [16, 63] concluded that the protons are emitted from the $3/2^+$ state and the data produced in this thesis agree with those conclusions.

The moment of inertia for the rotational band in ^{130}Sm is calculated to be 24.0 $\hbar^2$MeV^{-1}. When building the level scheme for ^{131}Eu this value was used as a point of reference to ensure the moment of inertia for the new structure was of a reasonable value. Based upon the proposed level scheme for ^{131}Eu as seen in figure 5.11, the moment of inertia could be calculated for various band assignments to see if they appeared to be within a reasonable range of the value for ^{130}Sm. A meticulous process was carried out to compare band assignments for the structure to determine if the moment of inertia of the band was within range of the ^{130}Sm daughter, and to establish
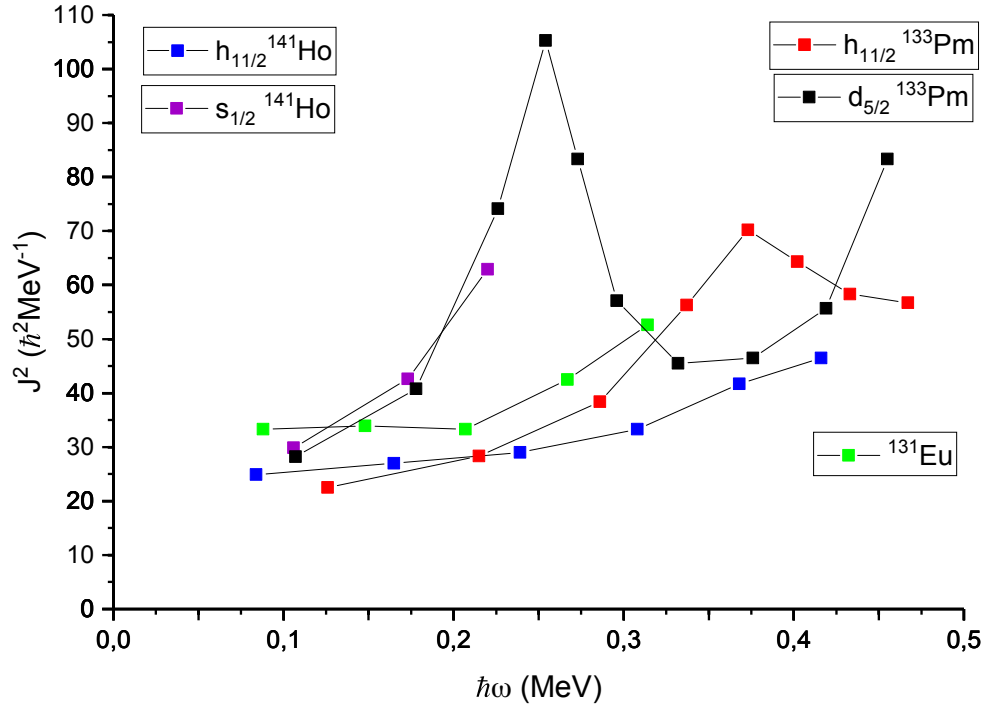
Figure 5.12: Dynamic moment of inertia as a function of frequency for bands in ^{141}Ho, ^{133}Pm and the newly identified band structure in ^{131}Eu for comparison.

if the predicted values versus experimental values for the gamma-ray energies were in agreement. The values for some similar cases in the region were calculated to see how well the energies agree assuming a constant moment of inertia. It is expected to see an effect of centrifugal stretching in rotating nuclei, effectively a stretching of the nucleus due to the centrifugal force. This results in an increase in the moment of inertia and a suppression of the energy levels. When this effect is present the experimental energies will be lower than the predicted energies as this has not been taken into account. This method provided values that appeared reasonable for all band assignments that were proposed, so although indicative that the excited states behave as nuclei in the region, gave no definitive answers as to which band assignments are more or less likely.

As the band assignments in ^{131}Eu cannot be concluded with confidence, there are some other structural situations that should be considered. The dynamic moment of inertia of the bands built upon the $h_{11/2}$ proton configuration in ^{141}Ho and ^{133}Pm, the $d_{5/2}$ configuration in ^{133}Pm and the $s_{1/2}$ configuration in ^{141}Ho have been presented for

comparison in figure 5.12. The dynamic moment of inertia has no spin dependence so the band identified in ^{131}Eu has been plotted without the need for spin assignments. The obtained gamma-ray emission pattern appears to support a $h_{11/2}$ assignment for the band. If this is the case, there is an isomer present for which the experiment was not sensitive and the bandhead is 'hanging'.

The kinematic moment of inertia is dependent on the spin assignment. Kinematic moment of inertia plots can be seen in figure 5.13 where in (a) the band in ^{131}Eu is assumed to have been built upon the $d_{5/2}$ proton configuration and ^{133}Pm is presented for comparison. In (b) the band is assumed to have been built upon the $h_{11/2}$ proton configuration and ^{141}Ho is presented for comparison. Figure 5.13 appears to also support a $h_{11/2}$ assignment for the band, however no clear conclusions can be made.

There are several possible transitions from the $h_{11/2}$ $[523]7/2^-$ to the ground state $d_{5/2}$ $[411]3/2^+$ band:

- At $\beta_2 \sim 0.35$ the $g_{9/2}$ state (Nilsson state $[404]9/2^+$) is close to the Fermi surface. This would allow a delayed E1 transition between the $h_{11/2}$ $[523]7/2^-$ and $g_{9/2}$ $[404]9/2^+$ bands, then further transitions from the $g_{9/2}$ band to the $g_{7/2}$ $[413]5/2^+$ band and then to the $d_{5/2}$ $[411]3/2^+$ band.

- An E1 transition is possible from the $h_{11/2}$ $[523]7/2^-$ band to the $g_{7/2}$ $[413]5/2^+$ band, then an M1 transition to the $d_{5/2}$ $[411]3/2^+$ band. This could be at a scale of ~ 10 ns.

- An M2 transition from the $h_{11/2}$ $[523]7/2^-$ band to the $d_{5/2}$ $[411]3/2^+$ band. This would be slower, of the scale of hundreds of μs.

There are multiple examples of similar transitions in the mass region near ^{131}Eu. In ^{135}Pr there is an M2 isomer from the $h_{11/2}$ bandhead with a 105 μs half life [92]. An M2 isomer is present in ^{131}La with a 170 μs half life from the $h_{11/2}$ bandhead [92]. In ^{133}La an E1 isomer with 62 ns half-life has been seen [93] from the $h_{11/2}$ bandhead. There is an M2 isomer in ^{137}Pr with a 2.66 μs half life from the $h_{11/2}$ bandhead [94], this kind of isomer would have been visible in our data.
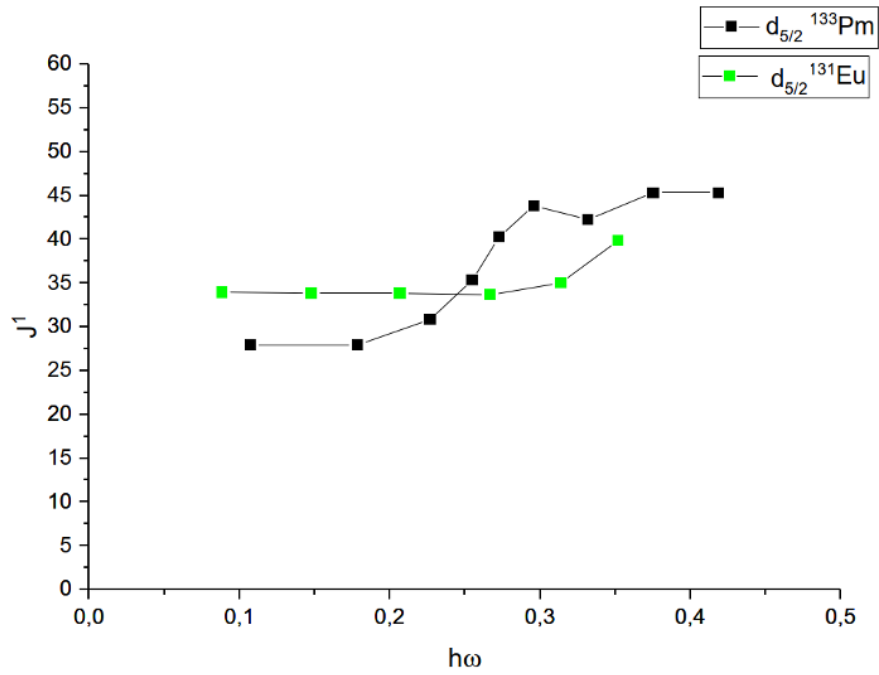
(a) A comparison of $d_{5/2}$ bands.
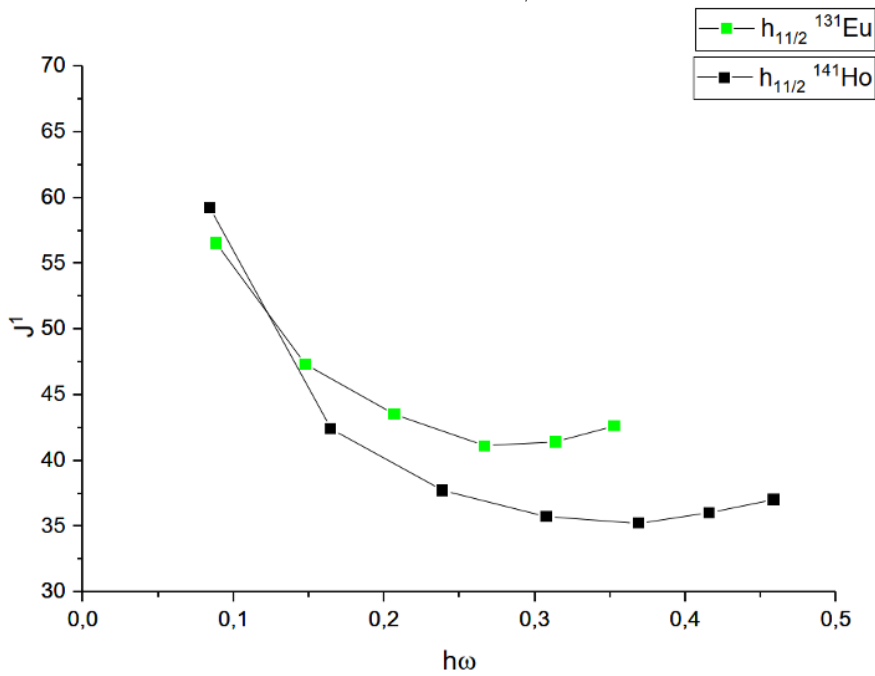
(b) A comparison of $h_{11/2}$ bands.

Figure 5.13: Kinematic moment of inertia plots to compare possible band assignments in ^{131}Eu.
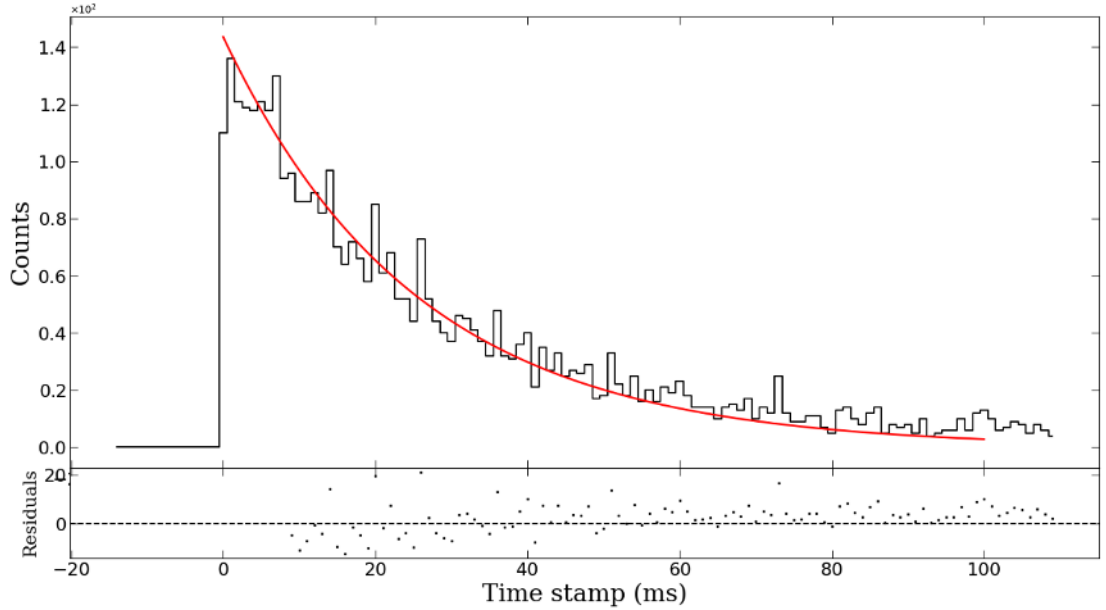
Figure 5.14: Half life of the main proton emitted in ^{131}Eu presented with 0.1 ms binning to search for a 'feeding' transition.

The isomers considered in this work can be divided into three categories: fast gamma-decaying isomers, slow gamma-decaying isomers and slow particle-decaying isomers via emission of a proton or beta particle.

A search for fast gamma-decaying isomers related to ^{131}Eu was carried out by looking at the life times of decays in the focal-plane germanium detectors. In total 3365 proton events were identified in this work. The recoil flight time through the MARA separator is ≈400 ns. Proton decay tagging is a very effective tool to look for isomers, however no evidence of a fast isomer in the time scale > 50 ns was identified. We cannot rule out of an existence of an isomer < 50 ns.

The line shape on the half-life spectrum as seen in figure 5.8 does not support the existence of an isomer feeding the ground state in the time scale of ≈10 ms. Similarly the spectra shown in figure 5.3 do not support a longer lived isomer feeding the ground state. The area of the main proton peak does not increase with the searching times longer than 100 ms. We cannot rule out a case where there is an isomer of the time scale ≈ 20 μs – 1 ms.

The half life was plotted again with 0.1 ms binning in figure 5.14 to search for a 'feeding' component to the transition. The curve is based on the 17.64 ms half-life fitting made in figure 5.8. At the beginning of the curve there appears to be a flat area lasting for a few ms. This could be indicative of a 'feeding' component based on an M2 transition, however it is difficult to say with confidence.

No evidence of additional proton peaks can be found in figures 5.3 and 5.4. This data was not sensitive to correlate with beta-activities. If there is a beta-decaying isomer the decaying state must have a relatively high spin. The proton-decaying ground state has been identified to have spin and parity $3/2^+$. If a long-living high-spin isomer originating from $h_{11/2}$ is present, it is expected that in heavy-ion induced fusion evaporation reactions that state would be populated more strongly than the low-spin state. The production cross section obtained for ^{131}Eu does not support this scenario as it follows the systematics of measured cross sections in p4n evaporation channels acquired for known proton emitters.

Looking at the cross-section calculation carried out and the expected systematics of the pxn channel, there is unlikely to be a beta-decaying high-spin state present. If it was there it would be highly populated relative to the low-spin ground-state and the measured cross section to produce ^{131}Eu in the p4n evaporation channel unexpectedly high.

In the search for in-beam data during the JM06 experiment, it was possible to carry out isomer tagging for other nuclei. By tagging on delayed gamma rays observed at the focal plane within a time window of implantation of the recoil, prompt gamma rays originating from the same nucleus can be identified. Some of these can be seen in figure 3.6.

Although the level structure and dynamic moment of inertia plot suggests that the identified band in ^{131}Eu could be based on the 7/2[523] Nilsson state, such as that seen in ^{141}Ho, identified by Seweryniak *et al.* [66], the low-energy state patterns identified for the neutron-rich Tb isotopes [95] may also indicate that the band obtained in this study is actually based on the $3/2^+$ state, specifically in the case of ^{161}Tb which is

	Experimental /keV	MOI Predicted /keV	^{132}Sm Predicted /keV
2^+	125	125	125
4^+		417	395
6^+		875	788
8^+		1500	1282
10^+		2292	1857

Table 5.3: Gamma-ray transition energies in ^{130}Sm, predicted using both constant moment of inertia and by ratios of energy levels in ^{132}Sm.

located as far from the neutron magic numbers as ^{131}Eu, so should occupy similar proton Nilsson states. A similar structure is seen in this nucleus to our rotational band(s) built upon the $3/2^+$ state.

5.3 ^{130}Sm

The information on the structure of ^{130}Sm is limited however using various methods it is possible to predict the rotational band above the single transition that we have been able to measure.

The rotational model, as described in chapter 2, allows us to obtain a moment of inertia for ^{130}Sm based upon the measured 2^+ to 0^+ transition. Substituting the transition energy into equation 2.15, a moment of inertia is obtained of 24.0 $\hbar^2$MeV^{-1}. Using this same equation it is possible to calculate the theoretical energies of each level. This information can then be used to help develop the structure of ^{131}Eu which can be modelled as a ^{130}Sm core with an additional single proton.

Grodzins [96] discovered that gamma-ray transition probabilities of even-even nuclei from the first 2^+ states show uniform behaviour within the $12 \leq A \leq 240$ range. It was found that the transition probabilities are approximately proportional to E^4 where E is defined as the transition energy. In a perfect rotor, the ratio of the energies of E(4^+)/E(2^+)=3.333, E(6^+)/E(2^+)=7, E(8^+)/E(2^+)=12 etc. By comparison it is possible to calculate the yrast band in ^{130}Sm from the known yrast band in ^{132}Sm [50].

Using the ratios as in Grodzins' rule, the predicted yrast band in ^{130}Sm is shown in the table 5.3.

By tagging on the 125(1) keV transition at the focal plane as seen in figure 5.6, a search was conducted for further transitions in ^{130}Sm, however nothing else could be confidently identified at either the focal-plane detection system or the in-beam detection system. The predicted values presented in table 5.3 are in reasonable agreement at low energies however no transitions could be identified at the transitions predicted. Further study is needed to establish rotational bands in ^{130}Sm.

Chapter 6

Conclusions

6.1   Summary

Proton radioactivity from ^{131}Eu has been remeasured with a proton energy of 952(5) keV for the ground state transition to the ground state in the ^{130}Sm daughter and a proton energy of 828(6) keV for the fine structure transition from the ground state in ^{131}Eu to the 2^+ excited state in the ^{130}Sm daughter. The 2^+ to 0^+ transition in ^{130}Sm was also measured directly for the first time with an energy of 125(1) keV. A branching ratio of 0.23(5) was obtained from this study, in close agreement with previous studies. A deformation of $\beta \approx 0.34(1)$ was also obtained. A half life measurement for the main proton emission yielded a value of 17.64(5) ms through a two-component half life fitting with the background.

In-beam data from this study was highly fruitful and through gamma-ray correlations it was possible to build rotational band(s). The obtained level structure and the dynamical moment of inertia plot when compared to ^{141}Ho suggest that the band is based on the 7/2[523] Nilsson state. However, the ground state has been identified to be based on the 3/2[411] Nilsson orbital. No clear evidence for existence of any sort of isomeric decay feeding the ground state could be identified. The low energy-state patterns identified for neutron-rich Tb isotopes from may also indicate that the band obtained in this study is actually based on the $3/2^+$ state. As a result, the band identified in

this study cannot firmly be assigned and further study is needed.

6.2   Improvements

JM06 was the first experiment with the newly commissioned JUROGAM 3. It was a highly successful experiment which exceeded the expectations laid out in the proposal and produced a large amount of data, far more than that laid out in this thesis.

JYTube, the charged particle veto detector, was not available for use in the JM06 experiment. This was due to issues maintaining the necessary vacuum following the installation of a new target chamber. When JYTube was in use there was significant outgassing from the detector which lead to sparking in the electrostatic deflector. As a result the experiment was run at a charge state higher than optimal to reduce the sparking. Even with this mitigation there was frequent sparking and a significant amount of beam time was lost to conditioning the deflector. The presence of JYTube in the experimental setup would have allowed for an additional veto at the target position which would have reduced background for both in-beam and focal-plane spectra. The full focal-plane gamma-ray detection system was not available for the entirety of the experiment. The addition of more germanium clover detectors would add to the statistics measured at the focal plane. In future experiments BEGe detectors would be a valuable addition to the focal plane to improve upon the resolution of lower energy gamma rays and X rays.

During the M09 experiment, a search was conducted for β-delayed proton emitters ^{133}Gd and ^{132}Eu. Strong enough evidence was not seen during online searches for these nuclei to continue the search and unfortunately no further evidence was found during the offline analysis. In the proposal, yield estimates were given based upon production cross sections and β-delayed proton branches inferred from the closest available neighbours: $\sigma_{\beta p} = 40$ nb for ^{133}Gd and $\sigma_{\beta p} = 100$ nb for ^{132}Eu. It is likely that the reason these nuclei were not observed is that the total implant recoil rates at the focal plane during this experiment were too high. For many nuclei in this region the production cross sections are too small compared to the yields of corresponding isobars so even with

the mass separating capabilities of MARA, observation is extremely difficult. The information gained in this study will inevitably aid in the future search for β-delayed proton emission in these nuclei.

6.3   Future case studies

Of course, an obvious case for a future experiment would be further study into the structure of ^{131}Eu. With the benefit of the information gained in this study, the beam energy could be optimised alongside a full detection system, including JYTube and a full array of focal plane detectors, with more beam time to further add to the rotational bands observed so far and increase the $\gamma - \gamma$ coincidence statistics.

^{135}Tb is similar case to ^{131}Eu in that it is predicted to have a highly deformed, prolate shape with $\beta_2 \sim 0.33$ [4], as described in more detail in chapter 4. Fine structure from the proton emission in ^{135}Tb to the ^{134}Gd daughter is very likely [62]. Measurement of the fine structure branch and of the 2^+ to 0^+ transition in ^{134}Gd would help to further improve upon theories on proton decay from deformed nuclei.

A potential case for in-beam studies would be ^{131}Sm, by studying the beta-delayed proton emission. By tagging on the 159 keV gamma ray emitted from ^{130}Nd at the focal plane the prompt spectrum could be obtained. In the JM06 experiment a factor of 1.3 gamma-rays with an energy of 159 keV were observed in coincidence with protons when compared to the yield of ^{131}Eu protons. Once in-beam gamma rays have been identified, the gamma-ray condition can be relaxed and the beta-delayed protons can be tagged to obtain gamma-gamma statistics. If 10 % efficiency to see the 159 keV gamma-ray is assumed, and 50 % proton feeding to the 2^+ state in ^{130}Nd, a cross-section value of $\sigma_{\beta p} \sim 3.6~\mu$b can be estimated for ^{131}Sm.

As described in Chapter 4, the proton line in the decay from odd-odd ^{140}Ho has an energy that is lower than the energy of the decay from its odd-even neighbour ^{141}Ho [64]. A similar trend was noticed for transitional nuclei which have a deformation between spherical and strongly deformed, above Z = 50 [97]. In spherical proton emitters the energy dependence is the opposite. Considering the ^{140}Ho proton was observed with an

energy ≈ 100 keV lower than the proton in ^{141}Ho, this could explain why for example the proton emission from ^{136}Tb and ^{137}Tb have not yet been observed. Mass estimates [98] predict ^{136}Tb to be more proton unstable however looking at the study in [64], the reverse might be the case. This could be a good case for further focal plane studies using MARA.

The MARA Low-Energy Branch (MARA-LEB) [99–101] is under development for MARA. It will allow further study of proton-rich nuclei using laser ionisation spectroscopy and mass measurements. Ions will be produced through fusion-evaporation reactions and following mass separation in MARA they will be stopped and then extracted from a buffer gas cell at the focal plane. The ions will then be accelerated and transported to experimental setups using an ion transport system which consists of multiple focusing, accelerating and mass separating components. MARA-LEB will open the possibility to look for even weaker proton branches. For example ^{136}Tb could be an ideal candidate for study using isobaric transportation.

References

[1] J. Sarén *et al.* The new vacuum-mode recoil separator MARA at JYFL. *Nuclear Instruments and Methods in Physics Research Section B: Beam Interactions with Materials and Atoms*, 266(19):4196–4200, 2008.

[2] J. Uusitalo, J. Sarén, J. Partanen, and J. Hilton. Mass Analyzing Recoil Apparatus, MARA. *Acta Phys. Polon. B*, 50(3):319, 2019.

[3] J. Pakarinen *et al.* The JUROGAM 3 spectrometer. *The European Physical Journal A*, 56(149), 2020.

[4] P. Möller, J. R. Nix, W. D. Myers and W. J. Swiatecki. Nuclear Ground-State Masses and Deformations. *Atomic Data and Nuclear Data Tables*, 59(2):185–381, 1995.

[5] B. Blank. *One- and Two-Proton Radioactivity*, pages 153–201. The Euroschool Lectures on Physics with Exotic Beams, Vol. III. Springer, 2009.

[6] D. Kot, G. Kissinger, M. Schubert, and A. Sattler. Current Stage of the Investigation of the Composition of Oxygen Precipitates in Czochralski Silicon Wafers. *ECS Journal of Solid State Science and Technology*, 6:N17–N24, 2017.

[7] B. Blank and M. Płoszajczak. Two-proton radioactivity. *Reports on Progress in Physics*, 71(4):046301.

[8] W. Nazarewicz, M. A. Riley and J. D. Garrett. Equilibrium deformations and excitation energies of single-quasiproton band heads of rare-earth nuclei. *Nuclear Physics A*, 512(1):61–96, 1990.

[9] V. I. Goldansky. On neutron-deficient isotopes of light nuclei and the phenomena of proton and two-proton radioactivity. *Nuclear Physics*, 19:482–495, 1960.

[10] K. P. Jackson *et al.* $^{53}Co^{m}$: A proton-unstable isomer. *Physics Letters B*, 33:281–283, 1970.

[11] S. Hofmann *et al.* Proton radioactivity of ^{151}Lu. *Zeitschrift für Physik A Atoms and Nuclei*, 305(2):111–123, 1982.

[12] O. Klepper *et al.* Direct and beta-delayed proton decay of very neutron-deficient rare-earth isotopes produced in the reaction ^{58}Ni+^{92}Mo. *Zeitschrift für Physik A Atoms and Nuclei*, 305:125–130, 1982.

[13] M. Pfützner *et al.* Radioactive decays at limits of nuclear stability. *Rev. Mod. Phys.*, 84:567, 2012.

[14] D. S. Delion, R. J. Liotta, and R. Wyss. Theories of proton emission. *Physics Reports*, 424(3):113–174, 2006.

[15] A. de Shalit and I. Talmi, editors. *Centrifugal and Coulomb Barriers*, volume 14 of *Pure and Applied Physics*. Elsevier, 1963.

[16] A. Sonzogni *et al.* Fine Structure in the Decay of the Highly Deformed Proton Emitter ^{131}Eu. *Phys. Rev. Lett.*, 83:1116–1118, Aug 1999.

[17] L. Gerward and A. Rassat. Paul Villard's discovery of gamma rays – A centenary. *Comptes Rendus de l'Académie des Sciences - Series IV - Physics*, 1(7):965–973, 2000.

[18] T. J. Thaddeus. Rutherford on the alpha-beta-gamma classification of radioactive rays. *Isis*, 67(1):61–75, 1976.

[19] V. F. Weisskopf. Radiative Transition Probabilities in Nuclei. *Phys. Rev.*, 83:1073–1073, 1951.

[20] A. Gavron. Statistical model calculations in heavy ion reactions. *Phys. Rev. C*, 21:230–236, 1980.

[21] W. Reisdorf. Analysis of fissionability data at high excitation energies Pt 1. *Zeitschrift für Physik A Atoms and Nuclei*, 300:227—-238, 1981.

[22] E. Liukkonen, T. Antaya, J. Bishop and S. Motzny. Design of the Central Regions for the MSU 500 MeV Superconducting Cyclotron. In *Proc. 8th Int. Cyclotron Conf. and Their Applications, Bloomington, IN, USA*, pages 2107–2110, 1978.

[23] T. Kalvas *et al.* Central Region Upgrade for the Jyväskylä K130 Cyclotron. In *Proc. Cyclotrons'19*, International Conference on Cyclotrons and their Applications, pages 326–329, 2020.

[24] L. Sottili. Test of JYUTube as a veto detector at MARA for background suppression in nuclear spectroscopy beyond the proton drip line. Master's thesis, 2018.

[25] J. Sarén, J. Uusitalo, M. Leino, and J. Sorri. Absolute transmission and separation properties of the gas-filled recoil separator RITU. *Nuclear Instruments and Methods in Physics Research Section A: Accelerators, Spectrometers, Detectors and Associated Equipment*, 654(1):508–521, 2011.

[26] I. Lazarus *et al.* The GREAT triggerless total data readout method. *IEEE Transactions on Nuclear Science*, 48(3):567–569, 2001.

[27] I. Y. Lee. The GAMMASPHERE. *Nuclear Physics A*, 520:641–655, 1990.

[28] C. N. Davids *et al.* Startup of the Fragment Mass Analyzer at ATLAS. *Nuclear Instruments and Methods in Physics Research Section B: Beam Interactions with Materials and Atoms*, 70(1):358–365, 1992.

[29] J. Sarén. *The ion-optical design of the MARA recoil separator and absolute transmission measurements of the RITU gas-filled recoil separator.* PhD thesis, Department of Physics, University of Jyväskylä, 2011.

[30] J. F. Ziegler, M. D. Ziegler, and J. P. Biersack. SRIM – The stopping and range of ions in matter (2010), journal = Nuclear Instruments and Methods in Physics

Research Section B: Beam Interactions with Materials and Atoms. 268(11):1818–1823, 2010.

[31] P. Rahkila. Grain—A Java data analysis system for Total Data Readout. *Nuclear Instruments and Methods in Physics Research Section A: Accelerators, Spectrometers, Detectors and Associated Equipment*, 595(3):637–642, 2008.

[32] R. Simon *et al.* Evidence for nuclear shape coexistence in ^{180}Hg. *Zeitschrift für Physik A Hadrons and Nuclei*, 325:197–202, 1986.

[33] E. S. Paul *et al.* In-beam γ-ray spectroscopy above ^{100}Sn using the new technique of recoil decay tagging. *Phys. Rev. C*, 51:78–87, 1995.

[34] P. J. Sellin *et al.* A double-sided silicon strip detector system for proton radioactivity studies. *Nuclear Instruments and Methods in Physics Research Section A: Accelerators, Spectrometers, Detectors and Associated Equipment*, 311(1-2):217–223, 1992.

[35] D. M. Cullen *et al.* Identification of the $K^{\pi} = 8^{-}$ rotational band in ^{138}Gd. *Phys. Rev. C*, 58:846–850, Aug 1998.

[36] D. M. Cullen *et al.* Recoil-isomer tagging near the mass 140 proton drip line. *Nuclear Physics A*, 682(1):264–269, 2001.

[37] P. J. Woods and C. N. Davids. Nuclei beyond the proton drip-line. *Annual Review of Nuclear and Particle Science*, 47(1):541–590, 1997.

[38] B. Blank and M. J. G. Borge. Nuclear structure at the proton drip line: Advances with nuclear decay studies. *Progress in Particle and Nuclear Physics*, 60:403–483, 2008.

[39] A. N. Wilson *et al.* Observation of excited states in the near-drip-line nucleus ^{125}Pr. *Phys. Rev. C*, 66:021305, 2002.

[40] C. M. Parry *et al.* Yrast structures in the neutron-deficient $^{127}_{59}$Pr$_{68}$ and $^{131}_{61}$Pm$_{70}$ nuclei. *Phys. Rev. C*, 57:2215–2221, 1998.

[41] B. H. Smith *et al.* Enhanced deformation in light Pr nuclei. *Physics Letters B*, 443(1):89–96, 1998.

[42] A. N. James, Y. He, I. Jenkins and M. A. Skelton. The Decay of Rotational Band Heads Near Z = 60 N = 70. Technical Report Daresbury 1989-1990 Annual, 1990.

[43] P. K. Weng *et al.* High spin structure in odd-proton nuclei ^{129,131}Pr. *Phys. Rev. C*, 47:1428–1435, 1993.

[44] A. Galindo-Uribarri *et al.* Strongly coupled enhanced-deformation band in ^{131}Pr. *Phys. Rev. C*, 50:R2655–R2659, 1994.

[45] P. H. Regan *et al.* Spectroscopy of the light rare-Earth nuclei ^{133}Pm and ^{133}Sm: Configuration-dependent pairing and evidence for strong residual proton-neutron interactions in neighbouring odd-N and odd-Z nuclei. *Nuclear Physics A*, 533(3):476–504, 1991.

[46] A. Galindo-Uribarri *et al.* Lifetime measurements of strongly deformed rotational bands in ^{133}Pm. *Phys. Rev. C*, 54:1057–1069, 1996.

[47] J. N. Wilson *et al.* Properties of superdeformed band population in the A$\approx$130 region. *Phys. Rev. C*, 57:R2090–R2094, 1998.

[48] S.-W. Xu *et al.* New β-delayed proton precursors in the rare-earth region near the proton drip line. *Phys. Rev. C*, 60:061302, 1999.

[49] J. M. Nitschke *et al.* Beta-delayed proton decay in the lanthanide region. In *Nuclei Far From Stability: 5th International Conference*, volume 164 of *American Institute of Physics Conference Series*, pages 697–707, 1987.

[50] R. Wadsworth *et al.* Yrast Band Spectroscopy of ^{132}Sm and ^{130}Nd. *Z.Phys.*, A333:411, 1989.

[51] R. Wadsworth *et al.* Evidence for an i$_{13/2}$ Neutron Band in ^{133}Sm. *Z.Phys.*, A333:409, 1989.

[52] C. N. Davids *et al.* Proton decay of the highly deformed odd-odd nucleus ^{130}Eu. *Phys. Rev. C*, 69:011302, 2004.

[53] K. S. Vierinen *et al.* Decay of neutron deficient Eu, Sm and Pm isotopes near the proton drip line. *Nuclear Physics A*, 499(1):1–28, 1989.

[54] P. J. Bishop *et al.* A Study of Nuclei in the Mass 137 Region of the Light Rare Earths. *Fizika(Zagreb)*, 19, 1987.

[55] L. Goettig *et al.* Decoupled bands in odd-A rare-earth nuclei below N = 82. *Nuclear Physics A*, 475(3):569–578, 1987.

[56] C. J. Lister *et al.* Deformation of very light rare-earth nuclei. *Phys. Rev. Lett.*, 55:810–813, 1985.

[57] P. J. Bishop *et al.* Low-lying states in ^{138,140}Gd and ^{139}Eu. *Journal of Physics G: Nuclear Physics*, 14(7):995–1004, 1988.

[58] E. S. Paul *et al.* High-spin studies of neutron-deficient A=138 nuclei: ^{138}Eu and ^{138}Gd. *Journal of Physics G: Nuclear and Particle Physics*, 20(5):751–764, 1994.

[59] A. M. Bruce *et al.* Systematics of $K^{\pi} = 8^-$ isomers in N=74 nuclei. *Phys. Rev. C*, 55:620–624, 1997.

[60] M. G. Procter *et al.* Lifetime measurements in the transitional nucleus ^{138}Gd. *Phys. Rev. C*, 84:024314, 2011.

[61] M. G. Procter *et al.* High-K four-quasiparticle states in ^{138}Gd. *Phys. Rev. C*, 83:034311, 2011.

[62] P. J. Woods *et al.* Proton decay of the highly deformed nucleus ^{135}Tb. *Phys. Rev. C*, 69:051302, 2004.

[63] C. N. Davids *et al.* Proton Radioactivity from Highly Deformed Nuclei. *Physical Review Letters*, 80(9), 1998.

[64] K. Rykaczewski *et al.* Proton emitters ^{140}Ho and ^{141}Ho: Probing the structure of unbound Nilsson orbitals. *Phys. Rev. C*, 60:011301, 1999.

[65] D. Seweryniak *et al.* In-beam studies of proton emitters using the Recoil-Decay Tagging method. *Invited paper given at the International Symposium on Proton-Emitting Nuclei*, 2000.

[66] D. Seweryniak *et al.* Rotational Bands in the Proton Emitter ^{141}Ho. *Phys. Rev. Lett.*, 86:1458–1461, 2001.

[67] W. Królas *et al.* First observation of the drip line nucleus ^{140}Dy: Identification of a 7μs K isomer populating the ground state band. *Phys. Rev. C*, 65:031303, 2002.

[68] J. C. Batchelder *et al.* Recent Results Of Proton Drip-Line Studies At The HRIBF Recoil Mass Spectrometer. In *Frontiers of Nuclear Structure*, volume 656 of *AIP Conference Proceedings*, pages 77–82, 2003.

[69] M. Karny *et al.* Shell structure beyond the proton drip line studied via proton emission from deformed ^{141}Ho. *Physics Letters B*, 664(1):52–56, 2008.

[70] P. Möller, J. R. Nix and K. L. Kratz. Nuclear properties for astrophysical and radioactive-ion-beam application. *Atomic Data and Nuclear Data Tables*, 66(2):131–343, 1997.

[71] D. Seweryniak *et al.* GAMMASPHERE + FMA: A journey beyond the proton drip-line. *Nucl.Phys.*, A682:247c, 2001.

[72] F. D. Becchetti and G. W. Greenlees. Nucleon-Nucleus Optical-Model Parameters, A > 40, E < 50 MeV. *Phys. Rev.*, 182:1190–1209, 1969.

[73] A. T. Kruppa, B. Barmore, W. Nazarewicz, and T. Vertse. Fine Structure in the Decay of Deformed Proton Emitters: Nonadiabatic Approach. *Physical Review Letters*, 84(20):4549–4552, 2000.

[74] E. Maglione, L. Ferreira and R. J. Liotta. Proton emission from deformed nuclei. *Phys. Rev. C*, 59:R589–R592, 1999.

[75] E. Maglione and L. Ferreira. Fine structure in proton emission from deformed ^{131}Eu. *Phys. Rev. C*, 61:047307, 2000.

[76] L. Ferreira, E. Maglione and P. Ring. Covariant density functional theory for decay of deformed proton emitters: A self-consistent approach. *Physics Letters B*, 753:237–241, 2016.

[77] L. Ferreira, E. Maglione and D. E. P. Fernandes. Dependence of the decay widths for proton emission on the single particle potential. *Phys. Rev. C*, 65:024323, 2002.

[78] L. Ferreira and E. Maglione. Structure of proton-radioactive nuclei. *Journal of Physics G: Nuclear and Particle Physics*, 31(10):S1569–S1572, 2005.

[79] H. Esbensen and C. N. Davids. Coupled-channels treatment of deformed proton emitters. *Phys. Rev. C*, 63:014315, 2000.

[80] R. D. Page and D. T. Joss. Proton Emission- Recent Results and Future Prospects. *Nuclear Physics Review*, 33(2):180–183, 2016.

[81] W. J. Huang *et al.* The AME2016 atomic mass evaluation (I). Evaluation of input data; and adjustment procedures. *Chinese Physics C*, 41(3):030002, 2017.

[82] C. N. Davids *et al.* New proton radioactivities ^{165,166,167}Ir and ^{171}Au. *Phys. Rev. C*, 55:2255–2266, 1997.

[83] C. Rauth *et al.* First Penning Trap Mass Measurements beyond the Proton Drip Line. *Phys. Rev. Lett.*, 100:012501, 2008.

[84] S. Hofmann *et al.* Precision Alpha Energy Calibration Measurements in the Decay of Implanted Isotopes. *GSI Scientific Report*, GSI-81-2:204, 1980.

[85] S. Hofmann *et al.* Stopping of Alpha-Recoil Atoms in Silicon. *GSI Scientific Report*, GSI-82-1:241, 1981.

[86] W.N. Lennard *et al.* Nonlinear response of Si detectors for low-Z ions. *Nuclear Instruments and Methods in Physics Research Section A: Accelerators, Spectrometers, Detectors and Associated Equipment*, 248(2):454–460, 1986.

[87] W. N. Lennard, S. Y. Tong, G. R. Massoumi, and L. Wong. On the calibration of low-energy ion accelerators. *Nuclear Instruments and Methods in Physics Research Section B: Beam Interactions with Materials and Atoms*, 45(1):281–284, 1990.

[88] R. Page *et al.* To be published.

[89] T. Kibédi *et al.* Evaluation of theoretical conversion coefficients using BrIcc. *Nucl. Instr. and Meth. A*, 589:202–229, 2008.

[90] J. Kantele. *Handbook of nuclear spectrometry.* London: Academic Press, 1995.

[91] K. Schmidt. A new test for random events of an exponential distribution. *The European Physical Journal A*, 8, 2000.

[92] T. W. Conlon. New M2 isomers in neutron deficient I, La and Pr associated with a deformed nuclear shape. *Nuclear Physics A*, 213(3):445–460, 1973.

[93] M. Budzynsky *et al.* Measurement of Submicrosecond Lifetimes of Levels by a Single-Crystal Scintillation Time Spectrometer. *Yad.Fiz.*, 21:913, 1975.

[94] E. Dragulescu *et al.* High-Spin Spectroscopy of Pr Nuclei. *Rev.Roum.Phys.*, 32:485, 1987.

[95] J. S. Boyno and J. R. Huizenga. Levels of ^{155,157,159,161}Tb Excited in Helium - Induced Single-Proton-Transfer Reactions. *Phys. Rev. C*, 6:1411–1424, 1972.

[96] L. Grodzins. The uniform behaviour of electric quadrupole transition probabilities from first 2^+ states in even-even nuclei. *Physics Letters*, 2(2):88–91, 1962.

[97] R. D. Page *et al.* Decays of odd-odd N-Z=2 nuclei above ^{100}Sn: The observation of proton radioactivity from ^{112}Cs. *Phys. Rev. Lett.*, 72:1798–1801, 1994.

[98] P. E. Haustein. An overview of the 1986–1987 atomic mass predictions. *Atomic Data and Nuclear Data Tables*, 39(2):185–200, 1988.

[99] P. Papadakis *et al.* Development of a low-energy radioactive ion beam facility for the MARA separator. *Hyperfine Interactions*, 237(1), 2016.

[100] P. Papadakis *et al.* Status and development of the MARA low-energy branch. *AIP Conference Proceedings*, 2011(1):070013, 2018.

[101] P. Papadakis *et al.* The MARA-LEB ion transport system. *Nuclear Instruments and Methods in Physics Research Section B: Beam Interactions with Materials and Atoms*, 463:286–289, 2020.